

# Spontaneous complexity

This collection was first termed *Simple rules outsmart “intelligence”* and included originally documents 1 to 3 in which researchers at Ludwig-Maximilians-Universität in Munich describe a new model showing how biological or technical systems form complex structures without external guidance (docs 1-3). But this is a very fertile domain, and I have renamed the document “Spontaneous complexity” after adding docs 6 and 7. The cooperative completion of tasks can arise from simple rules as well: they can be applied to solve other complex problems such as construction, search and rescue and defense (docs 4-5). Docs. 6 and 7 report about newly discovered molecular nano-structures formed by self-assembly (i.e. molecules organize themselves into unique patterns).

Read this and enjoy it, but don't forget the pioneers. If you look up the supplementary animations that are part of (2) (recommended: <https://www.nature.com/articles/s41467-022-34484-2>) you'll be reminded of the work of Conway and Eigen. To prevent you from forgetting them, I have included the obituaries that were published in Nature: John Horton Conway (1937-2020) and Manfred Eigen (1927-2019)

This file contains 12 documents numbered (1) to (3), (3a) and (4) to (11). They are grouped in 5 sets identified by colours.

**(1) Self-organization: What robotics can learn from amoebae**, 2022-11-22  
<https://www.sciencedaily.com/releases/2022/11/221122111436.htm>

**(2) Multi-scale organization in communicating active matter**, 2022-11-07  
<https://www.nature.com/articles/s41467-022-34484-2.pdf>

**(3) Supplementary information** [https://static-content.springer.com/esm/art%3A10.1038%2Fs41467-022-34484-2/MediaObjects/41467\\_2022\\_34484\\_MOESM1\\_ESM.pdf](https://static-content.springer.com/esm/art%3A10.1038%2Fs41467-022-34484-2/MediaObjects/41467_2022_34484_MOESM1_ESM.pdf)

**(3a) Description of animations**  
[https://static-content.springer.com/esm/art%3A10.1038%2Fs41467-022-34484-2/MediaObjects/41467\\_2022\\_34484\\_MOESM2\\_ESM.pdf](https://static-content.springer.com/esm/art%3A10.1038%2Fs41467-022-34484-2/MediaObjects/41467_2022_34484_MOESM2_ESM.pdf)

**(4) The physical intelligence of ant and robot collectives**, 2022-12-21  
<https://www.sciencedaily.com/releases/2022/12/221221135358.htm>

**(5) Dynamics of cooperative excavation in ant and robot collectives**, 2022-10-10  
<https://doi.org/10.7554/eLife.79638>

**(6) AI discovers new nanostructures**, 2023-01-13  
<https://www.sciencedaily.com/releases/2023/01/230113145356.htm>

**(7) Autonomous discovery of emergent morphologies in directed self-assembly of block copolymer blends**, 2023-01-13

<https://www.science.org/doi/10.1126/sciadv.add3687>

<https://www.science.org/doi/epdf/10.1126/sciadv.add3687>

**(8) Swarm intelligence caused by physical mechanisms, Researchers studied swarm behavior of microswimmers**, 2023-01-13

<https://www.sciencedaily.com/releases/2023/01/230113145348.htm>

**(9) Spontaneous vortex formation by microswimmers with retarded attractions**, 2023-01-04

<https://www.nature.com/articles/s41467-022-35427-7>

<https://www.nature.com/articles/s41467-022-35427-7.pdf>

**(10) Obituary of Manfred Eigen**, 2019-02-28

<https://www.nature.com/articles/d41586-019-00731-8.pdf>

**(11) Obituary of John Conway**, 2020-05-23

<https://www.nature.com/articles/d41586-020-01515-1.pdf>

[Updated by Wergosum on 20230125 based on a previous version dated December 2022.

Downloadable from

[https://wergosum.com/wp-content/uploads/2023/01/20230125\\_Spontaneous\\_complexity.pdf](https://wergosum.com/wp-content/uploads/2023/01/20230125_Spontaneous_complexity.pdf)]

## Self-organization: What robotics can learn from amoebae

*Date:* November 22, 2022

*Source:* Ludwig-Maximilians-Universität München

*Summary:* Researchers have developed a new model to describe how biological or technical systems form complex structures without external guidance.

### FULL STORY

---

LMU researchers have developed a new model to describe how biological or technical systems form complex structures without external guidance.

Amoebae are single-cell organisms. By means of self-organization, they can form complex structures -- and do this purely through local interactions: If they have a lot of food, they disperse evenly through a culture medium. But if food becomes scarce, they emit the messenger known as cyclic adenosine monophosphate (cAMP). This chemical signal induces amoebae to gather in one place and form a multicellular aggregation. The result is a fruiting body.

"The phenomenon is well known," says Prof. Erwin Frey from LMU's Faculty of Physics. "Before now, however, no research group has investigated how information processing, at a general level, affects the aggregation of systems of agents when individual agents -- in our case, amoebae -- are self-propelled." More knowledge about these mechanisms would also be interesting, adds Frey, as regards translating them to artificial technical systems.

Together with other researchers, Frey describes in *Nature Communications* how active systems that process information in their environment can be used -- for technological or biological applications. It is not about understanding all details of the communication between individual agents, but about the specific structures formed through self-organization. This applies to amoebae -- and also to certain kinds of robots. The research was undertaken in collaboration with Prof. Igor Aronson during his stay at LMU as a Humboldt Research Award winner.

## From biological mechanism to technological application

Background: The term "active matter" refers to biological or technical systems from which larger structures are formed by means of self-organization. Such processes are based upon exclusively local interactions between identical, self-propelled units, such as amoebae or indeed robots.

Inspired by biological systems, Frey and his co-authors propose a new model in which self-propelled agents communicate with each other. These agents recognize chemical, biological, or physical signals at a local level and make individual decisions using their internal machinery that result in collective self-organization. This orientation gives rise to larger structures, which can span multiple length scales.

The new paradigm of communicating active matter forms the basis of the study. Local decisions in response to a signal and the transmission of information, lead to collectively controlled self-organization.

Frey sees a possible application of the new model in soft robots -- which is to say, robots that are made of soft materials. Such robots are suitable, for example, for performing tasks in human bodies. They can communicate with other soft robots via electromagnetic waves for purposes such as administering drugs at specific sites in the body. The new model can help nanotechnologists design such robot systems by describing the collective properties of robot swarms.

"It's sufficient to roughly understand how individual agents communicate with each other; self-organization takes care of the rest," says Frey. "This is a paradigm shift specifically in robotics, where researchers are attempting to do precisely the opposite -- they want to obtain extremely high levels of control." But that does not always succeed. "Our proposal, by contrast, is to exploit the capacity for self-organization."

---

### Story Source:

Materials provided by **Ludwig-Maximilians-Universität München**. *Note: Content may be edited for style and length.*

---

### Journal Reference:

1. Alexander Ziepke, Ivan Maryshev, Igor S. Aranson, Erwin Frey. **Multi-scale organization in communicating active matter**. *Nature Communications*, 2022; 13 (1) DOI: 10.1038/s41467-022-34484-2

---

### Cite This Page:

---

Ludwig-Maximilians-Universität München. "Self-organization: What robotics can learn from amoebae." ScienceDaily. ScienceDaily, 22 November 2022.  
<[www.sciencedaily.com/releases/2022/11/221122111436.htm](http://www.sciencedaily.com/releases/2022/11/221122111436.htm)>.

# Multi-scale organization in communicating active matter

Received: 14 June 2022

Accepted: 27 October 2022

Published online: 07 November 2022

 Check for updatesAlexander Ziepke<sup>1</sup> , Ivan Maryshev<sup>1</sup>, Igor S. Aranson<sup>2</sup>   & Erwin Frey<sup>1,3</sup>  

The emergence of collective motion among interacting, self-propelled agents is a central paradigm in non-equilibrium physics. Examples of such active matter range from swimming bacteria and cytoskeletal motility assays to synthetic self-propelled colloids and swarming microrobots. Remarkably, the aggregation capabilities of many of these systems rely on a theme as fundamental as it is ubiquitous in nature: communication. Despite its eminent importance, the role of communication in the collective organization of active systems is not yet fully understood. Here we report on the multi-scale self-organization of interacting self-propelled agents that locally process information transmitted by chemical signals. We show that this communication capacity dramatically expands their ability to form complex structures, allowing them to self-organize through a series of collective dynamical states at multiple hierarchical levels. Our findings provide insights into the role of self-sustained signal processing for self-organization in biological systems and open routes to applications using chemically driven colloids or microrobots.

Active matter encompasses a broad class of non-equilibrium systems that transduce energy stored in the environment into mechanical motion. In its most common form, locally interacting, self-propelled agents form coherent collective states that exceed the size of a single agent by orders of magnitude. Examples range from a variety of biological systems such as swimming bacteria<sup>1–3</sup>, cytoskeletal motility assays<sup>4–6</sup>, swarms, and flocks and schools of larger animals<sup>7</sup>, to synthetic self-propelled colloids<sup>8,9</sup> and swarming microrobots<sup>10,11</sup>. There is broad agreement that self-propulsion, local alignment, and random disorientation of simple agents are fundamental microscopic determinants that can explain the occurrence of large-scale collective behavior.

However, in addition to local short-range interactions, such as alignment and collisions, many biological and synthetic systems exhibit various types of long-range signaling strategies. The social amoeba *Dictyostelium discoideum* uses cell-to-cell cyclic adenosine monophosphate (cAMP) concentration waves and chemotaxis to induce aggregation under harsh conditions<sup>12,13</sup>, insects rely on sound to coordinate the formation of cohesive swarms<sup>14</sup>, protein waves control cargo transport<sup>15</sup>, some active colloids form oscillating clusters using

long-range chemical Ag/AgCl coupling<sup>16,17</sup>, microrobots and robotic fish use infrared, electrical and acoustic signals to communicate<sup>18,19</sup>. Signal transduction allows organisms to develop successful survival techniques that give them an evolutionary advantage over non-communicating organisms<sup>20,21</sup>. Communication facilitates the emergence of novel dynamic steady states, such as large streams and localized vortices<sup>13</sup>. Without communication, such states are not generic and are observed only under specific boundary conditions, particle chirality, or density-dependent feedback mechanisms<sup>22,23</sup>. Despite its importance, the role of communication in the context of active matter remains largely unexplored.

A significant body of literature focuses on self-propelled particles with diffusive (chemotactic) interactions. Studies on chemotactic colloids report on the formation of localized clusters and colliding polar bands, both established through motility-induced phase-separation (MIPS)<sup>24–26</sup>. There, the chemical interactions between different agents are mostly linear and passive, e.g., with a constant emission of the signal by the individual agents<sup>27,28</sup>. Distinct from these earlier studies, we ask about the role of an active, non-trivial agent's response (decision-making) to detected signals. The information

<sup>1</sup>Arnold Sommerfeld Center for Theoretical Physics and Center for NanoSciences, Ludwig-Maximilians-Universität München, Theresienstraße 37, 80333 Munich, Germany. <sup>2</sup>Department of Biomedical Engineering, Pennsylvania State University, University Park, PA 16802, USA. <sup>3</sup>Max Planck School Matter to Life, Hofgartenstraße 8, 80539 Munich, Germany. ✉ e-mail: isa12@psu.edu; frey@lmu.de

processing and decision-making should enable the complex hierarchical organization akin to living matter that does not occur in systems with passive chemical signaling.

To reveal the fundamental role of interparticle communication for self-organization, we chose to study a system of self-propelled units (agents) with local polar-alignment interactions. In addition, each agent can perform a specific task, namely, to detect and relay a signal transmitted between agents. Inspired by social amoebae that use cyclic adenosine monophosphate (cAMP) for communication<sup>29</sup>, and Gram-negative bacteria that employ acyl-homoserine-lactone (AHL) molecules as quorum-sensing signals<sup>30,31</sup>, we consider agents that broadcast a signal in the form of a chemical substance into the environment, where it spreads diffusively. Once the local level of the signal exceeds a certain threshold, agents tend to produce and propagate it. Thus, the agents act like a Schmitt trigger, a simple nonlinear electronic circuit with hysteresis<sup>32</sup>. Such a signal transduction system constitutes a spatially extended excitable medium that generically exhibits spiral waves of signaling activity. These waves can control the spatial self-organization of the agents by entraining their direction of self-propulsion. Thus, unlike existing models of amoeboid or bacterial aggregation<sup>33–37</sup>, self-propelled motion, rather than Brownian motion, is the primary mode of transport in our system. In contrast to Vicsek-type models<sup>38</sup>, the model incorporates the ubiquitous signaling found in biological systems. It thus provides insight into specific behaviors such as

aggregation in social amoebae<sup>39</sup> and oscillatory colloids<sup>16</sup> and sheds light on the fundamental properties of active matter consisting of agents with “on-board” signal processing capabilities. The combination of chemical communication and internal information processing leads to an aggregation process involving collective dynamic states at multiple scales. We identify the decision-making machinery of the individual active agents as the driving mechanism for the collectively controlled self-organization of the system.

## Results

### Model

We consider an agent-based description of communicating active matter, in which each agent moves with velocity  $\mathbf{v} = v_0 \mathbf{n}$  and is endowed with signal detection and relaying capability whose activity depends on an internal state variable  $s$ . The dynamics of the agents' positions  $\mathbf{r}_i = (x_i, y_i)^T$  is described by

$$\frac{d\mathbf{r}_i}{dt} = v_0 \mathbf{n}_i + \sum_{j|r_{ij} < 2r_p} f_{ij} \quad (1)$$

where  $\mathbf{n}_i = (\cos\varphi_i, \sin\varphi_i)^T$  is the unit vector in the direction of the  $i$ -th agent's orientation  $\varphi_i$ , with  $i = 1, \dots, N$ ;  $N$  is the total number of agents in the domain. While the speed  $v_0$  of each particle is assumed to be constant, their direction of motion  $\mathbf{n}$  can change—owing to inelastic binary collisions that favor polar alignment (Fig. 1a) or in response to a

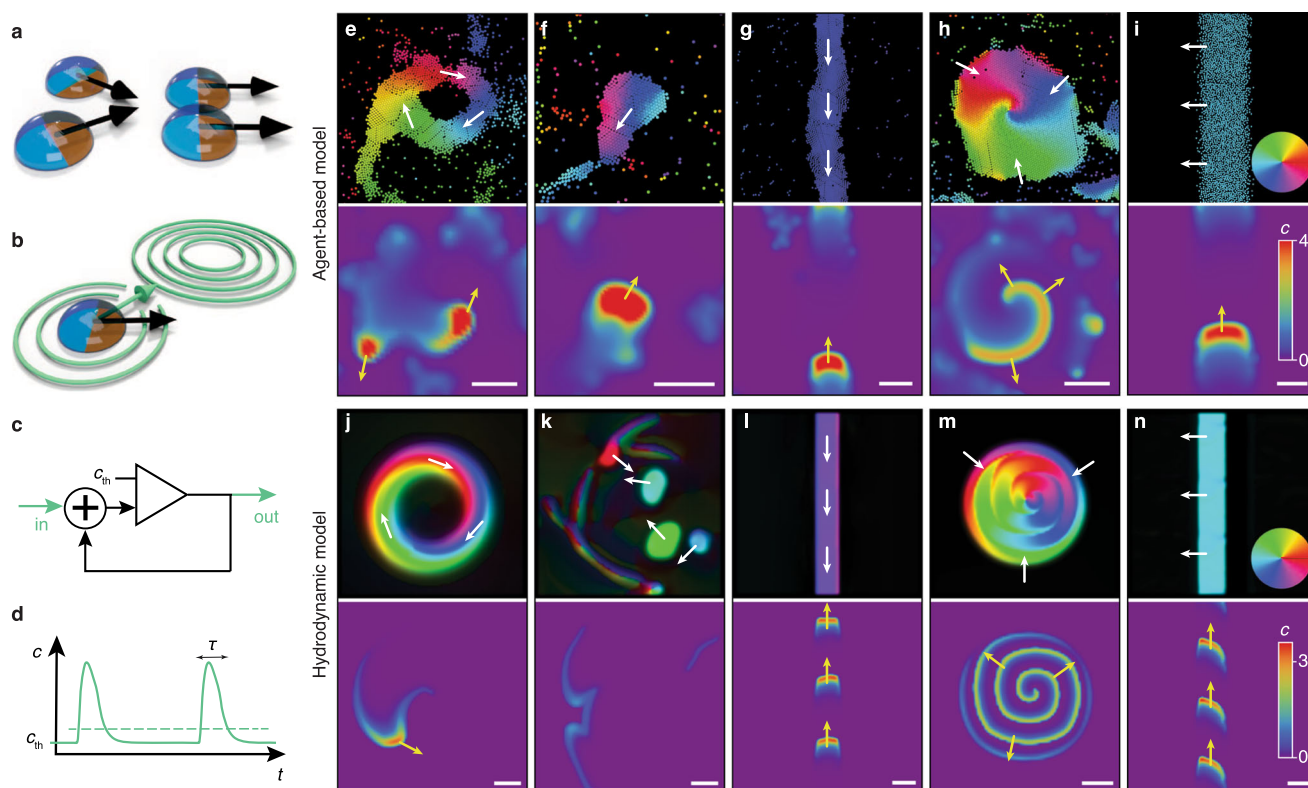


**Fig. 1 | Schematics of the agent-based model for communicating active matter and summary of collective dynamic states.** **a** Polar self-propelled particles undergo alignment in binary collisions. **b** A diffusible signal (green) aligns the cells' orientation vectors. **c** Schematic of a Schmitt trigger with variable threshold  $c_{th}$ . **d** Temporal response  $c(t)$  of the agents' signaling system with characteristic timescale  $\tau$ . **e–n** Representative collective dynamic states in the agent-based (**e–i**) and the hydrodynamic model (**j–n**). The snapshots illustrate aggregation and vortex formation following initial ring formation (**e, j**), where remnant spiral wave arms induce chemical wave propagation in the ring after the spiral core vanished due to

depletion in its center ('whispering gallery'-modes); active droplets (**f, k**), with a collective response to external stimuli; a collective stream (**g, l**), where agents propagate toward the source of communication waves; a large vortex with a spiral wave (**h, m**), and a polar band (**i, n**). White scale bars indicate a length of 10 units. Colors indicate the polar orientation of particles (top panels) and the chemical concentration  $c$  (bottom panels). White and yellow arrows illustrate the direction of motion of the particles (top panels) and the propagation direction of signaling activity (bottom panels), respectively. Parameters are defined in Supplementary Note 3.

chemical signal (Fig. 1b). Within an interaction radius  $r_c$ , agents align in a polar fashion, i.e., the interaction of an agent with a neighbor causes both agents to turn toward the average orientation angle with the alignment rate  $\Gamma$ . If agents approach each other below a critical distance  $2r_p$ , they obey a hard-core repulsion interaction cast as an isotropic short-range force  $f_{ij}$  between the agents in Eq. (1). Akin to chemotaxis, the agents align with a certain sensitivity  $\omega$  along the concentration gradient  $\varphi_c = \tan^{-1}(\partial_y c / \partial_x c)$  of the local maximum of the chemical signal concentration  $c$ . These competing alignment processes are generally error-prone, which is accounted for by a white-noise term  $\xi_i$  with amplitude  $\sqrt{2D_R}$ . Specifically, we assume that the dynamics of the agent's orientation  $\varphi_i$  over time  $t$  is given by the Langevin equation

$$\frac{d\varphi_i}{dt} = -\Gamma \sum_{j|r_{ij}<r_c} \frac{\sin(\varphi_i - \varphi_j)}{|\mathbf{r}_i - \mathbf{r}_j|} + \omega \sin(\varphi_c - \varphi_i) + \xi_i, \quad (2)$$

incorporating binary inelastic collisions between neighboring agents with spatial distance  $r_{ij} = |\mathbf{r}_i - \mathbf{r}_j|$ , chemotactic reorientation of agents along the concentration gradient of chemical signaling molecules<sup>40</sup>, and noise, respectively. The orientation along chemical gradients is implemented similarly to the agents' polar alignment with their neighbors. For instance, in social amoeba the ability of chemotaxis is stable over large ranges of concentrations and alignment can be assumed to be independent of the absolute signal strength<sup>41</sup>.

Signal detection and self-sustained relaying are modeled by a Schmitt trigger (Fig. 1c): if the signal amplitude (i.e., chemical concentration) is above some threshold value ( $c > c_{th}$ ), an agent in a quiescent state ( $s_0 = 0$ ) switches into an excited state ( $s_{ex} > 0$ ), and over a period  $\tau$  it broadcasts the signal (Fig. 1d), i.e., releases a certain amount of the chemical into the environment, where it diffuses (with diffusion constant  $D_c$ ) and is also degraded with rate  $\alpha$ . This yields the chemical signal dynamics

$$\partial_t c(\mathbf{r}, t) = D_c \Delta c - \alpha c + \beta \sum_{i=1}^N f(|\mathbf{r} - \mathbf{r}_i|) \phi(s_i, c), \quad (3)$$

with a Gaussian spatial source distribution  $f(|\mathbf{r}|)$ , Laplace operator  $\Delta$ , and temporal derivative  $\partial_t$ . The agents act as sources of the chemical signal as

$$\beta \phi(s_i, c) = \beta (1 - s_i) \Theta(c - c_{th}), \quad (4)$$

with Heaviside-type signal detection and production rate  $\beta$ . The threshold value  $c_{th}$  as well as the source strength depend on the internal state, whose dynamics, for simplicity, is assumed to be linearly adapting to the signal concentrations,

$$\frac{ds_i}{dt} = \epsilon(c - s_i). \quad (5)$$

The response of the agents' state  $s_i$  to recent stimuli mimics adaptation of receptor sensitivity and productiveness of the signal-emission. Taken together, the model incorporates the fundamental ingredients of a system of self-propelled active matter capable of communication; see "Methods" for a more extensive description of the agent-based model. Exemplary aggregation dynamics of a system without active decision-making are studied in the Supplementary Note 2.

As a complementary approach based on this microscopic model, we derive a hydrodynamic theory formulated in terms of the agents' density field  $\rho(\mathbf{r}, t)$ , the polarization field  $\mathbf{p}(\mathbf{r}, t)$ , the internal state variable  $s(\mathbf{r}, t)$ , and the concentration of the chemical signal  $c(\mathbf{r}, t)$ , all of

which depend on the spatial position  $\mathbf{r}$  and time  $t$ ,

$$\partial_t \rho(\mathbf{r}, t) = -\nu_0 \nabla \cdot \mathbf{p} + D_\rho \Delta \rho, \quad (6)$$

$$\partial_t \mathbf{p}(\mathbf{r}, t) = \sigma(\rho - 1)\mathbf{p} - \delta |\mathbf{p}|^2 \mathbf{p} + D_p \Delta \mathbf{p} - \chi \mathbf{p} \cdot \nabla \mathbf{p} - Q(\rho) \nabla \rho + \rho \omega \nabla c, \quad (7)$$

$$\partial_t s(\mathbf{r}, t) = D_s \Delta s - \alpha s + \rho \beta \Theta(c - c_{th})(1 - s), \quad (8)$$

$$\partial_t c(\mathbf{r}, t) = D_c \Delta c + \epsilon(c - s) - \bar{v} \mathbf{p} \cdot \nabla s. \quad (9)$$

The hydrodynamic model comprises a coupled set of partial differential equations for these fields with basically the same parameters as the agent-based model (see "Methods" for details and Supplementary Note 1 for a derivation of the hydrodynamic theory from the agent-based model). In the absence of communication, e.g.,  $c \equiv 0$ , the parameters  $\sigma$  and  $\delta$  regulate the emergence of polar order above a mean-field critical density  $\rho_c = 1$  when polar alignment interactions outweigh angular diffusion. Based on the large-scale field equations, we can study the dynamics of communicating active matter on length- and time-scales, not accessible with agent-based numerical simulations due to their high computational costs.

### Collective dynamic states

Communicating active matter exhibits unprecedentedly rich spatio-temporal dynamics and collective states, both during aggregation and in the final non-equilibrium steady state. The agent-based model and the hydrodynamic theory show that the emergence of order occurs through the hierarchical formation of distinct collective dynamic states (Supplementary Movie 1). These states include directed particle streams in which the agents move toward the source of chemical waves, ring-like streams with agents migrating along closed paths, compact motile droplets (active droplets), and large vortices that serve as sources of chemical spiral waves (Fig. 1e–n). The juxtaposition of the spatial organization of the particles (Fig. 1e–n, top panels) and the concentration field of the chemical signal (Fig. 1e–n, bottom panels) reveals a tight interdependence between the collective states of active matter and the chemical patterns.

Each of the collective dynamic states has a specific dynamics and a degree of stability. Vortices are well-localized and are stabilized by spiral waves trapped inside these dense aggregates. Their polarization vector  $\mathbf{p}$  is oriented perpendicular to the outer vortex boundary and points inward, preventing agents from escaping and, therefore, stabilizing the vortex (Fig. 1h, m). While vortices are stable and robust, ring-like particle streams (Fig. 1e, j), retained by "whispering-gallery" waves, are long-lived but metastable and are typically engulfed by neighboring vortices (Supplementary Movie 9). Active droplets (Fig. 1f, k) lack an intrinsic source of excitable waves, and their direction of migration is generally determined by external signal gradients. They dissolve in the absence of guiding stimuli. A particle stream (Fig. 1g, l) can be considered a limiting case of a ring-like stream (with an infinite radius of curvature and planar signaling waves). It establishes an efficient collective long-distance particle transfer toward the source of the signaling waves. Finally, we also observe bands resembling the polar bands that develop in non-communicating Vicsek-like models<sup>5</sup> (Fig. 1i, n). However, if agents in polar bands are coupled to chemical signaling waves propagating along the bands, as shown in Fig. 1i, n, this will induce a change of the agents' orientation and may lead to a transition toward stream-type solutions as depicted in Fig. 1g, l.

Given these phenomenological observations, we ask two fundamental questions: How can different collective dynamic steady states be selected by tuning characteristic properties of the particle dynamics and the communication process? How can one characterize

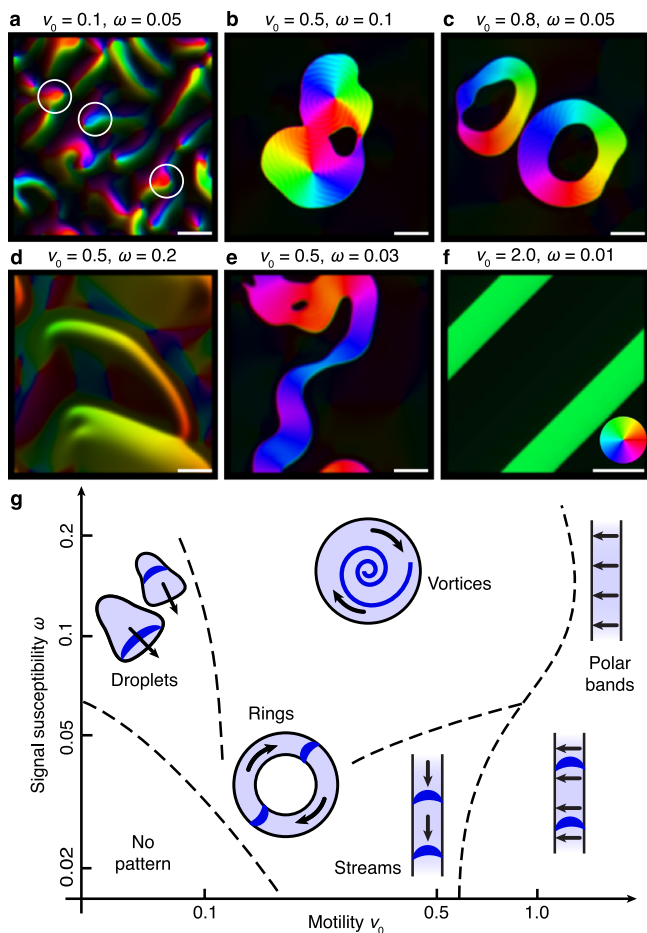


**Fig. 2 | Principal collective dynamic states in the hydrodynamic model.** The phase diagram of dominant (meta-stable) dynamic states in the  $\omega - \nu_0$  (signal susceptibility and motility) parameter space is shown in the lower panel **g**, and snapshots of corresponding numerical simulations of the hydrodynamic model, starting from a homogeneous initial density  $\rho_0 = 0.6$  and random initial excitations of the signaling system are depicted in the upper panels. Colors indicate the polar orientation within the aggregates. **a** Active droplets (three are highlighted by white circles), **b** vortex states, **c** ring solutions, **d** “silent” polar bands, **e** streams, **f** polar bands with signaling activity. See Supplementary Movies 2–7. The polar relaxation rate is set to  $\sigma = 0.02$ , remaining parameters are given in Supplementary Note 3. White bars indicate a length of 50 units.

the hierarchical self-organization process and quantify the information processing involved?

Figure 2 shows the (qualitative) phase diagram with the representative collective dynamic states as a function of the agents’ motility and signal sensitivity. In contrast to the isotropic-polar transition in Vicsek-type systems at  $\rho = 1^{42}$ , order here emerges at much lower densities, depending on the signal sensitivity (Supplementary Figure 1). This is due to the alignment of the polar particles with the collectively established signaling field. At a given particle density, the dominant collective dynamic state in the asymptotic non-equilibrium steady state is determined by the relative fraction of motility and signaling effects. Vortices and rings are the dominant structures in a parameter regime with low motility and high signaling sensitivity. Thereby, vortices exhibit a balance between the persistent self-propulsion promoting agents away from the localized vortices and chemotactic attraction toward the vortex’ center due to persistent spiral wave activity in the signaling field. If self-propulsion outweighs the attractive force established by collective signaling, vortices split up, and ring-like states become the predominant solution. If self-propulsion is rather weak and dominated by diffusion

effects, the steady-state is governed by active droplets. Conversely, for vanishing signal sensitivity, the model reduces to a Vicsek-type model<sup>38</sup>, and only polar bands are found. These can either host persistent signaling activity or remain in the quiescent state of the signaling machinery, just like system-spanning polar bands in Vicsek-like models.

Next, we asked how the hierarchical aggregation process from a disordered arrangement of particles to the final non-equilibrium steady state can be understood based on our characterization of the various collective dynamic states (Fig. 1). To this end, we focus on a parameter regime with intermediate polarity relaxation times and a balance between motility and signaling effects, which ultimately gives rise to vortex states.

### Hierarchical self-organization

Our agent-based simulations and numerical integration of the hydrodynamic theory consistently show that the hierarchical self-organization process is facilitated by an intricate interplay of self-propulsion, signaling, and information processing (Fig. 3, Supplementary Movie 8). Initially, small-scale density fluctuations form, out of which droplets, streams, and small clusters later emerge. These initial aggregation processes are facilitated by short distance signaling waves and a local mutual entrainment. At later stages, the aggregation is orchestrated by spiral waves of signaling activity. Interestingly, there is competition between the spiral waves: Those that occupy larger and denser areas (mounds) accordingly have a higher frequency and displace smaller spiral waves (Supplementary Figure 2). As a result, higher particle density provides a positive feedback mechanism that favors the formation of larger aggregation centers<sup>43</sup>. The aggregation stage is characterized by competition between particle clusters, which is quite different from that of non-signaling active matter [e.g., motility-induced phase separation (MIPS)], where the number of clusters scales as  $N_c \sim t^{-\eta}$  with  $\eta \approx 2/3^{44}$ . In our hydrodynamic model, we observe multi-scaling behavior, indicating qualitatively distinct types of processes (Fig. 3a, b) for the time evolution of the cluster number and the density and polarization fields. Initially, we observe  $N_c \sim 1/t$  (Fig. 3a), consistent with interface-controlled Ostwald ripening of clusters<sup>45</sup>. Once the streams have formed, there is a qualitative change in the aggregation process. The aggregation rate is now limited by the persistent directed motion of clusters and streams which migrate toward the aggregation centers. This leads to a much faster decay of the cluster number, even compared to the ballistic coalescence of clusters which would correspond to  $\eta = 2$ . This ‘streaming phase’ is followed by the formation of a few localized vortices that contain most agents. Due to the low particle density in between the vortices and the resulting lack of signal transmission, the interaction between these structures is strongly attenuated, and the coarsening process is slow. Since the signaling field decays exponentially (with diffusion length  $L_c \sim \sqrt{D_c/\alpha}$ ), one expects a logarithmic coarsening law  $N_c \sim 1/\ln t^{46}$ , consistent with the slow decay seen in our numerical data (Fig. 3c).

Thus, the ability to process information and make decisions results in the radically different organization of polar active matter. Ordering begins below the threshold of the polar-isotropic transition. The process leading to the formation of large vortices as robust attractors in the final stage of aggregation is much faster than that observed in non-signaling active matter or active matter with passive chemical signaling<sup>24</sup>. This is because it can exploit multi-scale collective intermediate states, whose respective frequencies are quantified in Fig. 3c. This classification confirms the observed phenomenology. The initial phase is dominated by coarsening of droplets. Once organizing vortices emerge, they establish persistent signaling waves. This causes a rapid decrease in the number of droplets and induces progressive aggregation through the formation of streams toward the vortices. In the final phase, a slow coarsening process occurs among

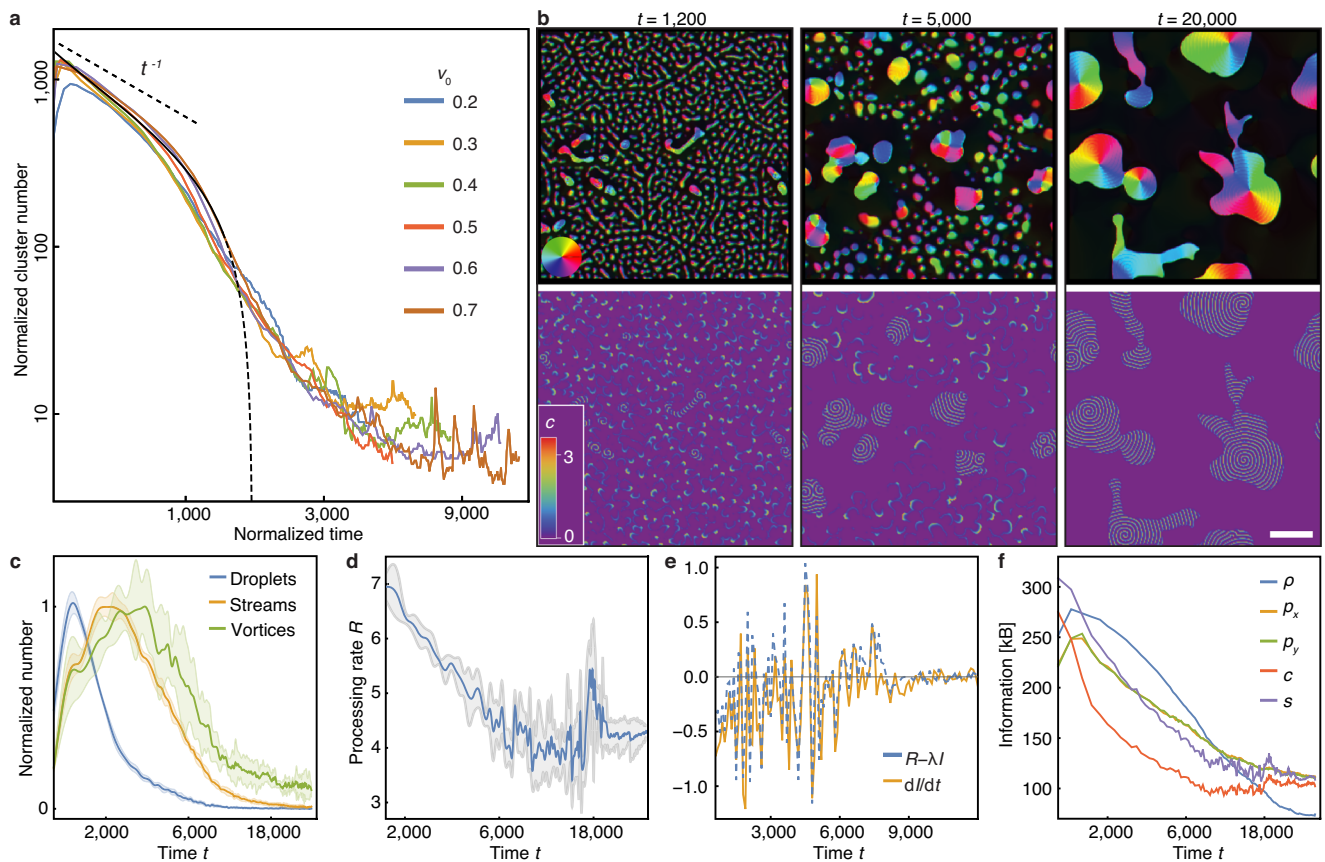


**Fig. 3 | Hierarchical self-organization and information processing.** **a** Time dependence of the cluster number  $N_c$  for different values of the mobility parameter  $v_0$  in rescaled quantities  $t \cdot v_0$  and  $N_c/\sqrt{v_0}$ . The unlabeled black line indicates the estimate  $N_c \sim (N_0 - \kappa t^2)/t$ . **b** Simulation snapshots at time  $t$ , displaying droplet ripening, vortex-controlled aggregation, and merging of vortices. The scale bar indicates a length of 100 units. Colors indicate polar orientation (top panels) and signaling concentration (bottom panels), respectively. **c** Time-resolved classification of collective dynamic states averaged over six simulation runs; the lighter shades define intervals of standard deviations. Initially, droplets grow and

aggregate to form streams and vortices. **d** Time evolution of the information processing rate  $R$  of the signaling system and standard deviations (gray) averaged over six simulation runs. **e** Comparison of the rate of change  $dI/dt$  of the stored information as predicted from Eq. (10) (blue) and the temporal derivative of compressed file sizes (orange). **f** Time dependence of the information content of the various fields, Eqs. (6)–(9). Parameters are  $\omega = 0.05$  and the values given in Supplementary Note 3. Panels **b–f** show simulation results and analysis for  $v_0 = 0.5$ . See “Methods” for details.

the vortices with a corresponding logarithmic decrease in their number.

### Information processing drives self-organization

Since each agent is endowed with a decision-making capability, we also sought to characterize the course of information processing during the multi-scale hierarchical aggregation process. To this end, we quantified the time evolution of the information content  $I(t)$  in the system, using the computable information content of a lossless compressed configuration of the physical fields  $c$ ,  $\rho$ ,  $\mathbf{p}$ , and  $s$ <sup>47,48</sup>. In particular, we consider the file sizes obtained by the Lempel-Ziv-Welch compression algorithm<sup>49</sup> as implemented in the PNG file format (see “Methods”). The system’s information content changes over time as individual agents process information in response to external stimuli employing their self-propulsion and intrinsic signal processing capability (Schmitt triggers). In the absence of signaling, self-propulsion and local interactions are unable to create order at subcritical densities due to dominant angular diffusion; accordingly, the information content will decline exponentially with some decay rate  $\lambda$  as the system approaches the disordered homogeneous state. Here, however, there is information processing which leads to self-organization and induces order. We quantify the information processing by the rate  $R$  of agents transitioning to the refractory state, i.e., agents that emit a signal in response to a stimulus and therefore process information (Fig. 3d).

Altogether, we expect the system’s information content to follow the dynamics

$$\frac{dI}{dt} \sim R - \lambda I, \tag{10}$$

with a fitting parameter  $\lambda$ . That, in turn, implies that the temporal change in the stored information depends exclusively on the initial information content and the measured processing rate  $R$ .

The basic hypothesis, Eq. (10), is validated by our numerical simulations (Fig. 3e). On a qualitative level, it agrees very well with the predicted evolution of information content. In particular, the prediction captures not only the overall trend but also coincides with important landmark points of the evolution. This affirms our assertion that the signaling machinery is key for information processing and the driving mechanism behind self-organization in the system.

The rate of change of the encoded information approaches a final state in which the order generated by persistent signaling offsets the loss of correlation created by the agents’ self-propulsion.

An analysis of the amount of information stored in the various fields also reveals the different stages of the aggregation process (Fig. 3f). We observe that the amount of information stored in the density field decreases and eventually approaches a comparably low value once the mass has accumulated in only a few stable vortices. This

reflects the results of the cluster number analysis (Fig. 3a), including the qualitative change in aggregation dynamics between the dominance of ripening and the dominance of the guided movement of active droplets. In contrast to the homogeneous density field, the information content of the polarity field saturates at higher values, which correlates with the presence of persistent vortex states. Interestingly, the information content of the chemical concentration field  $c$  exhibits a super-exponential decay. This confirms that information processing is mainly performed by the signaling machinery, which makes it an essential factor in the organization of the aggregation process. Moreover, it approaches its baseline information level earlier than the density field, indicating the transition toward the phase of nearly isolated vortex states.

## Discussion

In conclusion, we have introduced a new class of active matter equipped with self-sustaining signaling capabilities: it allows self-propelled agents to communicate and process information. Communication and decision-making enable hierarchical self-organized aggregation to emerge via a sequence of distinct collective dynamic states.

While our model is generic and does not rely on specific biological or chemical details, the observed phenomenology closely resembles the aggregation dynamics of social amoebae, including the formation of stable vortices<sup>13</sup> and metastable rings<sup>50</sup>. Communication induces a non-trivial self-organized attraction that gives rise to the formation of a rich variety of collective dynamic states. The exhibited behavior in terms of collective dynamic states and the collectively controlled aggregation process is a clear advance compared to current models of chemotactic colloids. Besides the variety of observed states, communication and active information processing introduce a new framework of collective organization. It allows for much faster aggregation times and a controlled competition between aggregation centers as high-density clusters can enlarge their basin of attraction.

There are several potential extensions to the model, such as locally coupled self-propelled relaxation oscillators, signaling nematic active matter, or self-propelled agents coupled via sound or electromagnetic waves, which may have direct relevance to technological applications such as self-organizing swarms of minimal drones or functional microrobots. Information processing could be introduced by modifying the chemistry of colloids and droplets, thus allowing experimentally accessible realizations to be directly established for silver-chloride Janus colloids exhibiting chemical oscillations and synchronization<sup>16,17</sup>, and for self-propelled emulsions hosting the Belousov-Zhabotinsky reaction<sup>51</sup>, to name but two. Decision-making can also be implemented using simple electronic circuits in mass-manufactured microrobots. These may open new avenues for applications of active matter in nanoscience and robotics.

## Methods

### A detailed description of the agent-based model

In the agent-based model, we consider self-propelled particles with radius  $r_p$  in a two-dimensional square periodic domain with side length  $L$ . The particles move with constant speed  $v_0$  in the plane. The dynamics of the agents' positions  $\mathbf{r}_i$  is described by Eq. (1). The direction of movement can be changed by polar alignment during collision events, chemotactic responses to signaling molecules, or stochastic fluctuations. If two agents come within a distance of less than  $2r_p$ , they are repositioned according to the following hard-core repulsion rule: overlapping particles are shifted in the direction of their distance vector by equal amounts until a distance of  $2r_p$  is restored. Within an interaction radius  $r_c > 2r_p$ , agents align in a polar fashion, i.e., the interaction of an agent  $i$  with a neighbor  $j$  causes both agents to turn toward the average orientation angle with the alignment rate  $\Gamma$ . The agents also align with the direction  $\varphi_c = \tan^{-1}(\partial_y c / \partial_x c)$  of the local

maximum of the chemical signal concentration  $c$  with the susceptibility coefficient  $\omega$ . Both alignment interactions are imperfect, which we account for by adding zero-mean white noise  $\xi_i$  with amplitude  $\sqrt{2D_R} : \langle \xi_i(t) \xi_j(t') \rangle = 2D_R \delta_{ij} \delta(t - t')$ . In total, the dynamics of the agent's orientation  $\varphi_i$  is given by the Langevin equation, Eq. (2).

The system of agents establishes self-sustaining chemical signaling as a means of information processing and transmission. Each agent is equipped with an internal state variable  $s_i \in [0,1]$  that determines whether or not it perceives the environment and transmits signals by emitting a chemical substance. We take the magnitude of  $s_i$  to be the refractoriness of an agent to external signals, i.e., a measure of how responsive it is to relay a signal:  $s_i = 0$  then corresponds to the state with the lowest refractoriness (highest susceptibility). The agents are assumed to sense the environment by linearly adapting to the local concentration level  $c$  of the chemical field with rate  $\epsilon$ , Eq. (3), and act as nonlinear sources of the chemical signal  $c$ . This release of chemicals depends on both the internal state of the agents and the environment. We assume the source strength to be of the threshold form, Eq. (4), where  $\beta$  denotes the release rate and  $c_{th}$  a threshold above which agents can detect and relay signals and below which they remain quiescent;  $\Theta(x)$  denotes the Heaviside step function with

$$\Theta(x) \equiv \begin{cases} 1 & , \text{ for } x > 0, \\ 0 & , \text{ else.} \end{cases} \quad (11)$$

The agent's signaling receptors are assumed to undergo state-dependent changes in susceptibility that implement potential saturation effects and adaptation to varying levels of signaling molecules in the environment. Specifically, we take the threshold value  $c_{th}$  to be a linear function of the state variable  $s_i$ ,

$$c_{th}(s_i) = \frac{s_i + b}{a}, \quad (12)$$

implementing a higher threshold for signal detection at larger state values of the refractoriness  $s_i$ . The parameter  $b$  sets the baseline threshold and the factor  $1/a$  specifies the linear increase of the threshold  $c_{th}(s_i)$  with growing state values. In addition, to implement the agents' ability to process detected signals and respond to them, the release of chemicals shall depend on the internal state  $s_i$  of an agent: In terms of their signal production, agents in the most susceptible state ( $s_i = 0$ ) react most vigorously to super-threshold stimuli. The rate of signal release is assumed to decrease linearly  $(1 - s)$  with increasing  $s_i$ . Note that for the set of parameters used in this study, Supplementary Note 3, the states  $s_i$  do not exceed values of one. Therefore, agents are always either quiescent and do not contribute to the chemical signaling field or act as sources for it.

Taken together, the interplay between the internal dynamics  $s$  and the chemical field  $c$  in a well-mixed environment is given by

$$\frac{ds}{dt} = \epsilon(c - s), \quad (13)$$

$$\frac{dc}{dt} = -\alpha c + \beta \phi(s, c), \quad (14)$$

which also accounts for degradation of the emitted signal at a rate  $\alpha$ . Equations (13) and (14) constitute a nonlinear two-component system, which shows excitable behavior; see Supplementary Fig. 3a for an illustration of the phase-space flow. The quiescent state, corresponding to  $c = s = 0$ , is linearly stable and has a finite domain of attraction. However, if for  $s = 0$  the input signal  $c_{in}$  exceeds the threshold  $c_{in} > c_{th}(s = 0) = b/a$ , the system performs a long excursion in phase space before returning to  $c = s = 0$ ; see the red phase space trajectory in Supplementary Fig. 3a. Note that the amplitude of the response (extent

of the red trajectory in phase space) is mainly determined by the phase-space flow and only weakly depends on the initial input strength  $c_{in}$ . This ensures a sufficiently strong transmission of any super-threshold signals. The phase-space trajectory in Supplementary Fig. 3a yields the excitation pulse displayed in Supplementary Fig. 3b, which shows fast excitation and emission of signals and a slower refractory dynamics that restores the susceptible state ( $c = s = 0$ ). The duration of the refractory period  $\tau$  is determined by the inverse of the relaxation rate  $\epsilon^{-1}$ .

Taken together, the excitable dynamics resemble the behavior of a Schmitt trigger (Fig. 1c), a circuit with closed negative feedback, which exhibits hysteresis-like dynamics representative of e.g., relaxation oscillators. In particular, the appropriate delay between the fast production of signaling molecules and the slower adaptation of the agent's internal state can be achieved by choosing  $\beta/\epsilon \gg 1$ , resulting in a relaxation dynamics with a rapid response to a stimulus followed by a slower refractory period. Model parameters are summarized in Supplementary Note 3.

To formulate the spatial dynamics of the signaling molecules in terms of a concentration field  $c$ , one must specify how the molecules emitted by the agents are distributed in their vicinity. We use a source distribution given by a normalized Gaussian profile  $f \sim \exp[-(x^2 + y^2)/(2w^2)]$  with characteristic width  $w \equiv 2r_p$ . In addition, we account for the center-of-mass diffusion (with diffusion coefficient  $D_c$ ) and degradation with rate  $\alpha$ , so that together with the source terms for each agent one obtains Eq. (3). We choose the decay rate  $\alpha$  to be of the same order of magnitude as the positive source contributions, terms  $\sim \beta$ , to the signaling field  $c$  for average agent densities. On the scale of individual agents, signal diffusion is assumed to be fast compared to the agents' self-propulsion velocity,  $1 \ll D_c/(r_p v_0)$ . The parameters used in the numerical simulations are specified in Supplementary Table 1.

### A detailed description of the hydrodynamic model

In this section, we give a detailed description of the hydrodynamic model, Eqs. (6)–(9), that we introduced in the main text for communicating active-matter systems. This dynamic field theory is formulated in terms of a set of evolution equations for the following fields: the number density of particles  $\rho$ , the vector order parameter characterizing the particles' local average polar alignment  $\mathbf{p} = \langle \mathbf{n}_i \rangle$ , the concentration of the signaling species  $c$ , and the state of refractoriness  $s$ . A representative vortex solution with internal spiral-wave activity of the signaling fields is shown in Supplementary Fig. 3a. We observe an approximately circular high-density cluster within which the particle orientation revolves around its center and aligns with the density gradients at the interface to the outer low-density regime. This vortex state is accompanied by the emergence of a spiral wave established inside the high-density domain by the chemical field and the adapting signaling states of the agents.

The time evolution of the agent's density field  $\rho(\mathbf{r}, t)$ , Eq. (6), is given by an advection-diffusion equation, which accounts for advective transport due to the particles' self-propulsion with speed  $v_0$  and diffusion of the center of mass with diffusion constant  $D_p$ . The center-of-mass diffusion has no direct counterpart in the agent-based model as it has been neglected there. However, for completeness and to regularize density gradients, it is included in the hydrodynamic theory.

The direction of self-propulsion, described by the polar field  $\mathbf{p}(\mathbf{r}, t)$ , can be changed by interparticle interactions, stochastic fluctuations, and signaling-induced reorientations: The first three terms in Eq. (7) for the time evolution of the polarity field correspond to a time-dependent Ginzburg-Landau model describing the dynamics close to an isotropic-polar phase transition; units for the density  $\rho$  are chosen such that the critical density is set to unity. The persistence parameter  $\sigma$  defines the relaxation time, the parameter  $\delta$  sets the magnitude of polar order, and  $D_p$  implements the elasticity in a one-Frank-constant approximation. Moreover, to make the model more general, we include a term  $\chi \mathbf{p} \cdot \nabla \mathbf{p}$

that accounts for self-advection. In the numerical simulations, the corresponding parameter  $\chi$  is set to a small value and does not contribute critically to the qualitative behavior of the system. The coupling between the orientational order and density combines both self-advective and steric effects incorporated in the function

$$Q(\rho) = \frac{v_0}{2} [\exp(-32\rho) + \exp(16(\rho - 2))]. \quad (15)$$

The steric effects can be modeled as an effective pressure. As derived in Supplementary Note 1, see Supplementary Eq. (11), we include the low-density contribution as an amplitude  $Q(\rho \rightarrow 0) = v_0/2$ . For increasing densities, we assume that collective effects arising from particle interactions counteract the steric repulsion, and therefore reduce the amplitude of the function  $Q(\rho)$ . Complementing this, for high densities, the effective pressure contributions outweigh the collective effects again due to the finite volume of agents. Therefore, the amplitude  $Q(\rho)$  increases at a critical maximum density of  $\rho = 2$ . The coupling of the polar order to signaling encoded by the chemical concentration field enters in Eq. (7) via the term  $\omega \nabla c$ . It describes the alignment of the polarization field in the direction of the local maximum of the signal concentration  $c$  with susceptibility parameter  $\omega$ .

The dynamics of the chemical concentration field  $c$ , Eq. (8), is a direct transfer from the agent-based model, Eq. (3). Coarse-graining the equation, we replace the discrete sum of Gaussian source terms  $\sum_i f(|\mathbf{r} - \mathbf{r}_i|)$  by a density-dependent continuous contribution  $\sim \rho(\mathbf{r}, t)$ .

The dynamics of the state variable  $s$ , Eq. (9), includes diffusive, reactive, and advective contributions. Here, the first term simply corresponds to the center-of-mass diffusion of the agents as in Eq. (6). The second term corresponds to the relaxation of the local state variable  $s$  to the corresponding local value of the signaling field  $c$ , where  $\epsilon$  denotes the relaxation rate.

Therefore, the magnitude of the rate  $\epsilon$  controls the timescale over which the internal signaling state  $s$  adapts to the chemical concentrations  $c$ . Finally, the term  $\sim \mathbf{p} \cdot \nabla s$  incorporates the local change of the agents' signaling states  $s$  by means of their self-propulsion. The regularizing prefactor  $\bar{v} = v_0 \tanh(|\mathbf{p}|/\rho)/|\mathbf{p}|$  ensures the boundedness of effective self-propulsion velocities for low densities  $\rho \rightarrow 0$ .

### Numerical implementation

We integrate the agent-based model, Eqs. (1)–(5), on a square periodic domain with side length  $L$  over discretized time intervals  $\Delta t$ . For each time step, the continuous particle positions and orientations are updated following Eqs. (1), (2) and the hard-core repulsion rule, using an Euler-Maruyama scheme. For efficient identification of potential interaction partners at each time step, particles are assigned to virtual grid cells. We check for collisions within a particle's grid cell and its surrounding cells. Agents that pass through a virtual grid cell's boundaries are reassigned to their new grid cell. Based on the updated agent positions, we compute the agents' source contributions,  $\sim \beta$  to the continuous signaling field  $c$ . Subsequently, we solve the temporal dynamics of the signaling field, Eq. (3), in Fourier space by a forward Euler integration scheme and then obtain the representation in real space by inverse Fourier transform. We apply a fast Fourier transform algorithm for these transformations. Concluding the calculations for a given time, we update the internal states of the agents using the same forward Euler time integration scheme for Eq. (5). For the simulations with 4000 agents, shown in Fig. 1, we use a total system size of  $200 \times 200$ , resolved by 200 Fourier modes per spatial direction and a time step of  $\Delta t = 0.01$ . The depicted solutions are neither dependent on the selected spatial or temporal resolution which we verified by corresponding simulations with higher accuracy.

The set of continuous hydrodynamic Eqs. (6)–(9) is solved in a square periodic domain by a quasi-spectral method and a semi-implicit time integration with discretized time steps  $\Delta t$ .

For each time step, we make use of fast Fourier transform of the field quantities to calculate their spatial derivatives. Also, we compute the Fourier transform of the nonlinear contributions to the dynamics, and apply an exponential time differencing scheme of second order (ETD2) to integrate the complete set of equations in Fourier space over a time interval  $\Delta t$ <sup>52</sup>. In doing so, all linear contributions to the dynamics, Eqs. (6)–(9), are implicitly solved for, while nonlinearities are included explicitly via their first-order forward finite difference approximation. The eigenvalues and pseudoinverse of the matrix representation of the linear dynamics of Eqs. (6)–(9), necessary for ETD2, are calculated once at the beginning of the runtime using the linear algebra library Eigen<sup>53</sup>. We initialize the system with homogeneous densities and polarity fields with small zero-mean white noise perturbations. The chemical system is initialized by exciting randomly positioned and oriented two-dimensional Gaussian kernels of characteristic lengths ranging from 20 to 30 units and widths of 5 units. The model parameters are given in Supplementary Note 3. For all simulations, time steps and spatial resolutions have been adapted to optimize runtime while ensuring that results do not depend on the chosen discretization.

### Quantification of the aggregation process

The self-sustaining signaling mechanism we consider has a threefold effect on the formation and organization of large-scale structures in the active polar system. Firstly, signaling enables pattern formation from a homogeneous density, even below the critical density ( $\rho_c \equiv 1$ ) for the polar ordering transition. Secondly, stronger chemotactic susceptibility of the polar orientation to the established signaling significantly increases the rate of the self-organization process, as can be seen in Supplementary Figure 1. Starting from an initially spatially uniform density  $\rho_0$ , the aggregation times  $T_{\text{aggr}}$  for crossing the isotropic-to-polar ordering transition at  $\rho_c \equiv 1$  decrease significantly for larger signal susceptibilities  $\omega$ . And thirdly, spiral waves as sources of persistent signaling activity can stabilize the emerging vortex structures, as can be seen from the results of the numerical simulations, e.g., Fig. 3. To gain a better understanding of the principles underlying the signal-driven self-organization process and to quantify the degree and type of ordering, we use cluster classification analysis and quantify the time evolution of the information content in the system. Both methods are presented in more detail below.

In our numerical simulations, we observe that distinct collective states dominate the different phases of aggregation; see Fig. 3, Supplementary Movie 8. During an initial phase, droplets of agents are formed and undergo Ostwald-type ripening. Once spiral waves are established as persistent signaling sources, the droplets show directed motion toward the strongest of these sources, i.e., they become ‘active’ droplets. The coalescence of these active droplets leads to the formation of collective density streams. Eventually, streams and active droplets approach the source of the organizing signal, where they condense into stable clusters. The interplay of aggregation due to the intrinsic signaling and the self-propulsion of the polar active matter typically results in localized vortex solutions. As a means of classifying the various collective states discussed above, namely droplets, streams and vortices, we analyze clusters with densities  $\rho > 0.7$  (above the system’s average density, which we typically set to  $\rho_0 = 0.6$ ) by quantifying their total mass, spatial extension along their main axes, and the direction of the effective self-propulsion of the cluster. The latter represents the direction of the cluster’s center-of-mass motion,  $\sim \int \mathbf{p}(\mathbf{r}, t) d\mathbf{r}$ . In particular, we measure the spatial extension of clusters along their main axes (axes with largest spatial extent), the angle between the main axis and the averaged cluster polarity, and the intrinsic vorticity  $\nabla \times \mathbf{p}$  of the orientational field.

We classify a given aggregate as a stream if the shape factor (the ratio of major to minor diameter) is larger than 1.4 and the angle between the major axis and polarity is smaller than  $\pi/4$ ; if the shape

factor is less than 1.4 and the mean vorticity inside the domain exceeds a value of 0.01, the aggregate is classified as a vortex. Clusters characterized as neither streams nor vortices are classified as droplets. Information about domain position, orientation and shape is obtained by using the first three central moments of the binarized domain with density threshold  $\rho = 0.7$ .

As a measure for emerging order in the system, and to quantify the impact of the signaling machinery on the aggregation process, we consider the total amount of information stored in the system. Following references<sup>47,48</sup>, the information content can be obtained by lossless compression of the system’s data, i.e., the data points of the discretized continuous fields, Eqs. (6)–(9), for a given time. We analyze the fields at discrete time points with step size  $\Delta t = 200$  for total simulation times of  $t_{\text{sim}} = 40,000$ . In order to measure the information content of the system for a given time, we saved the data of all the separate fields into a collective image with a spatial discretization of 128 by 128 pixels per field and 256 gray values per pixel. Subsequently we use the lossless compression in the PNG format to compute the stored information content. The resulting file sizes then give a corresponding amount of stored information as discussed in the main text; see Fig. 3e, f. Information processing in the system is facilitated by two distinct processes: polar ordering due to pairwise collisions and decision-making of the individual signaling units, as specified by the excitable signaling field dynamics. Below the isotropic-to-polar transition at the critical density ( $\rho_c = 1$ ), the disordering effect of the agent’s angular diffusion dominates over their ordering alignment dynamics, such that in the absence of chemical signaling the system must relax toward a homogeneous disordered state. This relaxation process is expected to proceed at a rate  $\lambda$ . As an organizing factor, the signaling machinery counteracts the natural trend of the polar active-matter system toward the homogeneous state. We hypothesize that most of the information processing occurs through the signaling machinery, and we quantify its activity by the information processing rate  $R$ . The latter is represented by the area fraction of the excitable system in the refractory state. Specifically, we define this state as exhibiting a super-threshold concentration in the chemical signaling field,  $c > 1$ . Taken together, we posit that the time evolution of the stored information content  $I$  can be approximated as given in Eq. (10). By means of this dynamic equation, and based on the assumption that information in the system is mainly processed by the signaling machinery, we are able to predict the temporal evolution of the total stored information. Starting from a value of the system’s initial information content, and supplied with the time-dependent processing rates  $R$ , Eq. (10) allows for a prediction of the temporal dynamics of the stored information. The comparison between this prediction and the actual dynamics of the stored information content quantified by the file size of the lossless compressed data at a given time in Fig. 3e yields good agreement. This again validates the basic assumption of signaling-mediated information processing in the system.

Based on the cluster classification and cluster number analysis, we can quantify the three main stages of the aggregation process described above and in the main text; see also Fig. 3 and Supplementary Movies 1 and 8. In the following, we describe the basic modes of mass aggregation in terms of the efficiency of the processes. Consider a system of droplets of equal size, concentration  $n$  and diffusion coefficient  $D \sim S^\gamma$ , with a yet-to-be determined exponent  $\gamma$  relating the diffusion to the droplet sizes  $S$ . For diffusion-limited coalescence of droplets in two spatial dimensions, the time dependence of droplet sizes and numbers is given by<sup>54</sup>

$$S \sim t^z, N_c \sim t^{-z}, \quad (16)$$

where the exponent  $z$  can be determined from the hydrodynamic equations underlying the aggregation process at the corresponding stages. For instance, the probability of coalescence in a binary collision

process is given by  $n^2$ , and thus, the mean-field equation for the droplet density  $n$  reads

$$\frac{dn}{dt} = -D(S)n^2 = -D_0 S^\gamma n^2. \quad (17)$$

Substituting the expressions for  $S$  and  $n$ , one obtains for the exponent

$$z = \frac{1}{1-\gamma}. \quad (18)$$

For the case where diffusion does not depend on the cluster size,  $\gamma=0$ , one obtains  $N_c \sim 1/t$ . This behavior is similar to the interface-controlled Ostwald ripening for which the coarsening of droplets is independent of their diffusive motion. In addition, our hydrodynamic model gives rise to directed motion of active droplets, which is guided by organizing spiral waves. Including the guided movement of active droplets toward the organizing vortices, one can estimate the cluster number dynamics by

$$N_c(t) \sim (N_0 - \kappa t^2)/t, \text{ with } \kappa > 0. \quad (19)$$

This estimate incorporates the directed ballistic motion of clusters toward a collective aggregation center  $\sim N_0 - \kappa t^2$ . Moreover, these clusters may still exhibit interface-driven coarsening, which is accounted for by an additional factor  $t^{-1}$ . Thus, the estimate captures the main behavior of the first two aggregation stages, which are dominated by Ostwald ripening and coordinated movement of droplets toward spiral waves as organizing centers. This becomes manifest in a good qualitative agreement between the estimate and the measured evolution of the cluster number as shown in Fig. 3a, with fit parameters  $N_0 = 382,000$  and  $\kappa = 0.15$ . However, at longer times, vortex-vortex competition, which is not accounted for in the given estimate, becomes increasingly important. Therefore, the deviations between the estimated and measured dynamics of the cluster numbers grow as the aggregation process progresses.

## Data availability

The data that support the findings of this study are available in the main text, methods, and supplementary information. Additional information is available from the corresponding authors upon request.

## Code availability

The code used in this study is available from the corresponding authors upon request.

## References

- Sokolov, A., Aranson, I. S., Kessler, J. O. & Goldstein, R. E. Concentration dependence of the collective dynamics of swimming bacteria. *Phys. Rev. Lett.* **98**, 158102 (2007).
- Aranson, I. S. Bacterial active matter. *Rep. Prog. Phys.* **85**, 076601 (2022).
- Decoene, A., Lorz, A., Martin, S., Maury, B. & Tang, M. Simulation of self-propelled chemotactic bacteria in a stokes flow. *ESAIM: Proc.* **30**, 104–123 (2010).
- Sanchez, T., Chen, D. T., DeCamp, S. J., Heymann, M. & Dogic, Z. Spontaneous motion in hierarchically assembled active matter. *Nature* **491**, 431–434 (2012).
- Schaller, V., Weber, C., Semmrich, C., Frey, E. & Bausch, A. R. Polar patterns of driven filaments. *Nature* **467**, 73–77 (2010).
- Doostmohammadi, A., Ignes-Mullol, J., Yeomans, J. M. & Sagues, F. Active nematics. *Nat. Commun.* **9**, 3246 (2018).
- Couzin, I. D. & Krause, J. Self-organization and collective behavior in vertebrates. *Adv. Stud. Behav.* **32**, 10–1016 (2003).
- Howse, J. R. et al. Self-motile colloidal particles: from directed propulsion to random walk. *Phys. Rev. Lett.* **99**, 048102 (2007).
- Chen, X. et al. Unraveling the physiochemical nature of colloidal motion waves among silver colloids. *Sci. Adv.* **8**, eabn9130 (2022).
- Palagi, S. & Fischer, P. Bioinspired microrobots. *Nat. Rev. Mater.* **3**, 113–124 (2018).
- Rubenstein, M., Ahler, C. & Nagpal, R. Kilobot: A low cost scalable robot system for collective behaviors. in *2012 IEEE International Conference on Robotics and Automation* 3293–3298 (2012).
- Parent, C. A. & Devreotes, P. N. A cell's sense of direction. *Science* **284**, 765–770 (1999).
- Singer, G., Araki, T. & Weijer, C. J. Oscillatory cAMP cell-cell signalling persists during multicellular Dictyostelium development. *Commun. Biol.* **2**, 139 (2019).
- Gorbonos, D. et al. Long-range acoustic interactions in insect swarms: an adaptive gravity model. *N. J. Phys.* **18**, 73042 (2016).
- Ramm, B. et al. A diffusio-phoretic mechanism for ATP-driven transport without motor proteins. *Nat. Phys.* **17**, 850–858 (2021).
- Altemose, A. et al. Chemically Controlled Spatiotemporal Oscillations of Colloidal Assemblies. *Angew. Chem. Int. Ed. Engl.* **56**, 7817–7821 (2017).
- Zhou, C. et al. Coordinating an Ensemble of Chemical Micromotors via Spontaneous Synchronization. *ACS Nano* **14**, 5360–5370 (2020).
- Katzschmann R. K., DelPreto J., MacCurdy R., Rus D. Exploration of underwater life with an acoustically controlled soft robotic fish. *Sci Robot* **3**, (2018).
- Li, S. et al. Particle robotics based on statistical mechanics of loosely coupled components. *Nature* **567**, 361–365 (2019).
- Waters, C. M. & Bassler, B. L. Quorum sensing: cell-to-cell communication in bacteria. *Annu. Rev. Cell Dev. Biol.* **21**, 319–346 (2005).
- Zampetaki, A. V., Liebchen, B., Ivlev, A. V. & Löwen, H. Collective self-optimization of communicating active particles. *Proc. Natl Acad. Sci. USA* **118**, e2111142118 (2021).
- Liu, Z. T. et al. Activity waves and freestanding vortices in populations of subcritical Quincke rollers. *Proc. Natl Acad. Sci. USA* **118**, e2104724118 (2021).
- Liebchen, B., Cates, M. E. & Marenduzzo, D. Pattern formation in chemically interacting active rotors with self-propulsion. *Soft Matter* **12**, 7259–7264 (2016).
- Saha, S., Golestanian, R. & Ramaswamy, S. Clusters, asters, and collective oscillations in chemotactic colloids. *Phys. Rev. E* **89**, 062316 (2014).
- Liebchen, B. & Lowen, H. Synthetic chemotaxis and collective behavior in active matter. *Acc. Chem. Res.* **51**, 2982–2990 (2018).
- Sesé-Sansa, E., Levis, D. & Pagonabarraga, I. Phase separation of self-propelled disks with ferromagnetic and nematic alignment. *Phys. Rev. E* **104**, 054611 (2021).
- Romanczuk, P., Erdmann, U., Engel, H. & Schimansky-Geier, L. Beyond the Keller-Segel model. *Eur. Phys. J. Spec. Top.* **157**, 61–77 (2008).
- Bäuerle, T., Fischer, A., Speck, T. & Bechinger, C. Self-organization of active particles by quorum sensing rules. *Nat. Commun.* **9**, 3232 (2018).
- Tyson, J. J. & Murray, J. D. Cyclic AMP waves during aggregation of Dictyostelium amoebae. *Development* **106**, 421–426 (1989).
- Parsek, M. R. & Greenberg, E. P. Acyl-homoserine lactone quorum sensing in gram-negative bacteria: a signaling mechanism involved in associations with higher organisms. *Proc. Natl Acad. Sci. USA* **97**, 8789–8793 (2000).
- Sager, B. & Kaiser, D. Intercellular C-signaling and the traveling waves of Myxococcus. *Genes Dev.* **8**, 2793–2804 (1994).
- Schmitt, O. H. A thermionic trigger. *J. Sci. Instrum.* **15**, 24 (1938).

33. Rappel, W.-J., Nicol, A., Sarkissian, A., Levine, H. & Loomis, W. F. Self-organized vortex state in two-dimensional Dictyostelium dynamics. *Phys. Rev. Lett.* **83**, 1247 (1999).
  34. Levine, H., Rappel, W. J. & Cohen, I. Self-organization in systems of self-propelled particles. *Phys. Rev. E* **63**, 017101 (2000).
  35. Levine, H., Aranson, I., Tsimring, L. & Truong, T. V. Positive genetic feedback governs cAMP spiral wave formation in Dictyostelium. *Proc. Natl Acad. Sci. USA* **93**, 6382–6386 (1996).
  36. Meyer, M., Schimansky-Geier, L. & Romanczuk, P. Active Brownian agents with concentration-dependent chemotactic sensitivity. *Phys. Rev. E* **89**, 022711 (2014).
  37. Brenner, M. P., Levitov, L. S. & Budrene, E. O. Physical mechanisms for chemotactic pattern formation by bacteria. *Biophys. J.* **74**, 1677–1693 (1998).
  38. Vicsek, T., Czirok, A. & Ben-Jacob, E. Cohen I, Shochet O. Novel type of phase transition in a system of self-driven particles. *Phys. Rev. Lett.* **75**, 1226–1229 (1995).
  39. Kessin, R. H. *Dictyostelium: Evolution, Cell Biology, and the Development of Multicellularity* (Cambridge University Press, 2001).
  40. Aranson, I. S. & Tsimring, L. S. Pattern formation of microtubules and motors: inelastic interaction of polar rods. *Phys. Rev. E* **71**, 050901 (2005).
  41. Song, L. et al. Dictyostelium discoideum chemotaxis: Threshold for directed motion. *Eur. J. Cell Biol.* **85**, 981–989 (2006).
  42. Toner, J. & Tu, Y. Long-range order in a two-dimensional dynamical XY model: how birds fly together. *Phys. Rev. Lett.* **75**, 4326–4329 (1995).
  43. Aranson, I. S., Levine, H. & Tsimring, L. Spiral competition in three-component excitable media. *Phys. Rev. Lett.* **76**, 1170–1173 (1996).
  44. Cates, M. E. & Tailleur, J. Motility-induced phase separation. *Annu Rev. Condens Ma* **P 6**, 219–244 (2015).
  45. Voorhees, P. W. The theory of Ostwald ripening. *J. Stat. Phys.* **38**, 231–252 (1985).
  46. Bray, A. J., Majumdar, S. N. & Schehr, G. Persistence and first-passage properties in nonequilibrium systems. *Adv. Phys.* **62**, 225–361 (2013).
  47. Avinery, R., Kornreich, M. & Beck, R. Universal and accessible entropy estimation using a compression algorithm. *Phys. Rev. Lett.* **123**, 178102 (2019).
  48. Martiniani, S., Chaikin, P. M. & Levine, D. Quantifying hidden order out of equilibrium. *Phys. Rev. X* **9**, 11031 (2019).
  49. Ziv, J. & Lempel, A. A universal algorithm for sequential data compression. *IEEE T Inf. Theory* **23**, 337–343 (1977).
  50. Dormann, D., Vasiev, B. & Weijer, C. J. Propagating waves control Dictyostelium discoideum morphogenesis. *Biophys. Chem.* **72**, 21–35 (1998).
  51. Thutupalli, S. & Herminghaus, S. Tuning active emulsion dynamics via surfactants and topology. *Eur. Phys. J. E* **36**, 1–10 (2013).
  52. Shen, J., Tang, T. & Wang, L.-L. *Spectral Methods: Algorithms, Analysis and Applications* (Springer, 2011).
  53. Guennebaud, G. et al. Eigen v3. <http://eigen.tuxfamily.org> (2010).
  54. Meakin, P. Diffusion-limited droplet coalescence. *Phys. A* **165**, 1–18 (1990).
- Horizon 2020 research and innovation programme (Marie Skłodowska-Curie Grant Agreement No. 754388). I.M. acknowledges support through LMUexcellent, funded by the Federal Ministry of Education and Research (BMBF) and the Free State of Bavaria under the Excellence Strategy of the German Federal and State Governments. Research of I.S.A. was supported by the U.S. Department of Energy, Office of Science, Basic Energy Sciences, Materials Science and Engineering Division, under Award No. DE-SC0020964. I.S.A. thanks the Alexander-von-Humboldt foundation for the support of his collaboration with the LMU Munich. E.F. acknowledges support from the German Research Foundation DFG through Collaborative Research Center SFB 1032, Project- ID No. 201269156. E.F. acknowledges support from Germany's Excellence Strategy, Excellence Cluster ORIGINS, EXC-2094-390783311.

### Author contributions

I.S.A. and E.F. designed the research, A.Z. and I.M. performed the computational studies and analyzed the numerical data. All authors participated in discussing and interpreting the theoretical results and in writing the manuscript.

### Funding

Open Access funding enabled and organized by Projekt DEAL.

### Competing interests

The authors declare no competing interests.

### Additional information

**Supplementary information** The online version contains supplementary material available at <https://doi.org/10.1038/s41467-022-34484-2>.

**Correspondence** and requests for materials should be addressed to Igor S. Aranson or Erwin Frey.

**Peer review information** *Nature Communications* thanks the anonymous reviewer(s) for their contribution to the peer review of this work.

**Reprints and permissions information** is available at <http://www.nature.com/reprints>

**Publisher's note** Springer Nature remains neutral with regard to jurisdictional claims in published maps and institutional affiliations.

**Open Access** This article is licensed under a Creative Commons Attribution 4.0 International License, which permits use, sharing, adaptation, distribution and reproduction in any medium or format, as long as you give appropriate credit to the original author(s) and the source, provide a link to the Creative Commons license, and indicate if changes were made. The images or other third party material in this article are included in the article's Creative Commons license, unless indicated otherwise in a credit line to the material. If material is not included in the article's Creative Commons license and your intended use is not permitted by statutory regulation or exceeds the permitted use, you will need to obtain permission directly from the copyright holder. To view a copy of this license, visit <http://creativecommons.org/licenses/by/4.0/>.

© The Author(s) 2022

### Acknowledgements

A.Z. thanks Timo Krüger for sharing his expertise on agent-based active matter simulations and acknowledges support by Graduate School of Quantitative Biosciences Munich (QBM). I.M. has received funding from the European Research Council (ERC) under the European Union's

Supplementary Information for

# Multi-scale organization in communicating active matter

Alexander Ziepke,<sup>1</sup> Ivan Maryshev,<sup>1</sup> Igor S. Aranson,<sup>2\*</sup> and Erwin Frey<sup>1,3\*</sup>

<sup>1</sup>Arnold Sommerfeld Center for Theoretical Physics and Center for NanoSciences,  
Ludwig-Maximilians-Universität München, Theresienstr. 37, 80333 Munich, Germany  
<sup>2</sup>Department of Biomedical Engineering, Pennsylvania State University, University Park,  
PA 16802, USA

<sup>3</sup>Max Planck School Matter to Life, Hofgartenstraße 8, 80539 Munich, Germany

\*Correspondence to: isa12@psu.edu, frey@lmu.de

# Supplementary Notes

## 1 Derivation of the hydrodynamic equations through a Boltzmann-like kinetic approach

In this section we show how the set of hydrodynamic equations,

$$\partial_t \rho(\mathbf{r}, t) = -v_0 \nabla \cdot \mathbf{p} + D_\rho \Delta \rho, \quad (1a)$$

$$\partial_t \mathbf{p}(\mathbf{r}, t) = \sigma (\rho - 1) \mathbf{p} - \delta |\mathbf{p}|^2 \mathbf{p} + D_p \Delta \mathbf{p} - \chi \mathbf{p} \cdot \nabla \mathbf{p} - Q(\rho) \nabla \rho + \rho \omega \nabla c, \quad (1b)$$

$$\partial_t c(\mathbf{r}, t) = D_c \Delta c - \alpha c + \rho \beta \Theta (c - c_{\text{th}}) (1 - s), \quad (1c)$$

$$\partial_t s(\mathbf{r}, t) = D_s \Delta s - \epsilon (s - c) - \bar{v} \mathbf{p} \cdot \nabla s, \quad (1d)$$

can be derived from a Boltzmann-like approach for the probability density  $P(\mathbf{r}, \varphi, t)$  of finding a particle at position  $\mathbf{r}$  with orientation  $\varphi$  at time  $t$ ; the particle's orientation is signified by the unit vector  $\mathbf{n} = (\cos \varphi, \sin \varphi)^T$ . The equation accounts for center-of-mass diffusion, particle self-propulsion, rotational diffusion, alignment with the signaling field, and interactions between particles:

$$\partial_t P(\mathbf{r}, \varphi, t) = D_\rho \partial_i \partial_i P - v_0 \partial_i (n_i P) + \partial_\varphi [D_R \partial_\varphi + \omega(c) \sin(\varphi - \varphi_c)] P + \text{interactions}. \quad (2)$$

The advection term together with the rotational diffusion describe the self-propelled motion of the particles combined with the angular noise as in the agent-based model. The fourth term corresponds to a probability flux directed towards orientations that are aligned with the local gradients of the signaling field  $c$  with sensitivity parameter  $\omega(c)$  and  $\varphi_c \equiv \tan^{-1}(\partial_y c / \partial_x c) = \text{angle}(\nabla c)$ . The interaction contributions will be discussed further below.

We follow the standard approach for deriving hydrodynamic equations from a Boltzmann-type of equation by expanding the probability density function in Fourier modes for the spatial orientation of the director  $\mathbf{n}$  in two-dimensional space<sup>1,2</sup>,

$$P(\mathbf{r}, \varphi) = \sum_k P_k(\mathbf{r}) e^{ik\varphi}, \quad (3)$$

whereby, for the sake of brevity, we suppress the time dependency here and in the following. The corresponding Fourier coefficients follow from the forward transform

$$P_k(\mathbf{r}) = \frac{1}{2\pi} \int_0^{2\pi} d\varphi P(\mathbf{r}, \varphi) e^{-ik\varphi}. \quad (4)$$

We define the particle density  $\rho$  and the density-weighted polar order  $\mathbf{p}$  by relating them to the harmonics via the Fourier expansion, Eq. (3):

$$\rho(\mathbf{r}) \equiv \int_0^{2\pi} d\varphi P(\mathbf{r}, \varphi) = 2\pi P_0, \quad (5)$$

$$\begin{aligned} \mathbf{p}(\mathbf{r}) &\equiv \int_0^{2\pi} d\varphi \mathbf{n}(\varphi) P(\mathbf{r}, \varphi), \\ &= \sum_k \frac{1}{2} \int_0^{2\pi} d\varphi \left( e^{i\varphi} + e^{-i\varphi}, i(e^{-i\varphi} + e^{i\varphi}) \right)^T P_k(\mathbf{r}) e^{ik\varphi}, \\ &= \pi (P_1 + P_{-1}, i(P_1 - P_{-1}))^T. \end{aligned} \quad (6)$$

To describe the intrinsic states of the communicating active matter, we introduce a probability density  $P^s(s)$  of particles in a given signaling state  $s$  and assume that the total probability density  $P_{\text{tot}}(\mathbf{r}, \varphi, s) = P^s(s) P(\mathbf{r}, \varphi)$  factorizes in a part for the signaling state and the distribution for the agent's positions and orientations. Thus, the density-weighted signaling state of the agents is given by

$$\bar{s} \equiv \int ds \int_0^{2\pi} d\varphi s P^s(s) P(\mathbf{r}, \varphi). \quad (7)$$

In the following, the different contributions to the Boltzmann equation, Eq. (2), are analyzed separately. First, in order to derive expressions for the diffusive contributions in the hydrodynamic equations we use the projection onto the  $m$ -th harmonic,

$$\overline{(\dots)}^m = \frac{1}{2\pi} \int_0^{2\pi} d\varphi e^{-im\varphi} (\dots), \quad (8)$$

which gives the  $m$ -th Fourier coefficient to the expansion above, Eq. (3). Applying the projection operator, Eq. (8), onto the corresponding term in Eq. (2) one obtains

$$\partial_t \rho = D_\rho \Delta \rho, \quad (9)$$

for the dynamics of the density. One would obtain the same dynamics for the center-of-mass diffusion in the polar order field, but contributions from interaction kernels, representing elasticity of the polarity field, can lead to similar terms, which is why we assume a different coefficient  $D_p$  for the polar field. Continuing with the advective term, (i.e.  $\sim v_0$ ), the projection onto the modes yields

$$\begin{aligned} \partial_t P_m(\mathbf{r}) &= \overline{-v_0 \partial_i (n_i P(\mathbf{r}, \varphi))}^m, \\ &= -\frac{v_0}{2\pi} \int_0^{2\pi} d\varphi \sum_k P_k(\mathbf{r}) e^{ik\varphi} \left[ \partial_x e^{-im\varphi} \frac{(e^{i\varphi} + e^{-i\varphi})}{2} + \partial_y e^{-im\varphi} \frac{(e^{i\varphi} - e^{-i\varphi})}{2i} \right], \\ &= -\frac{v_0}{2} \left[ \partial_x \sum_k P_k(\mathbf{r}) (\delta_{k,m-1} + \delta_{k,m+1}) + i\partial_y \sum_k P_k(\mathbf{r}) (\delta_{k,m+1} - \delta_{k,m-1}) \right]. \end{aligned} \quad (10)$$

With the definitions, Eqs. (5) and (6), we obtain for the field variables

$$\partial_t \rho(\mathbf{r}) = 2\pi \partial_t P_0(\mathbf{r}) = -v_0 \partial_i p_i(\mathbf{r}), \quad (11)$$

$$\partial_t p_x(\mathbf{r}) = \pi \partial_t (P_1(\mathbf{r}) + P_{-1}(\mathbf{r})) = -\frac{v_0}{2} \partial_x \rho(\mathbf{r}), \quad (12a)$$

$$\partial_t p_y(\mathbf{r}) = i\pi \partial_t (P_1(\mathbf{r}) - P_{-1}(\mathbf{r})) = -\frac{v_0}{2} \partial_y \rho(\mathbf{r}). \quad (12b)$$

Since a Boltzmann-approach is by design a low-density approximation, these results must be interpreted as such and require for an extension to assure well-behavedness at higher densities. Notably, this applies to the coupling of the polarity field to density gradients,  $\partial_t p_i \sim -\frac{1}{2} v_0 \partial_i \rho$ . At low densities, this term accounts for an effective pressure, increasing with increasing particle densities. At higher densities, other cooperative effects emerging

from anisotropic interactions can dominate the coupling of the polarity field to density gradients, counteracting the repulsion dominating at low densities. In addition, at a critical maximum density, which we set to  $\rho = 2$ , the effective pressure increases significantly due to the finite volumes of the agents. Therefore, steric interactions dominate the cooperative interactions for  $\rho \rightarrow 2$ . We account for these effects by extending the terms  $\sim -\partial_i \rho$  by a density-dependent prefactor  $Q(\rho)$  which is proportional to  $v_0$  and has the following form:

$$Q(\rho) = \frac{v_0}{2} \left[ \exp(-32\rho) + \exp(16(\rho - 2)) \right]. \quad (13)$$

The function  $Q(\rho)$  captures the repulsion at low densities which decays for intermediate densities due to cooperative effects. Moreover, it limits the maximum density to values  $\rho \approx 2$  taking into account the steric repulsion at dense packing of the agents. The presented results do not qualitatively depend on the particular choice of the function  $Q(\rho)$ . The scalar field corresponding to the agent's signaling activity, Eq. (7) is directly associated with the agents. Hence, in the same way as the particles it is advected with the polar flow and exhibits center-of-mass diffusion. From the definition, Eq. (7), we obtain

$$\begin{aligned} \partial_t \bar{s} &= -v_0 \int d\varphi ds s \partial_i n_i P, \\ &= -v_0 \int d\varphi ds s \left[ \partial_x \frac{e^{i\varphi} + e^{-i\varphi}}{2} + \partial_y \frac{e^{i\varphi} - e^{-i\varphi}}{2i} \right] \sum_k P^k P^s, \\ &= -2\pi v_0 \int ds s \left[ \frac{1}{2} \partial_x (P_{-1}^\varphi + P_1^\varphi) + \frac{1}{2i} \partial_y (P_{-1}^\varphi - P_1^\varphi) \right] P^s, \end{aligned}$$

and with the definition of the polarity field, Eq. (6),

$$\partial_t \bar{s} = -v_0 \partial_i \left( \frac{\bar{s} p_i}{\rho} \right). \quad (14)$$

Thus, the complete diffusive and advective contributions to the dynamics of the density weighted signaling state  $\bar{s} = \rho s$  are given by

$$\partial_t \bar{s} = D_\rho \Delta \bar{s} - v_0 \partial_i \left( \frac{\bar{s} p_i}{\rho} \right). \quad (15)$$

Correspondingly to the agent-based model, we re-express the state field  $\bar{s}$  in terms of the 'state concentration', i.e., the local state normalized by the particle density,  $s$  by replacing  $s = \bar{s}/\rho$  in Eq. (15); one obtains

$$\partial_t s = D_\rho \Delta s - \frac{v_0 p_i}{\rho} \cdot (\partial_i s), \quad (16)$$

where we neglected cross-gradient contributions in the density  $\rho$  and the field  $s$ .

Next, we turn to the contribution of the angular noise to the dynamics of the polar field. Fourier-expanding the corresponding term  $\sim D_R$  in Eq. (2) and projecting it onto the  $j^{\text{th}}$  harmonic according to Eq. (8), yields the equation

$$\partial_t P_j(\mathbf{r}) = -D_R j^2 P_j(\mathbf{r}) \quad (17)$$

and, thus, with the definition of the polar field, Eq. (6),

$$\partial_t \mathbf{p}(\mathbf{r}) = -2D_R \mathbf{p}(\mathbf{r}). \quad (18)$$

Finally, regarding the alignment of the agents' orientation vectors with gradients of the signaling field  $c$ , we want to briefly highlight the origin of the corresponding terms,  $\sim \omega$ , in the Boltzmann equation (2) starting from the proposed underlying Langevin dynamics

$$\begin{aligned} \frac{\partial \mathbf{r}}{\partial t} &= v_0 \mathbf{n}(\varphi), \\ \frac{\partial \varphi}{\partial t} &= \xi(t) + \omega(c) \sin(\varphi - \varphi_c), \end{aligned} \quad (19)$$

with the particle position vector  $\mathbf{r}$  and the angle of the chemical gradient  $\varphi_c = \text{angle}(\nabla c)$ . The chemotaxis contributes to the Boltzmann equation, Eq. (2), directly as the angular drift term

$$\partial_t P \sim -\partial_\varphi [\omega(c) \sin(\varphi - \varphi_c)] P. \quad (20)$$

Expanding the probability density in the Fourier harmonics as in Eq. (3), one obtains

$$\partial_t P_k = -\frac{\omega(c)}{2\pi} \int_0^{2\pi} d\varphi e^{-ik\varphi} \partial_\varphi \left[ \sin(\varphi - \varphi_c) \sum_{k'} P_{k'} e^{ik'\varphi} \right], \quad (21)$$

and after integration by parts

$$\begin{aligned} \partial_t P_k &= -\frac{ik\omega(c)}{2\pi} \sum_{k'} \int_0^{2\pi} d\varphi [\cos(\varphi_c) \sin(\varphi) - \sin(\varphi_c) \cos(\varphi)] P_{k'} e^{i(k'-k)\varphi}, \\ &= -\frac{ik\omega(c)}{4\pi} \sum_{k'} [\cos(\varphi_c) (i\delta_{k,k'-1} - i\delta_{k,k'+1}) - \sin(\varphi_c) (\delta_{k,k'-1} + \delta_{k,k'+1})] P_{k'}. \end{aligned} \quad (22)$$

Using the definitions, Eqs. (5),(6), and neglecting contributions of the second harmonics, the response of the dynamics of  $\mathbf{p}$  to the signaling stimulus is given by

$$\partial_t p_i = \omega \rho \partial_i c, \quad (23)$$

where we chose a linear dependence of the alignment strength on the signaling amplitude  $c$ , namely  $\omega(c) = 4\pi \omega c$ . The contributions arising from particles' interactions can be motivated as done in Refs.<sup>3-5</sup>. As such, we include for completeness an elasticity like contribution

$$\partial_t \mathbf{p} \sim D_p \Delta \mathbf{p}, \quad (24)$$

and a self-propulsion

$$\partial_t \mathbf{p} \sim \chi \mathbf{p} \cdot \nabla \mathbf{p}, \quad (25)$$

in the model. Both terms may arise from anisotropic interactions, e.g., for elongated particles. They are not included in the agent-based model and we set the corresponding parameters

$D_p$  and  $\chi$  to small values as the effects are not crucial for the reported behavior of signaling active matter. Altogether we obtain the set of hydrodynamic equations

$$\partial_t \rho(\mathbf{r}, t) = -v_0 \nabla \cdot \mathbf{p} + D_\rho \Delta \rho, \quad (26a)$$

$$\partial_t \mathbf{p}(\mathbf{r}, t) = \sigma (\rho - 1) \mathbf{p} - \delta |\mathbf{p}|^2 \mathbf{p} + D_p \Delta \mathbf{p} - \chi \mathbf{p} \cdot \nabla \mathbf{p} - Q(\rho) \nabla \rho + \rho \omega \nabla c, \quad (26b)$$

$$\partial_t c(\mathbf{r}, t) = D_c \Delta c - \alpha c + \rho \beta \Theta(c - c_{\text{th}}) (1 - s), \quad (26c)$$

$$\partial_t s(\mathbf{r}, t) = D_s \Delta s - \epsilon (s - c) - \bar{v} \mathbf{p} \cdot \nabla s, \quad (26d)$$

complementing the derived contributions from the Boltzmann equation, Eq. (2), with the interaction terms, Eqs. (24), (25), and the continuous versions of the equations for the signaling machinery, Eqs. (3), (5) in the main text.

## 2 Reduced model without decision making

To highlight the role of the individual decision making for the multi-scale aggregation process, for comparison we also investigate the behavior of a system lacking such a mechanism. In particular, we modify the source dynamics given in main text Eq. (3), such that it becomes independent of the agents' internal state,

$$\partial_t c(\mathbf{r}, t) = D_c \Delta c - \alpha c + \beta \sum_{i=1}^N f(\mathbf{r}, t). \quad (27)$$

The polar agents with dynamics given by main text Eqs. (1), (2), and supplementary information Eq. (27), are assumed to contribute as persistent sources of the signaling field. Similar to what has been reported in reference<sup>6</sup>, we observe aster-like stationary cluster formation with interface controlled ripening, see Supplementary Fig. 4a. Moreover, the interplay between self-propulsion and attraction towards a local aggregation center can give rise to short-lived ring-like structures and vortices which eventually tend to dissolve into a few aster-like aggregates as depicted in Supplementary Fig. 4b. Since in the modified model there is only local interactions mediated by the comparably slow diffusion of the signaling field, it does not exhibit a collective long-range organization of aggregation centers. In contrast to a system with active decision making, here the established smaller aggregates collide and merge upon random encounters.

### 3 Model parameters

The supplementary tables 1-3 provide an overview of the system parameters used in the numerical simulations shown in the main text as well as in the supplementary figures and movies. We measure densities in units of the critical density for the isotropic-polar transition. Time is given in units of the signal decay rate  $[\alpha]$  and lengths are given in units of the resulting diffusion length  $\sqrt{D_c/[\alpha]}$ .

## Supplementary Tables

Parameter	Description	Value (continuum model)	Value (agent-based)
$\alpha$	signal decay rate	10	0.9
$\beta$	signal production rate	40	2
$a$	threshold factor	0.9	0.9
$b$	constant threshold	0.05	0.05
$\epsilon$	refractory rate	4	0.3
$D_c$	signal diffusion	1	0.9

Supplementary Table 1: Parameters of the signaling system, Eqs. (1c), (1d), in the excitable regime used for the hydrodynamic- and the agent-based model, respectively.

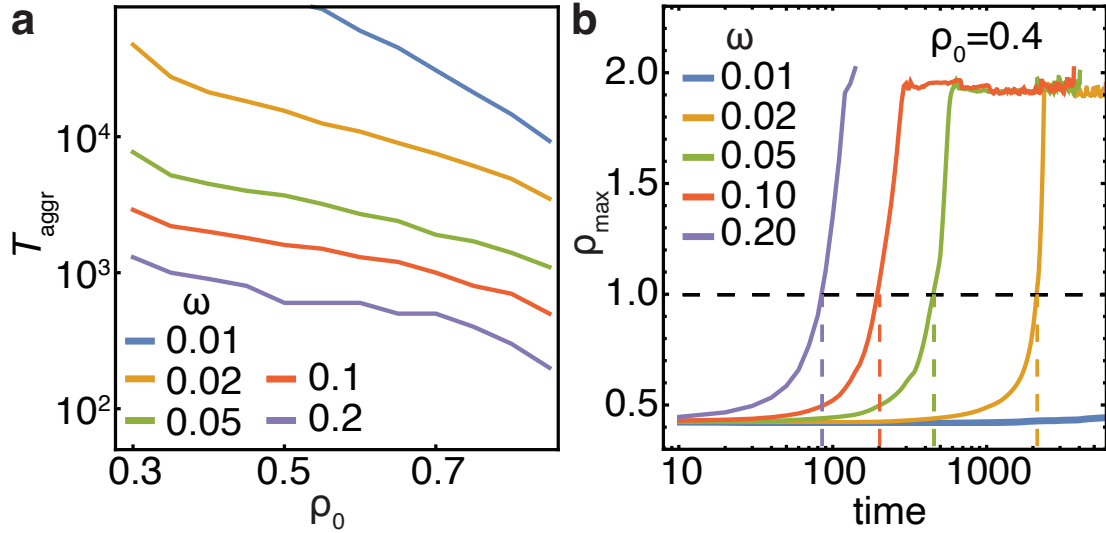
Parameter	Description	Value
$v_0$	propulsion speed	0.2
$D_R$	rotational diffusion	0.05
$r_c$	interaction radius	2
$r_p$	particle radius	0.25
$\Gamma$	polar alignment factor	0.1

Supplementary Table 2: Parameters of the agent-based model as detailed in Methods. The chemical susceptibility parameter in main text Fig. 1 is set to  $\omega \in \{0.1, 0.4, 0.004, 0.2, 0.004\}$  for panels e-i, respectively.

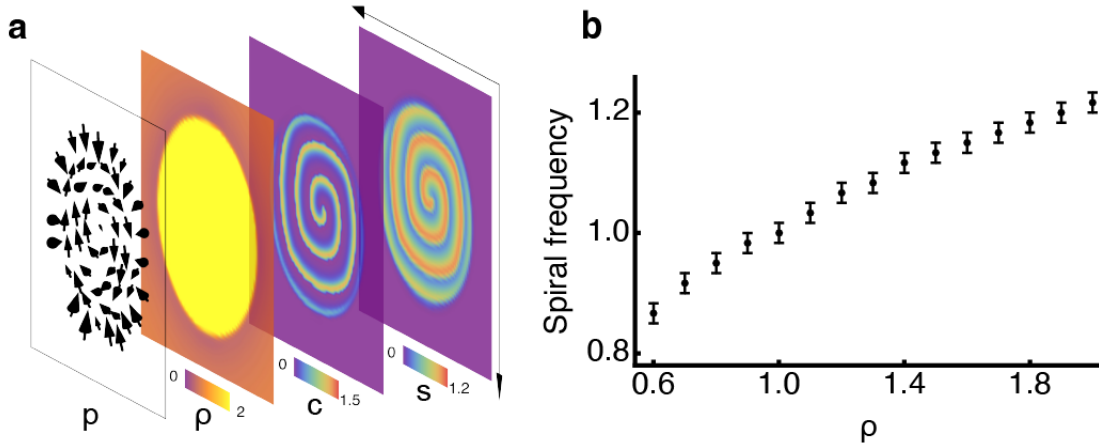
		Value				
Parameter	Description	Default	Fig. 1j	Fig. 1k	Fig. 1 l,n	Fig. 1 m
$v_0$	motility	0.5	0.1	0.5	0.2	0.1
$\sigma$	polar persistence parameter	0.01	0.1	0.2	0.5	0.05
$\omega$	signal susceptibility	0.1	0.8	0.3	0.8	0.4
$D_\rho$	translational diffusion	0.05				
$D_p$	elasticity parameter	0.1				
$\chi$	convective derivative coefficient	0.1				
$\delta$	magnitude of bulk order	1.0				
$\rho_0$	average density	0.6				

Supplementary Table 3: Parameters of the hydrodynamic continuum model, described in Methods. Figure numbers correspond to main text figures.

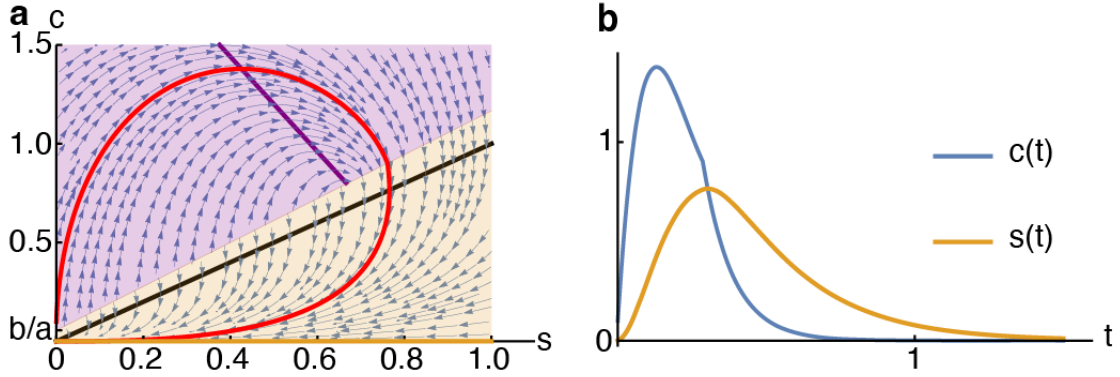
## Supplementary Figures



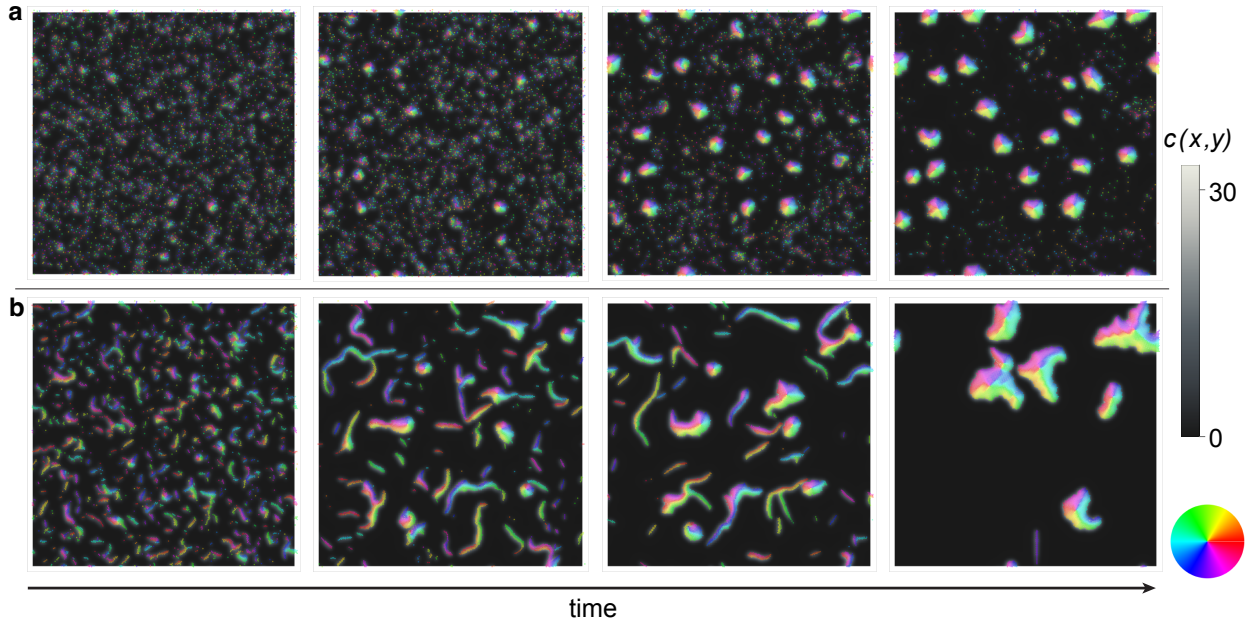
Supplementary Figure 1: Signaling-enhanced aggregation capabilities. a, Aggregation times  $T_{\text{aggr}}$  of the hydrodynamic system, main text Eqs. (6)-(9), reaching the polar-order transition at  $\rho = 1$  from a homogeneous initial density  $\rho_0$ . We observe faster aggregation for higher initial densities as well as larger signaling susceptibilities  $\omega$ . b, Corresponding temporal evolution of the system's maximum density  $\rho_{\text{max}}$  evolving from a homogeneous initial density  $\rho_0 = 0.4$  for different values of  $\omega$ . We determine the aggregation times  $T_{\text{aggr}}$  (dashed colored lines) as the first times at which the critical density (dashed black line) is reached,  $\rho_{\text{max}} = \rho_c = 1$ . Other parameters as given in SI section 3.



Supplementary Figure 2: Spiral waves and vortex solution in the hydrodynamic model. a, Vortex solution with persistent spiral wave activity in the hydrodynamic model, see Methods. The composite image containing layers representing the orientation vector field  $\mathbf{p}(\mathbf{r})$  (arrows), the local density profile  $\rho(\mathbf{r})$ , concentration of signaling molecules  $c(\mathbf{r})$ , and field of state  $s(\mathbf{r})$ . b, Dependence of spiral frequency on spatially homogeneous density values  $\rho$ . Error bars indicate error ranges arising from the numerical measurement of spiral frequencies. Parameters as stated in SI section 3.



Supplementary Figure 3: Excitable dynamics of the well-mixed signaling system. The agents serve both as a source of chemical signals and can adapt their internal state to the chemical environment. In this process, the release of the chemicals by the agents depends on the internal state of the agents and the state of the environment. The combination of these factors leads to a ‘sense-and-response’ system that exhibits excitable dynamics. a, Phase-space flow of the excitable system, main text Eqs. (3), (5). The black line indicates the nullcline  $c = s$  of the agents’ state kinetics, main text Eq. (5). Due to the discontinuous switch in the agents’ signal relaying capability, there are two nullclines (violet and orange) originating from the signaling kinetics, main text Eq. (3), with  $c = \beta/\alpha(1 - s)$  and  $c = 0$ , respectively. These nullclines are valid in the correspondingly colored areas  $c \geq (s + b)/a$ . The red trajectory highlights an excursion in phase space upon initial excitation. b, Dynamics of the chemical concentration  $c$  and the signaling state  $s$  corresponding to the red trajectory in a. Parameters as stated in SI section 3. Time is measured in the units of the decay rate  $[\alpha]$ .



Supplementary Figure 4: Time evolution of a reduced model, lacking the internal decision making machinery of the self-propelling agents, main text Eqs. (1), (2), and SI Eq. (27). The two parameter regimes shown in panels a and b illustrate localized cluster formation as a generic form of aggregation in the model. The clusters exhibit an interface-controlled coarsening behavior. a, Formation of localized clusters for small polar alignment  $\Gamma = 0.01$ . b, Cluster formation with intermediate transient solutions for stronger polar alignment,  $\Gamma = 0.1$ . Agent colors indicate the polar orientation and background colors represents concentrations of the communication field  $c(\mathbf{r}, t)$ , see Eq. (27). Parameters as in table 2 with  $r_p = 0.5$ ,  $\beta = 0.9$ , and  $\omega = 0.05$ .

## Supplementary References

1. Aranson, I. S. & Tsimring, L. S. Pattern formation of microtubules and motors: Inelastic interaction of polar rods. Phys. Rev. E **71**, 050901 (2005).
2. Bertin, E., Droz, M. & Grégoire, G. Boltzmann and hydrodynamic description for self-propelled particles. Phys. Rev. E **74**, 022101 (2006).
3. Aranson, I. S. & Tsimring, L. S. Patterns and collective behavior in granular media: Theoretical concepts. Rev. Mod. Phys. **78**, 641 (2006).
4. Peshkov, A., Aranson, I. S., Bertin, E., Chaté, H. & Ginelli, F. Nonlinear field equations for aligning self-propelled rods. Phys. Rev. Lett. **109**, 268701 (2012).
5. Maryshev, I., Marenduzzo, D., Goryachev, A. B. & Morozov, A. Kinetic theory of pattern formation in mixtures of microtubules and molecular motors. Phys. Rev. E **97**, 22412 (2018).
6. Romanczuk, P., Erdmann, U., Engel, H. & Schimansky-Geier, L. Beyond the Keller-Segel model. Eur. Phys. J. Spec. Top. **157**, 61–77 (2008).

## Description of Supplementary Movies<sup>1</sup>

To view the animations, click on <https://www.nature.com/articles/s41467-022-34484-2> and locate the text *Supplementary Movie 1 to Supplementary Movie 9* etc near the bottom of the page.

Supplementary Movie 1: Aggregation process in agent-based and hydrodynamic model. Visual comparison of the aggregation process from a homogeneous disordered state in the agent-based model (left) and the hydrodynamic model (right). We observe a very similar behavior with an initial formation of smaller droplets that subsequently organize into streams. Particles collectively propagate in active droplets towards emerging vortices as organization centres with internal spiral wave activity. Parameters for the agent-based simulation are  $N=8,000$ ,  $\omega=0.2$ . Parameters of the hydrodynamic model are  $D_c=2$ ,  $\epsilon=0.8$ ,  $\alpha=2$ ,  $\beta=8$ ,  $\sigma=0.02$  and remaining values as given in Supplementary Information section 3. Scale bars indicate a length of 10 units.

Supplementary Movie 2: Droplets as predominant collective dynamic states. Temporal dynamics of the density  $\rho$  (left) and the signaling field  $c$  (right) together with the local orientation  $p$  indicated by arrows. Results of numerical simulations of the hydrodynamic model accompanying Fig. 2.

Supplementary Movie 3: Vortices as predominant collective dynamic states. Temporal dynamics of the density  $\rho$  (left) and the signaling field  $c$  (right) together with the local orientation  $p$  indicated by arrows. Results of numerical simulations of the hydrodynamic model accompanying Fig. 2.

Supplementary Movie 4: Rings as predominant collective dynamic states. Temporal dynamics of the density  $\rho$  (left) and the signaling field  $c$  (right) together with the local orientation  $p$  indicated by arrows. Results of numerical simulations of the hydrodynamic model accompanying Fig. 2.

Supplementary Movie 5: Silent bands as predominant collective dynamic states. Temporal dynamics of the density  $\rho$  (left) and the signaling field  $c$  (right) together with the local orientation  $p$  indicated by arrows. Results of numerical simulations of the hydrodynamic model accompanying Fig. 2.

Supplementary Movie 6: Streams as predominant collective dynamic states. Temporal dynamics of the density  $\rho$  (left) and the signaling field  $c$  (right) together with the local orientation  $p$  indicated by arrows. Results of numerical simulations of the hydrodynamic model accompanying Fig. 2.

Supplementary Movie 7: Polar bands with signaling activity as predominant collective dynamic states. Temporal dynamics of the density  $\rho$  (left) and the signaling field  $c$  (right) together with the local orientation  $p$  indicated by arrows. Results of numerical simulations of the hydrodynamic model accompanying Fig. 2.

Supplementary Movie 8: Hierarchical aggregation and information processing. Time evolution of the density and signaling fields and corresponding information measures accompanying the data shown in Fig. 3.

Supplementary Movie 9: Ring annihilation due to interaction with a vortex. A stable vortex interacts with a meta-stable ring. Due course of time, the ring is destabilized by the interaction with the vortex and mass is transferred to the latter in a stream-like fashion. Parameters of the hydrodynamic simulation as detailed in Supplementary Methods section 3, with  $\sigma=0.05$

---

<sup>1</sup> Source: modified from [https://static-content.springer.com/esm/art%3A10.1038%2Fs41467-022-34484-2/MediaObjects/41467\\_2022\\_34484\\_MOESM2\\_ESM.pdf](https://static-content.springer.com/esm/art%3A10.1038%2Fs41467-022-34484-2/MediaObjects/41467_2022_34484_MOESM2_ESM.pdf)

## The physical intelligence of ant and robot collectives

*Date:* December 21, 2022

*Source:* Harvard John A. Paulson School of Engineering and Applied Sciences

*Summary:* Researchers took inspiration from ants to design a team of relatively simple robots that can work collectively to perform complex tasks using only a few basic parameters.

### FULL STORY

---

Individual ants are relatively simple creatures and yet a colony of ants can perform really complex tasks, such as intricate construction, foraging and defense.

Recently, Harvard researchers took inspiration from ants to design a team of relatively simple robots that can work collectively to perform complex tasks using only a few basic parameters.

The research was published in *ELife*.

"This project continued along an abiding interest in understanding the collective dynamics of social insects such as termites and bees, especially how these insects can manipulate the environment to create complex functional architectures," said L Mahadevan, the Lola England de Valpine Professor of Applied Mathematics, of Organismic and Evolutionary Biology, and Physics, and senior author of paper.

The research team began by studying how black carpenter ants work together to excavate out of and escape from a soft corral.

"At first, the ants inside the corral moved around randomly, communicating via their antennae before they started working together to escape the corral," said S Ganga Prasath, a postdoctoral fellow at the Harvard John A. Paulson School of Engineering and Applied Sciences and one of the lead authors of the paper.

Ants primarily rely on their antennae to interact with the environment and other ants, a process termed antennation. The researchers observed that the ants would spontaneously congregate around areas where they interacted more often. Once a few

ants started tunneling into the corral, others quickly joined in. Over time, excavation at one such location proceeded faster than at others and the ants eventually tunneled out of the corral.

From these observations, Mahadevan and his team identified two relevant parameters to understand the excavation task of the ants; the strength of collective cooperation, and the rate of excavation. Numerical simulations of mathematical models that encode these parameters showed that the ants can successfully excavate only when they cooperate with each other sufficiently strongly while simultaneously excavating efficiently.

Driven by this understanding and building upon the models, the researchers built robotic ants, nicknamed RAnts, to see if they could work together to escape a similar corral. Instead of chemical pheromones, the RAnts used "photormones," fields of light that are left behind by the roving RAnts that mimic pheromone fields or antennation.

The RAnts were programmed only via simple local rules: to follow the gradient of the photoromone field, avoid other robots where photoromone density was high and pick up obstacles where photoromone density was high and drop them where photoromone was low. These three rules enabled the RAnts to quickly escape their confinement, and just as importantly, also allowed the researchers to explore regions of behavior that were hard to detect with real ants.

"We showed how the cooperative completion of tasks can arise from simple rules and similar such behavioral rules can be applied to solve other complex problems such as construction, search and rescue and defense." said Prasath.

This approach is highly flexible and robust to errors in sensing and control. It could be scaled up and applied to teams of dozens or hundreds of robots using a range of different types of communication fields. It's also more resilient than other approaches to collaborative problem solving -- even if a few individual robotic units fail, the rest of the team can complete the task.

"Our work, combining lab experiments, theory and robotic mimicry, highlights the role of a malleable environment as a communication channel, whereby self-reinforcing signals lead to the emergence of cooperation and thereby the solution of complex problems. Even without global representation, planning or optimization, the interplay between simple local rules at the individual level and the embodied physics of the collective leads to intelligent behavior and is thus likely to be relevant more broadly," said Mahadevan.

The paper's other lead authors were Souvik Mandal and Fabio Giardina, and the paper was co-authored by Jordan Kennedy, and Venkatesh N Murthy, Raymond Leo Erikson Life Sciences Professor of Molecular and Cellular Biology in the Department of Molecular and Cellular Biology.

The research was supported in part by the National Science Foundation under grants PHY1606895, EFRI 18-30901 and 1764269, the Swiss National Science Foundation,

under grant P400P2- 191115, the Ford Foundation, the Kavli Institute for Bionano Science and Technology, the Simons Foundation and the Henri Seydoux Fund.

Video: <https://youtu.be/a6Yg8C4O0Ps>

---

### Story Source:

Materials provided by **Harvard John A. Paulson School of Engineering and Applied Sciences**. Original written by Leah Burrows. *Note: Content may be edited for style and length.*

---

### Journal Reference:

1. S Ganga Prasath, Souvik Mandal, Fabio Giardina, Jordan Kennedy, Venkatesh N Murthy, L Mahadevan. **Dynamics of cooperative excavation in ant and robot collectives**. *eLife*, 2022; 11 DOI: 10.7554/eLife.79638
- 

### Cite This Page:

MLA	APA	Chicago
-----	-----	---------

---

Harvard John A. Paulson School of Engineering and Applied Sciences. "The physical intelligence of ant and robot collectives." ScienceDaily. ScienceDaily, 21 December 2022. <[www.sciencedaily.com/releases/2022/12/221221135358.htm](http://www.sciencedaily.com/releases/2022/12/221221135358.htm)>.

# 1 Dynamics of cooperative excavation 2 in ant and robot collectives

3 S Ganga Prasath<sup>1†</sup>, Souvik Mandal<sup>2,3†</sup>, Fabio Giardina<sup>1†</sup>, Jordan Kennedy<sup>1</sup>,  
4 Venkatesh N Murthy<sup>2,3</sup>, L Mahadevan<sup>1,3,4,5</sup>

\*For correspondence:

lmahadev@g.harvard.edu (LM)

†These authors contributed  
equally to this work

5 <sup>1</sup>School of Engineering and Applied Sciences, Harvard University, Cambridge, United  
6 States; <sup>2</sup>Department of Molecular and Cellular Biology, Harvard University, Cambridge,  
7 United States; <sup>3</sup>Center for Brain Science, Harvard University, Cambridge, United States;  
8 <sup>4</sup>Department of Physics, Harvard University, Cambridge, United States; <sup>5</sup>Department of  
9 Organismic and Evolutionary Biology, Harvard University, Cambridge, United States

10

11 **Abstract** The solution of complex problems by the collective action of simple agents in both  
12 biologically evolved and synthetically engineered systems involves cooperative action.  
13 Understanding the resulting emergent solutions requires integrating across the organismal  
14 behaviors of many individuals. Here we investigate an ecologically relevant collective task in black  
15 carpenter ants *Camponotus pennsylvanicus*: excavation of a soft, erodible confining corral.  
16 Individual ants show a transition from individual exploratory excavation at random locations to  
17 spatially localized collective exploitative excavation and eventual excavate out from the corral. An  
18 agent minimal continuum theory that coarse-grains over individual actions and considers their  
19 integrated influence on the environment leads to the emergence of an effective phase space of  
20 behaviors in terms of excavation strength and cooperation intensity. To test the theory over the  
21 range of both observed and predicted behaviors, we used custom-built robots (RAnts) that  
22 respond to stimuli to characterize the phase space of emergence (and failure) of cooperative  
23 excavation. By tuning the amount of cooperation between RAnts, we found that we could vary  
24 the efficiency of excavation and synthetically generate the other macroscopic phases predicted  
25 by our theory. Overall, our approach shows how the cooperative completion of tasks can arise  
26 from simple rules that involve the interaction of agents with a dynamically changing environment  
27 that serves as both an enabler and a modulator of behavior.

28

## 29 Introduction

30 Collective behavior is seen in organisms across many decades in length-scale, from the microscopic  
31 to the macroscopic (Nowak, 2006; Camazine et al., 2020; Gordon, 1999; Seeley, 2009; Couzin et al.,  
32 2003). These behaviours are often functional and serve as solutions to problems associated with  
33 a range of tasks that cannot be solved efficiently at the individual level: from brood care to forag-  
34 ing for food, protection from enemies and predation of prey, building complex architectures etc.  
35 (Feinerman et al., 2018; Ocko and Mahadevan, 2014; Hölldobler et al., 2009; Peleg et al., 2018;  
36 Rasse and Deneubourg, 2001). Since collective behavior involves multiple individuals, it necessarily  
37 involves some form of communication and/or cooperation that takes different forms across scales  
38 - from quorum sensing in unicellular bacterium and slime molds, to the waggle dance in bees, and  
39 various forms of physical signal propagation in animal societies and human organizations (Rasse  
40 and Deneubourg, 2001; Alcock, 2001; Pennisi, 2009; Nowak, 2006; Elster et al., 1998; Couzin et al.,  
41 2003).

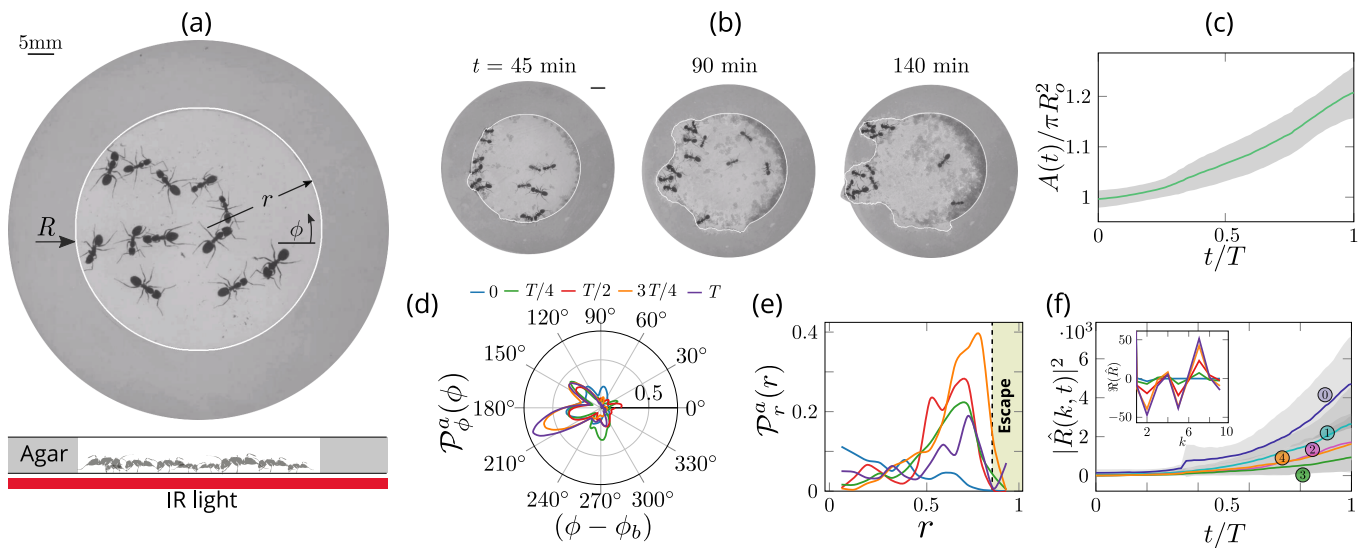


**Figure 1. Collective dynamics of ant excavation** (a) Colony members of the black carpenter ant *Camponotus pennsylvanicus* are confined to a porous boundary made out of Agarose. The boundary is represented by its radius  $R(\phi, t)$  ( $\phi$  - polar angle,  $t$  - time). Bottom part shows the side-view schematic of the experimental set-up with the boundary made of agarose and background IR light source used to image the ants in the dark. (b) Temporal progression of excavation experiments as 12 ants cooperatively tunnel through the agarose confinement. The white line is the tracked location of the inner wall which grows in size as the excavation progresses. (c) Confinement area  $A(t)$  as a function of time (scaled by time to excavate out of the corral  $T$ ), normalized by initial circular confinement with radius  $R_0$ . (d) Evolution of the orientation distribution of the ant density,  $\mathcal{P}_\phi^a(\phi, t)$  obtained by averaging along the radial direction. Ants start from an initially isotropic state and localize at an angle  $\phi_b$  along the boundary.  $T$  here is the excavation time. (e) Dynamics of the radial distribution of ant density  $\mathcal{P}_r^a(r, t)$  as a function of radial distance,  $r$  obtained by averaging a sector of  $\pi/6$  around the excavation site. We see that the ant density front propagates through the corral. The density is plotted for the same times as in (d). (f) Evolution of the power spectrum  $|\hat{R}(k, t)|^2$  of first five Fourier modes capturing the number of tunnels formed during excavation  $R(\phi, t) = \sum_k \hat{R}(k, t)e^{ik\phi}$ . Inset shows the real part of the Fourier coefficient,  $\Re(\hat{R})$  at different time instants indicating that many modes are present in the boundary shape.

42 The importance of environmental signals is particularly clearly seen in examples of collective  
 43 task execution in social insects that have a long history of documented cooperative behavior (*Hölldobler et al., 1990; Gordon, 1999; Perna and Theraulaz, 2017; Mikheyev and Tschinkel, 2004*).  
 44 Super-organisms made of individuals that respond to local stimuli with stereotypical actions that  
 45 leave their "mark" on the environment, creating a spatio-temporal memory, and is commonly  
 46 known as stigmergy (*Hölldobler et al., 2009*). While stigmergy is usually associated with scalar  
 47 pheromone fields, a broader definition might include the use of signaling via chemical, mechanical  
 48 and hydrodynamic means (*Buhl et al., 2005; Mikheyev and Tschinkel, 2004*), as has been quanti-  
 49 fied in recent studies of bees (*Ocko and Mahadevan, 2014; Peleg et al., 2018*). To understand how  
 50 collective task execution arises, we need to understand how individuals switch from local uncoor-  
 51 dinated behavior to collective cooperation that translates to successful task execution in different  
 52 social systems. From a biological perspective, this naturally involves understanding the neural cir-  
 53 cuits, physiology and ethology of an individual. A complementary perspective at the level of the  
 54 collective is that of characterizing a "crude view of the whole," which entails the quest for a small  
 55 set of rules that are sufficient for task completion and the range of possible solutions that arise  
 56 from these rules that might be tested experimentally. And finally, given the ability to engineer min-  
 57 imally responsive biomimetic agents such as robots (*Rahwan et al., 2019*), a question that suggests  
 58 itself is that of the synthesis of effective behaviors using these agents. Therefore, we also explore  
 59 regions of phase space that are hard to explore with social insects, to learn about the robustness  
 60 of these behaviors using imperfect agents in uncertain and noisy physical environments, before  
 61 looking for them *in-vivo*.  
 62

63 Here we use an ecologically relevant task in carpenter ants *Camponotus Pennsylvanicus*: exca-  
 64 vation and tunneling, to quantify the dynamics of successful task execution by tracking individual  
 65 ants, use this to create a quantitative framework that takes the form of mathematical models for

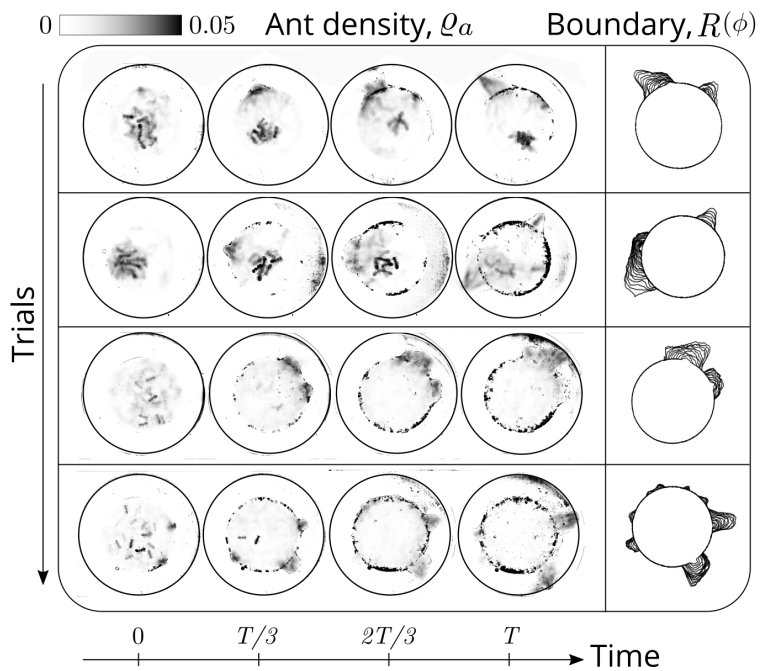


**Figure 2.** Evolution of the ant density field,  $\rho_a(\mathbf{x}, t)$  (in units of  $\#/mm^2$ ) as the tunneling progresses for experiments with 12 major ants. The density field is obtained by averaging the ant locations over 250 secs during the tunneling process. In the second columns is the evolution of the boundary shape,  $R(\phi)$  as a function of time where we see multiple excavation sites being explored before one of them succeeds. The darker spots in the image are the debris that the ants deposit as they excavate the boundary.

66 the behavior of how agents communicate and cooperate, and finally synthesize the behavior using  
 67 robots that can sense and act. Our work complements and builds on earlier studies on excavation  
 68 (*Buhl et al., 2005; Tschinkel, 2004; Deneubourg and Franks, 1995; Deneubourg et al., 2002*) in  
 69 social insects that looked at the effects of population size and role of cooperation on efficiency of  
 70 digging and developed 1-dimensional models to understanding the effective excavation process.  
 71 We go beyond these studies by (i) quantifying the collective behavior of ants by tracking them in  
 72 space-time while following the dynamics of how they interact with each other and the simultaneous  
 73 excavation a substrate that confines them, and (ii) use our observations to develop a theoretical  
 74 framework that couples the change in ant density, substrate density and the rate of antennation in  
 75 space and time to capture the collective execution of the task. We also identify the non-dimensional  
 76 parameters that define the range of behaviors of the agents and use this to map out the dynamics  
 77 of agents in different phases using an agent-based model. (iii) We then synthesize and recreate  
 78 this behavior using custom-built robots that can respond to each other and the environment to  
 79 show how they can perform this collective task. An important outcome of our study is a phase  
 80 diagram that shows the emergence of different collective behaviors associated with task comple-  
 81 tion as a function of just two dimensionless parameters that characterize the local rules underlying  
 82 individual behavior and the nature of communication between agents, e.g. ants and robots.

### 83 **Materials and methods**

#### 84 **Excavation in Carpenter ants**

85 We start with ants drawn from a mature colony of *C. Pennsylvanicus* that consist of a queen, the  
 86 sole egg layer, and the workers from three morphologically different castes - major, median and  
 87 minor (*Hansen and Klotz, 2005*). Though all ants perform different tasks like foraging, nest-keeping,  
 88 brood care to a varied degree, during excavation, major ants, equipped with their large mandibles,  
 89 generally take the lead role, while media and minor ants transport the debris outside their nest.  
 90 Ants communicate primarily through their antennae by using them to sense pheromones released

91 by other ants and by touching other ants to identify their caste. It is this inter-organismal informa-  
 92 tion exchange that enables the collective solution of complex tasks. Our experiments consist of a  
 93 dozen worker ants from the same colony that are anesthetized (using  $CO_2$ ) and then brought into a  
 94 confining corral made out of agarose flanked between two hard plastic sheets, without visible light  
 95 to mimic their natural environment in a nest; infrared light was used to monitor the experiment  
 96 using video (see **Figure 1(a)**). We used a ring-like confinement made of agarose gel, with a height  
 97 of 10 mm, an inner radius of 35 mm and outer radius of 55 mm, making the ring 20 mm thick. We  
 98 performed a total of 7 sets of experiments with 4 experiments with a collective of 12 majors ants  
 99 and 3 sets of experiments with a mixture of 4 major, 4 media and 4 minor ants. Once the ants  
 100 regain activity (due to the introduction of  $O_2$ ), they stay still for a while before moving. Observa-  
 101 tions show that they first exhibit wall-following followed by one of the ants initiating an exploratory  
 102 excavation at a random location along the corral (ref **Figure 2**). After an initial exploratory phase  
 103 the ants switch to an exploitative strategy in which they excavate a tunnel at a specific location and  
 104 eventually break through the corral (see the sequence in **Figure 1(b)**).

105 We can quantify this transition from rotationally isotropic exploration to localized excavation by  
 106 considering either the behavior of individual ants or their effective density  $\rho_a(r, \phi, t)$  as a function of  
 107 the polar coordinates  $(r, \phi)$  and time. We choose to use an effective coarse-grained density for two  
 108 reasons: it is a more natural variable in the limit of large populations that vary in space and time,  
 109 and is also amenable to building effective theories to which experiments can be compared. The  
 110 ant density is obtained by averaging the position of the ants over a time window larger than the  
 111 time taken for them to perform one cycle of excavation at the boundary to dropping debris in the  
 112 bulk (see sec. 1 for further details). Over time, the density becomes localized at a particular angle  
 113 and location along the corral where large-scale excavation eventually leads to excavation out of  
 114 the corral (see Video 3, **Figure 2** and SI **Figure 1** for the coarse-grained spatio-temporal evolution  
 115 of the ant density, obtained by this averaging procedure). Simultaneously, we see a signature of  
 116 collective excavation in an increase of the volume of excavated material, as shown in **Figure 1(c)**  
 117 (see also (**Toffin et al., 2009**)). Averaging the density over radial positions, in **Figure 1(d)** we show the  
 118 orientation distribution of the ant density  $\mathcal{P}_\phi^a(\phi, t) = \int \rho_a(r, \phi, t) dr$  is initially isotropic, and gradually  
 119 starts to localize at a particular (arbitrary) value of the angle as time increases.

120 Averaging the density over the localized region, in **Figure 1(e)** we show the radial distribution of  
 121 the ant density  $\mathcal{P}_r^a(r, t) = \int \rho_a(r, \phi, t) S(\phi) d\phi$  (where  $S(\phi)$  is a kernel around the excavation site) that  
 122 is initially uniform, and gradually propagates inside the boundary of the corral as time increases.  
 123 Consistent with localization and concomitant excavation (**Figure 1(f)** inset, SI **Figure 2(c)**), we see  
 124 that the Fourier amplitudes of multiple modes compete with each other initially before an elliptic  
 125 mode (corresponding to a strongly localized state) is amplified as excavation progresses (shown in  
 126 **Figure 1(f)**, SI **Figure 2(b)**). All together, our quantitative observations show that an initially isotropic  
 127 and homogeneous distribution of ants in the corral induces exploration of multiple potential tun-  
 128 neling paths that transitions into the exploitative excavation of one specific location that eventually  
 129 leads to an excavation route.

### 130 **Model of cooperative excavation**

In order to understand the dynamics of this cooperative excavation we model the ants using dis-  
 crete agents that mimic the microscopic behaviors of ants and also obtain a coarse-grained field  
 model for their evolution by averaging over the local actions. In the 2-dimensional agent-based  
 model each ant is represented as a circular disk of radius  $a$  with center position  $\mathbf{r}_j(t)$  and orientation  
 $\hat{\mathbf{p}}_j(t)$  where  $j = 1 \dots n$ ,  $n$  being the number of ants in the domain (see **Figure 3(a)**). We approximate  
 the confining corral in the experiments using discrete boundary elements which the agents can  
 pick and place in the interior of the domain (see **Figure 3(b)**). The agents engage in exploration  
 within the corral in the absence of external gradients, consistent with observations (**Trible et al.,**  
**2017**) and their motion is rectified either by the presence of pheromone gradients or reinforcing  
 antennating signals (**Hölldobler et al., 1990; Reinhard and Srinivasan, 2009; Waters and Bassler,**

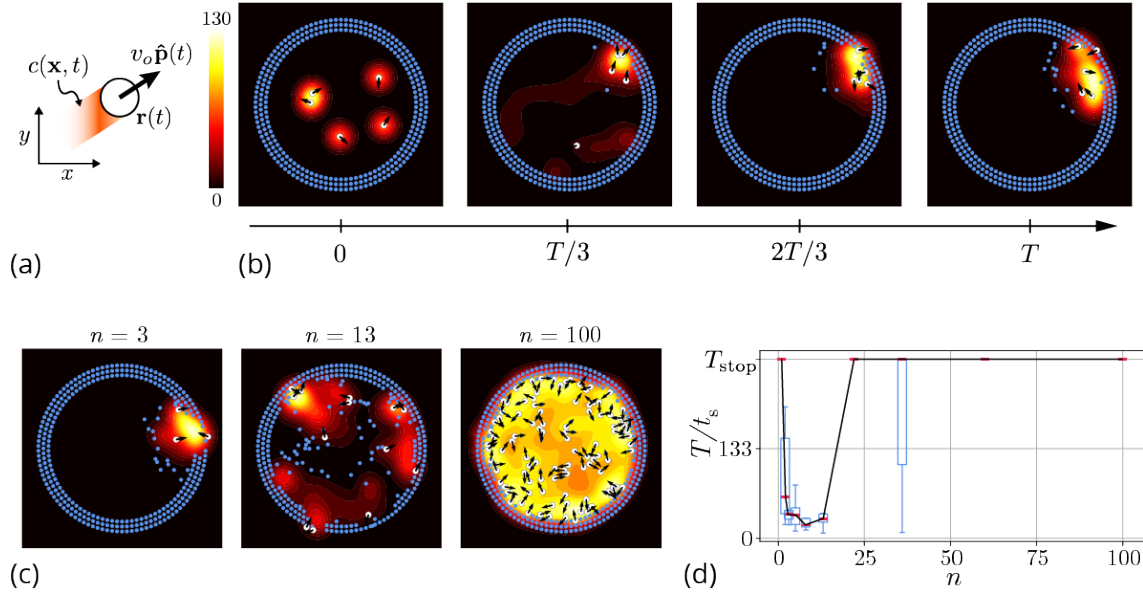


**Figure 3. Agent-based simulation** (a) Schematic of the agents in our simulation captured by their position  $\mathbf{r}(t)$  and orientation  $\hat{\mathbf{p}}(t)$  moving at speed  $v_o$ . These agents generate an antennating field  $c(\mathbf{x}, t)$  at a constant rate  $k_+$  which decays at a rate  $k_-$ . (b) Progression of cooperative excavation of the corral by 5 agents as they pick elements from the boundary and drop them in the interior (see sec. [Table 1](#) for parameters). Color bar shows the magnitude of antennating field and it varies between 0-130. (c) Snapshot of the dynamics at the end of simulations corresponding to  $T_{\text{stop}} = 266$  for the number of agents  $n = 3, 13, 100$ . We see that agents can go from excavating successfully to being trapped in their own communication field. (d) Box plot showing the time taken to excavate out of the corral  $T/t_s$  (non-dimensionalized using  $t_s$  - time taken for an agent to travel the entire domain) as a function of the number of agents  $n$  in the corral when  $T_{\text{stop}} = 266$ . For very small and very large number of agents the collective does not excavate out as the median  $T/t_s = T_{\text{stop}}$  and they escape fastest for  $n = 8$ .

[2005; Gordon et al., 1993; Hillen and Painter, 2009; Toffin et al., 2009](#)). This is because communication between ants is mediated either via antennation and/or pheromones which act as two different modes of information transfer. The former involves information moving with the ants and the latter leads to changes in the fixed environment. However, when ants move slowly relative to the time for the decay of the memory associated with antennation with other ants, the dynamics of both these processes is similar. Then the signals laid down (or transported) by ants increases locally at a rate proportional to their density ([Gordon, 2021](#)), and is subject to degradation and diffusion slowly. Accounting for these effects, we arrive at the following dynamical equations for the evolution of  $\mathbf{r}_j(t), \theta_j(t), c(\mathbf{x}, t)$ :

$$\dot{\mathbf{r}}_j(t) = \underbrace{v_o \hat{\mathbf{p}}(t)}_{\text{Self-propulsion}}, \quad (1)$$

$$\dot{\theta}_j = \underbrace{G \nabla_{\perp} c}_{\text{Antennation feedback}} + \underbrace{\eta_j(t)}_{\text{Exploration}}, \quad (2)$$

$$\partial_t c = \underbrace{D_c \nabla^2 c}_{\text{Diffusion}} + \underbrace{k_+ \sum_{j=1}^n \mathcal{H}(\mathbf{r}_j(t); a)}_{\text{Production}} - \underbrace{k_- c}_{\text{Decay}}. \quad (3)$$

131 Here the orientation of the agents is given by  $\hat{\mathbf{p}}_j = (\cos \theta_j, \sin \theta_j)$  with  $\theta_j$  being the heading an-  
 132 gle,  $v_o$  the characteristic speed of the agents,  $\eta_j$  is a Gaussian white noise with correlation function  
 133  $\langle \eta_j^k(t) \eta_j^l(t') \rangle = 2D_a \delta_{k,l} \delta(t - t')$ . Further the agents produce antennating field at a rate  $k_+$  which  
 134 decays at a rate  $k_-$ . Here the production of the antennating field is captured by a square function  
 135  $\mathcal{H}(\mathbf{r}_j, a) = \{1 \text{ if } |\mathbf{x} - \mathbf{r}_j|^2 - a^2 \leq 0; 0 \text{ if } |\mathbf{x} - \mathbf{r}_j|^2 - a^2 > 0\}$ . We assume that the gradient in the antennating  
 136 field along the local normal determines the rotation of the agents by a magnitude  $G$  is the rotational  
 137 gain. In order for the agents to initiate the excavation process, they can pick the elements from

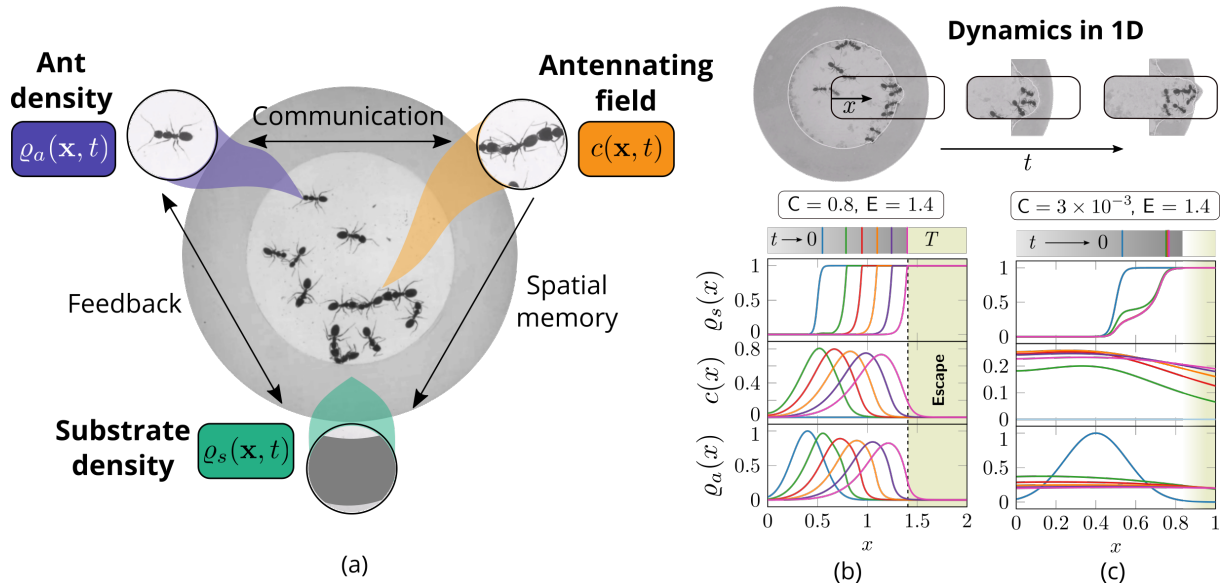


**Figure 4. Cooperation via organism-environment-organism interaction** (a) Schematic of the model showing the interaction between the different spatio-temporal fields required to capture cooperative excavation of ants: ant density,  $\rho_a(\mathbf{x}, t)$ ; concentration of antennating field,  $c(\mathbf{x}, t)$  capturing inter-ant communication; density of corral,  $\rho_s(\mathbf{x}, t)$  representing the soft corral which the ants excavate. We capture the dynamics of excavation by ants close to the excavation site using the 1-dimensional version of *Equation 4-Equation 5*. (b, c) Temporal progression of the corral density, antennating field and the ant density showing successful excavation for high cooperation captured using the non-dimensional number, C (representing non-dimensional strength of cooperation amongst ants) and faster excavation, captured using E. For reduced cooperation ants' diffusion dominates and only partial tunnels are formed (see SI 2 for details).  $T$  here is the time for excavating out of the corral. The agent density is a gaussian function centered around  $x = 0.5$ .

138 the boundary and drop them in the interior of the corral only when the local concentration of the  
139 antennating field is beyond a critical threshold  $c^*$  ensuring that the agents start performing a task  
140 only after enough number of interactions among themselves, consistent with observations (**Gor-**  
141 **don, 2021; Gordon et al., 1993**). **Figure 3(b)** shows snapshots of simulation following the dynamics  
142 of *Equation 1-Equation 3* where the agents excavate successfully out of the corral when we ensure  
143 that the gradient following behavior is strong (see SI 2 for details). Given such a dynamics, we ex-  
144 pect the time taken to excavate out of the corral is going to be a function of the number of agents.  
145 In order to characterize the behavior we vary the number of agents from  $n = 1 - 100$  and find that  
146 for very small or large number of agents in the corral, the agents do not excavate out during the  
147 time of simulations,  $T_{\text{stop}}$  (see **Figure 3(c, d)**), seen as saturation in the excavation time  $T/t_s$ .

In the agent based simulations we can encode the behavior of ants with all its details such as prescribing the sequence of actions taken during the execution of pick and place task, the path taken during the dropping of debris in the interior of the coral, changes in orientation after inter-ant interaction and so on. It also helps us get an estimate time of excavation given these behavioral rules. Further, as we have seen, we can study the effect of number of agents on the time of excavation. However for each of these actions there is a parameter associated with it in the simulations which results in a large dimensional phase-space. These simulations, moreover, are computationally expensive as one needs to couple the antennating field equations (which is a partial differential equation) with discrete agents and also evaluate the mutual interaction of all the agents in the corral. In order to gain insights into the relevant parameters that describe our observations in the agent-based model and also the parameters that govern the macroscopic dynamics of the collective, we develop a theoretical framework that coarse-grains over the fast times and short length scale actions of the agents, i.e. considers spatial variations over scales much larger than a "mean-free path" and "collision time" associated with agent-agent interactions. A formal coarse-graining of the actions from the discrete agent-based simulations to the continuum is often difficult and one resorts to closure models to account for the effects of fluctuations accurately. Our effec-

tive theory attempts to couple three slowly-varying spatio-temporal fields: the ant density  $\rho_a(\mathbf{x}, t)$ , a communication field  $c(\mathbf{x}, t)$  representing processes such as antennation and pheromone-based communication that the ants use to communicate with each other, and the corral density  $\rho_s(\mathbf{x}, t)$ , shown schematically in **Figure 4(a)** to explain our observations in terms of a small number of effective measurable parameters. In the continuum picture, the agents' random motion is captured using diffusion of the density while the rectified motion due to pheromone gradients is captured through chemotaxis, in addition to being self-propelled with a velocity  $\mathbf{u}_a$  that is related to the local environment. Finally, motivated by observations of antennation (**Gordon, 1999; Pagliara et al., 2018**), we assume that when the ants are stimulated by the presence of the corral past a threshold of antennation,  $c^*$  they start excavating. The rate of excavation is assumed to be proportional to the difference in the pheromone concentration relative to the threshold value i.e.  $\sim (c - c^*)$  (see SI sec. 1 further details). Accounting for these effects, we arrive at the following dynamical equations for the evolution of  $\rho_a(\mathbf{x}, t)$  and  $\rho_s(\mathbf{x}, t)$ :

$$\partial_t \rho_a = - \underbrace{\nabla \cdot (\mathbf{u}_a \rho_a)}_{\text{Self-propulsive advection}} + \nabla \cdot \left( \underbrace{D_a \nabla \rho_a}_{\text{Diffusive flux}} - \underbrace{\chi \rho_a \nabla c}_{\text{Tactile feedback}} \right), \quad (4)$$

$$\partial_t \rho_s = - k_+ \rho_s \underbrace{\left\{ \Theta(c - c^*) \right\}}_{\text{Antennating field threshold}} \times \underbrace{\left\{ \Theta(\rho_a - \rho_a^*) \right\}}_{\text{Ant density threshold}}. \quad (5)$$

148 Here, in the first equation, the ant advection velocity is assumed to have the form  $\mathbf{u}_a = v_o(1 -$   
 149  $\rho_s/\rho_o)\hat{\mathbf{p}}$  where  $v_o$  is the characteristic speed of the agents, and  $\hat{\mathbf{p}}$  is a unit vector pointing along the  
 150 radial ( $\theta$ ) direction, and the term  $(1 - \rho_s/\rho_o)$  reflects the fact that excavating ants are slowed down  
 151 by their labor;  $D_a$  is the diffusivity of ants,  $\chi$  is a chemotactic gain associated with the strength of  
 152 antennating-field-following behavior that captures the intensity of the tactile feedback that ants  
 153 experience (related to the rotational  $G$  in the agen-based model);  $k_+, k_-$  are the rate of production  
 154 and decay of the antennating/pheromone field, and  $D_c$  is its diffusivity (see SI sec. );  $k_s$  is the rate of  
 155 excavation of the corral and  $\rho_a^*, c^*$  are the threshold concentration of ant density and antennating  
 156 field required to initiate excavation. We assume that the behavioral switches have simple switch-  
 157 like responses modeled here via the Heaviside function  $\Theta(x)$  (or its regularization via hyperbolic  
 158 or Hill functions). It is useful to note that in the absence of excavation dynamics, our framework  
 159 reduces to the well known Keller-Segel model for chemotaxis (see (**Hillen and Painter, 2009**) for  
 160 a recent review) (also detailed in SI sec. 2). The coupling of ant behavior to the dynamics of ex-  
 161 cavation introduces the all-important notion of *functional* collective behavior linking active agents,  
 162 communication channels (the antennating and pheromone fields) and a dynamic, erodible corral  
 163 that characterizes function in terms of progress towards task completion.

### 164 Model parametrization and description

The evolution of the ant density in **Equation 4** is a combination of three dynamical processes: ant migration, their diffusion and biased motion due to feedback from contact with other ants (captured using the antennating field). There are three time-scales associated with these three processes: ant density diffusion time-scale  $\tau_a \sim l^2/D_a$ , ant collective migration time-scale  $\tau_o \sim l/v_o$  and the time-scale associated with taxis due to antennating field gradient  $\tau_x \sim l^2/\chi c_o$ , where  $l$  is a characteristic length-scale which is either the width of the corral to be tunneled  $L$  (which is assumed to be of same order as width of initial ant density profile  $l_a$ ) or the length-scale due to antennating field diffusion and decay,  $l \sim (D_c/k_-)^{1/2}$  or the length-scale due to the advection of ant density and diffusion,  $l \sim D_a/v_o$ . The antennating field in **Equation 3** on the other hand is governed by three processes, which are the generation of antennating field at ant locations, decay and diffusion in the intensity representing loss in memory as well as errors in their measurements. We have three more time-scales due to these processes: antennating field production time-scale  $\tau_+ \sim c_o/(k_+\rho_o)$ , diffusion time-scale  $\tau_c \sim l^2/D_c$ , and decay time-scale  $\tau_- \sim 1/k_-$ . Lastly, the corral is excavated as a

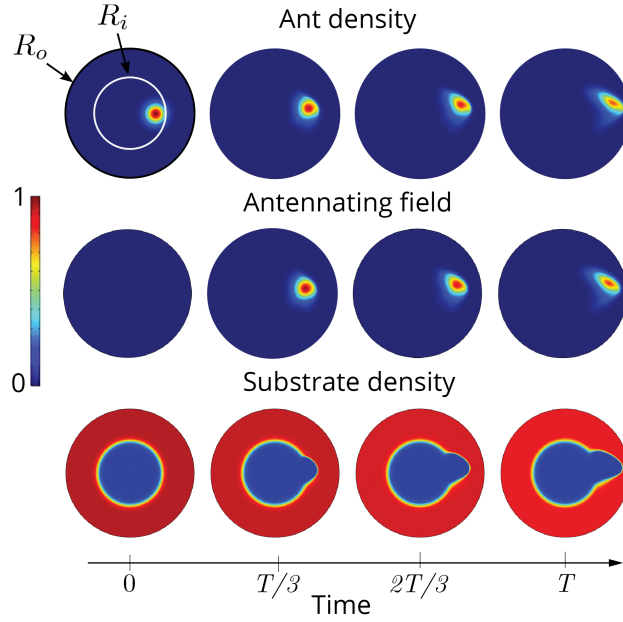


**Figure 5.** Two dimensional simulations showing the evolution of the ant density  $\rho_a$ , antennating field  $c$  and the corral density  $\rho_s$  by evolving **Equation 4-Equation 5**, capturing successful tunneling for non-dimensional numbers  $C = 0.8$ ,  $E = 1.44$  and time of simulation  $T = 20.0$ . The list of dimensional parameters used in the simulation are indicated in the SI **Figure 1(f)**. Radius of the outer boundary,  $R_o$  is 5 non-dimensional units and the inner boundary is  $R_i = 2.5$  (see SI 2 for details). Color bar shows the magnitude of different variables and they vary between 0-1.

function of time with a characteristic time-scale  $\tau_s \sim 1/k_s$  as in **Equation 5**. Here  $\rho_o$  is the average density of the ants defined by  $\rho_o = \int \rho_a dx / L$  where  $L$  is the domain size. This is a natural scale of the ant density as **Equation 4** is in conservative form and the net density of the ants is preserved over the evolution. The dynamics has the threshold  $c^*$  as the only intrinsic intensity scale of the antennating field. However this is not a natural scale for the antennating field as the threshold cannot be tuned but is often fixed in the system. Instead we use the maximum antennating field produced during the dynamics to be  $c_o$ . The list of time-scales and length-scales associated with the different processes in the model are in **Table 2**. With seven time-scales the parameter space of the model is quite large. We thus look at various limits in this parametric space to glean insights into the mechanisms of task execution. Although our model has a number of different time-scales parameters (see SI sec. 2 for a list along with their ranges), two non-dimensional numbers arising out of these different time-scales are qualitatively important in capturing the etho-space of collective excavation: (i) the scaled cooperation parameter defined as  $C = \tau_a / \tau_x = \chi c_o / D_a$  which determines the relative strength of antennation (gradient-following) to ant diffusion with  $c_o$  being the maximum amplitude of the antennating field, (ii) the scaled excavation rate,  $E = \tau_v / \tau_s = k_s l / v_o$ . Here,  $l / v_o$  is the characteristic time-scale of ant motion, with  $l \sim \min[(D_c / k_-)^{1/2}, l_a]$ , where  $l_a$  is the ant size (see SI sec. 2 for details). In addition, we have the ratio of ant motion time-scale vs the diffusive time-scale,  $V = \tau_x / \tau_a = v_o l / D_a$ . The three non-dimensional numbers  $C, E, V$  arise out of the dynamics of the ant density field in **Equation 4** and the corral in **Equation 5**. Two additional non-dimensional numbers follow from the dynamics of the antennating field in **Equation 3**: comparing the rate of production of pheromone with diffusion or decay, we write  $\hat{k}_{\pm} = \tau_- / \tau_{\pm} = k_{\pm} \rho_o / (k_- c_o)$  and  $D_c = \tau_- / \tau_c = D_c / (l^2 k_-)$ . Then the complete set of non-dimensional numbers that capture the dynamics of the ant collective is given by

$$C = \frac{\chi c_o}{D_a}, E = \frac{k_s l}{v_o}, V = \frac{v_o l}{D_a}, \hat{k}_{\pm} = \frac{k_{\pm} \rho_o}{k_- c_o}, D_c = \frac{D_c}{l^2 k_-}.$$

In terms of these parameters, the dynamics of the ant density, the antennating field and the corral density can be written in non-dimensional form as

$$\partial_t \rho_a + \nabla \cdot [(C \nabla c + V(1 - \rho_s)) \rho_a] = \nabla^2 \rho_a, \quad (6)$$

$$\partial_t c = D_c \nabla^2 c + \hat{k}_\pm \rho_a - c, \quad (7)$$

$$\partial_t \rho_s = -\frac{1}{4} E \rho_s (1 + \tanh[\alpha_c (c - c^*)]) \times (1 + \tanh[\alpha_c (\rho_a - \rho_a^*)]). \quad (8)$$

165 To complete the formulation of our model, we also need to specify some initial conditions for the  
166 three fields and boundary conditions for the ant density, the pheromone density, and the location  
167 of the corral boundary which are detailed in the sec. 2.

## 168 Results

### 169 Linear analysis

170 Before we can look at the different limits of the phase-space defined by the non-dimensional num-  
171 bers, we show that the excavation process is an instability which is triggered by the scaled exca-  
172 vation parameter  $E$  in the system. We can see that the homogeneous state  $\rho_a^{SS} = \rho_a^*$ ,  $c^{SS} = c^* =$   
173  $k_+ \rho_o / k_-$ ,  $\rho_s^{SS} = 1$  is a steady state of the above equations. This steady state represents a special  
174 case where the density of the ants is close to the critical threshold and so is the strength of the  
175 antennating field. Perturbation analysis helps us determine the mode of instability close to this  
176 threshold where the ants have accumulated and generated an effective antennating field.

177 In order to understand the short time dynamics close to this steady state, we introduce a  
178 perturbation around this configuration and expand it using a plane wave ansatz. In 1D this be-  
179 comes:  $\{\rho_a(x, t) - \rho_a^{SS}, c(x, t) - c^{SS}, \rho_s(x, t) - \rho_s^{SS}\} = \{\tilde{\rho}_a(k), \tilde{c}(k), \tilde{\rho}_s(k)\} \exp(ikx + \Omega t)$  where we assume  
180 that  $\|\tilde{\rho}_a\|, \|\tilde{c}\|, \|\tilde{\rho}_s\| \ll 1$ . Then the linearized equations for ant density in **Equation 6** reads as:  
181  $(\Omega + k^2) \tilde{\rho}_a + ikV \tilde{\rho}_s \rho_o = k^2 C \tilde{c}$  and the antennating field in **Equation 7** becomes:  $\tilde{c} = \hat{k}_\pm \tilde{\rho}_a / (\Omega + 1 + D_c k^2)$ ,  
182 and lastly the corral density in **Equation 8** becomes  $\Omega \tilde{\rho}_s = -E \tilde{\rho}_s / 2$ . From this we see that the growth  
183 rate  $\Omega = -E/2$ , is independent of all other parameters in the system. Thus tunneling begins when  
184  $E > 0$ , once the ants have created a sufficiently large spatially diffuse antennating field, and the  
185 corral excavation rate determines the dynamics of the instability. To understand the dynamics of  
186 excavation of the corral and the different phases of collective behavior, we now explore the role  
187 of the other non-dimensional numbers.

### 188 Limits of phase-space

189 In this section we discuss the different limits of the phase-space defined by the non-dimensional  
190 numbers  $\{C, E, V, \hat{k}_\pm, D_c\}$  and the thresholds  $\rho_a^*, c^*$ . We use non-dimensional numbers to describe  
191 the region in phase-space but revert to dimensional form to keep the analysis mechanistically trans-  
192 parent.

193 Small thresholds, when  $\rho_a^* \ll \rho_o$  and  $c^* \ll c_o$

194 When  $\rho_a^* \ll \rho_o$  and  $c^* \ll c_o$ , partial tunneling can be achieved even if we start with an inhomogeneous  
195 ant density  $\rho_a$ , independent of the pheromone dynamics and is thus very inefficient. Depending on  
196 whether the ants can tunnel fast or slow relative to their motion, i.e. depending on the value of the  
197 ratio  $\tau_s / \tau_v$ , the ants can excavate through the corral completely ( $\tau_v / \tau_s \ll 1$ ) or partially ( $\tau_v / \tau_s \leq 1$ )  
198 (ref **Table 2**).

199 On the other hand if the ants are moving randomly, i.e. in the diffusion-dominated regime,  
200 then they can still tunnel through the corral if  $\tau_c \sim \tau_s$  and achieve partial tunneling if  $\tau_c \lesssim \tau_s$ . In non-  
201 dimensional terms this translates to  $V \sim \mathcal{O}(1)$ ,  $C \ll 1$  or  $V, C \ll 1$  for the ant density and  $E \sim \mathcal{O}(1)$  for  
202 the corral evolution. It is worth mentioning that we use the width of the corral,  $L$  as the relevant

203 length-scale to define these non-dimensional numbers. SI **Figure 1(a)** has simulations showing this  
 204 behavior both in the tunneling and the partial tunneling phase.

205 Cooperation dominated regimes when  $C \gg 1$  and  $E, V \rightarrow 0$

206 For efficient excavation, the ants need to work collectively, i.e. be localized and excavate fast. Lo-  
 207 calization in space leads to cooperation via feedback from the antennating field (see **Figure 4(b)**) -  
 208 this keeps the collective together and prevents it from diffusing away. For successful excavation,  
 209 ants also need to migrate towards the corral and tunnel through it, so that their effective speed  $v_o$   
 210 needs to be non-zero. We first look at the dynamics of the ant density and the antennating field in  
 211 the absence of migration i.e.  $V \rightarrow 0$  (we also neglect the corral dynamics for now). There are three  
 212 regimes arising out of the antennating field dynamics which we now consider separately:

- **Diffusion dominated regime:** When the generated antennating field rapidly diffuses away, i.e.  $D_c \sim \hat{k}_{\pm} \gg 1$ , then the antennating field and the ant density evolve as

$$-D_c \nabla^2 c = k_+ \rho_a, \quad (9)$$

$$\partial_t \rho_a + \chi \nabla \cdot (\rho_a \nabla c) = D_a \nabla^2 \rho_a. \quad (10)$$

213 In this limit, we obtain the well known Keller-Segel model for bacterial aggregation (**Hillen and**  
 214 **Painter, 2009**). Balancing the effects of diffusion of the antennating field with the production  
 215 term, we obtain a length-scale over which gradients in antennating field is felt which is  $l \sim$   
 216  $(D_c c_o / k_+ \rho_o)^{1/2}$ . Accumulation in ant density can happen when the ants can sense this gradient  
 217 which corresponds to large  $C$ . On the other hand for small  $C$ , the ant density diffuses out. The  
 218 diffusion of the antennating field drives migration of ants due to detection of gradients thus  
 219 resulting in generation of more antennating field in the new location. This process continues  
 220 to happen perpetually resulting in piling up of ant density.

- **Decay dominated regime:** When the generated antennating field all decays fast we are in the limit of  $\hat{k}_{\pm} \sim \mathcal{O}(1), D_c \ll 1$ . The dynamics of the antennating field reduces to  $c \approx (k_+ / k_-) \rho_a$ . The ant density evolution then becomes,

$$\partial_t \rho_a + \frac{\chi k_+}{k_-} \nabla \cdot (\rho_a \nabla \rho_a) = D_a \nabla^2 \rho_a. \quad (11)$$

221 When the chemocactic coefficient  $\chi$  is large, i.e. in dimensionless terms  $C \gg 1$ , the ant collec-  
 222 tive undergoes jamming. This can be seen most easily by linearizing the equation **Equation 11**  
 223 about a uniform ant density  $\rho_o$  and recognizing that this can lead to an effective negative dif-  
 224 fusivity and thus the onset of clustering and a spatio-temporal focusing of the ant density;  
 225 we leave a detailed analysis of the characteristics of this for future study.

- **Competing effects of diffusion and decay:** Comparing the diffusion of the antennating field and its decay, i.e. letting  $D_c \sim \mathcal{O}(1)$ , yields a length scale  $l \sim (D_c / k_-)^{1/2}$  which defines the zone of influence of the field. We use this length scale to arrive at the non-dimensional tunneling rate indicated in **Figure 8**. Then, in the limit when the antennating field generation rate is large, i.e.  $\hat{k}_{\pm} \gg 1$ , the field generates a gradient that drives collective ant motion and excavation.

232 All together, our analysis shows that the dynamics of the antennating field controls the aggregation  
 233 or diffusion of ant density. But this is alone is not enough; for efficient excavation, especially when  
 234 the activation thresholds for excavation and localization  $\rho_a^*, c^*$  are large, we need both cooperation  
 235 and finite velocity of migration so that the ant collective can eventually tunnel through. Other  
 236 regimes associated with partial tunneling, jamming or diffusion arise as the parameters are varied,  
 237 as listed in **Table 3**.

252 When accounting for the effects of excavation and migration of the ants i.e.  $E, V \neq 0$ , by solving  
 253 the governing **Equation 4-Equation 5** in a one-dimensional setting (ref SI sec. 2) captures the two  
 254 limits of the excavation behavior seen in experiments; For large excavation rate  $E$  and cooperation

239 **Box 1. Ant behavior → Model → Robot behavior**

240 Ants inside the corral move around, communicating with each other using their antennae  
 241 before they cooperatively excavate the agarose corral. Though the detailed spatio-temporal  
 242 dynamics of each ant's behavior is different at the microscopic level, we see that the coopera-  
 243 tion between the ants results in a persistent density front (see **Figure 1(d, e)** and **Figure 2**) that  
 244 excavates the substrate. In the theoretical description of the collective's dynamics, the relevant  
 245 behaviors are encoded through mutual interaction between the ants (via the antennating  
 246 field) and the substrate. Such a description also inspires the robotic mimics that capture the  
 247 ant collective's average behavior. We list below the comparison between relevant behaviors  
 248 in ants and their analogous encoding in the theoretical model as well as in the robots.

Ants	Theoretical model	Robots
Discrete ants	Ant density, $\rho_a(\mathbf{x}, t)$	Discrete robots
Antennae communication	Communication field, $c(\mathbf{x}, t)$	Photomone field
Agarose corral	Substrate density, $\rho_s(\mathbf{x}, t)$	Boundary elements
Motility	Self-propulsive advection, $\mathbf{u}_a$	Mobile agents
Exploratory behavior	Density diffusion, $D_a \nabla \rho_a$	Random walk
Tactile feedback	Antennating field taxis, $\chi \rho_a \nabla c$	Phototaxis
Biting behavior	Excavation rate, $k_s$	Collection and deposition
Neural control	Dynamics of ant density	Behavioral rules

250 **Box 1 Table 1.** Comparison of relevant variables, basic behaviors, and behavioral coordination between  
 251 ant experiments, theoretical model and robotic implementation.

255 parameter,  $C$ , we see coordinated excavation (shown in **Figure 4(b)**), while decreasing the cooper-  
 256 ation parameter leads to disorganized excavation (shown in **Figure 4(c)**) (see SI **Figure 1**). While  
 257 a direct comparison with the behavior of ants is not easy owing to the difficulty of inferring the  
 258 dynamics of information transfer through antennation, the minimal assumptions we have made  
 259 about the antennating field dynamics suffice to capture the macroscopic behavior of the collective.  
 260 All together, our agent-based model and the phase-field model shows the emergence of cooper-  
 261 ativity without the need for a plan, optimization principle, or an internal representations of the  
 262 world, but via the environmentally-mediated communication between agents (**Mataric, 1993**) that  
 263 leads to task completion.

264 **Robotic collective excavation**

265 Although the collective behavior of the ants is qualitatively captured by our simplified theoretical  
 266 model, we can ask if the coarse-grained averaging over microscopic dynamics of the communica-  
 267 tion field might affect the emergence of the task in experiments. It is thus unclear if the simplifying  
 268 assumptions underlying the model are sufficiently general, since we are unable to control the mi-  
 269 croscopic behaviors in the system. To go beyond our ability to merely explain the observations of  
 270 ant behavior using our theoretical framework, we asked if we might be able to synthesize or recre-  
 271 ate the behavior in robotic mimics, and probe a larger range of the parameters and phase-space  
 272 spanned by  $C, E$ , than our experiments allowed us to.

273 For this, we turn to a robotic platform to synthesize collective functional behaviors that arise  
 274 from simple behavioral rules underlying individual programmable robots. Our custom designed  
 275 robot ants (RAnts) are inspired by many earlier attempts to create artificial agents that are mobile  
 276 and follow simple rules (**Braitenberg, 1986; Brooks, 1991; Simon, 1996**), can respond to virtual  
 277 pheromone fields (**Sugawara et al., 2004; Garnier et al., 2007**) and are capable of robotic exca-  
 278 vation (**Aguilar et al., 2018**). Our autonomous wheeled robots can exhibit emergent embodied  
 279 behavior (**Bricard et al., 2013**), and are flexible enough to allow for a range of stigmergic interac-

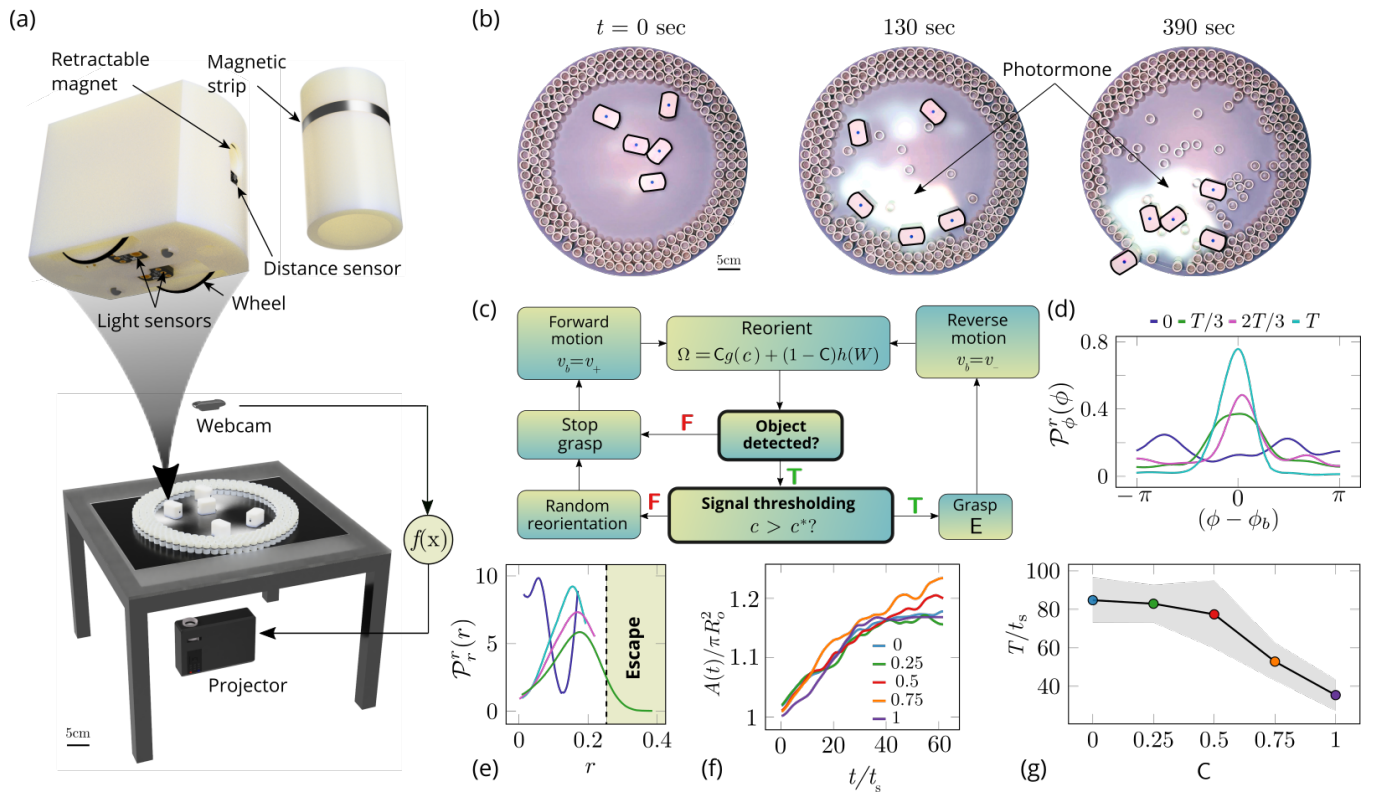


**Figure 6. Emergent cooperative excavation dynamics in robotic ants** (a) Robot Ant (RAnt) set-up. A mobile RAnt is placed in an arena 50cm in diameter surrounded by three layers of cylindrical boundary elements totalling 200 elements. The outermost layer is prevented from being pushed out of the arena by a circular ring. A scalar concentration field (*photormone* field) is projected onto a plane whose intensity can be measured by a RAnt. The position of each RAnt is tracked using a webcam. Each RAnt can pick up and drop the discrete boundary elements using a retractable magnet. (b) Series of snapshots at different times of the excavation process for a cooperation parameter  $C = 1$ . (c) Flowchart of the RAnt programming. A base locomotion speed  $v_b$  is stored internally and the rate of change  $\Omega$  of the heading is a function of the cooperation parameter  $C$ , the photormone concentration  $c$ , and a stochastic process  $W$  (Brownian motion). A photormone threshold  $c^*$  determines whether an object is grasped (with probability  $E$ ) after it is detected by the distance sensor. (d) Orientation distribution of the RAnt density  $\mathcal{P}_\phi^r(\phi, t)$  as a function of the azimuthal position  $\phi$ .  $\phi_b$  is the orientation of the excavated tunnel. The density is plotted for different times. (e) Radial distribution of the RAnt density  $\mathcal{P}_r^r(r, t)$  within a sector of  $\pi/2$  centered around the position of the excavated tunnel as a function of distance from the center of the arena  $r$ . The density is plotted for the same times as in (d). (f) Confinement area  $A(t)$  as a function of time, normalized by initial circular confinement with radius  $R_o$  for different cooperation parameter  $C$ . (g) Normalized excavation time  $T$  as a function of cooperation parameter  $C$ , averaged over 5 experiments per cooperation parameter. Every experiment was run until the first RAnt excavated out or the experiment duration exceeded 15 minutes.

280 tions with the environment (Werfel et al., 2014; Petersen et al., 2019). This is made possible by  
 281 having each RAnt equipped with an infrared distance sensor to detect obstacles and other RAnts,  
 282 a retractable magnet that can pick up and drop wall elements with a ferromagnetic ring (shown  
 283 in Figure 6(a)), and the ability to measure a virtual pheromone field generated by a light projected  
 284 (from below) onto the surface of a transparent arena they operate in (see Figure 6(a, b)) (Theraulaz  
 285 and Bonabeau, 1995; Sugawara et al., 2004; Garnier et al., 2007; Wang et al., 2021). The intensity  
 286 of this “photormone” field follows the antennating field Equation 3 and thus follows the dynam-  
 287 ics of a field that is linked to the the locations of the RAnts and diffuses and decays away from  
 288 it. The photormone field is realized by a projected luminous field on the arena, which the robots  
 289 can sense. This allows us to use a local form of Equation 4-Equation 5 to define a robot’s behavior  
 290 in terms of an excavation rate  $E$ , a cooperation parameter  $C$ , and a threshold concentration for  
 291 tunneling  $c^*$ . This is encoded in the behavior-based rules (see Figure 6(c) and SI sec. 3 for more  
 292 details), that induces the following behavior: (i) follow gradient of projected photormone field; (ii)  
 293 avoid obstacles and other RAnts at higher photormone locations; (iii) pick up obstacles from high  
 294 photormone locations and drop them at low concentration levels. Since the robots have no sym-  
 295 bolic representation of the different signals they sense (e.g. they cannot distinguish another RAnt

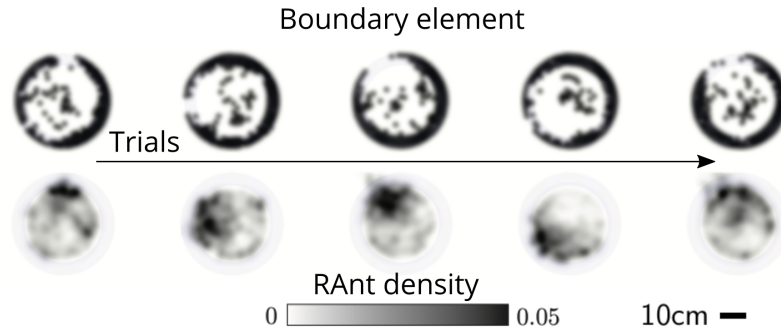


**Figure 7. Averaged RAnt dynamics** Ultimate distribution of boundary elements and averaged RAnt density field (in units of  $\#/cm^2$ ) over the full duration of experiments for different trials.

296 from a wall element, since both merely produce a bump in the sensor signal), the observed behav-  
 297 ior emerges from this simple sequence by depending on the current state of the environment and  
 298 the robot.

299 Varying the parameter  $C \in [0, 1]$  allows us to tune the individual behavior from random motion  
 300 ( $C = 0$ ) to tracking the photormone gradient ( $C = 1$ ). Varying the non-dimensional excavation rate  $E$   
 301 changes the frequency at which the robots execute pick-and-drop behavior with detected objects,  
 302 and serves to mimic what arises in ants as a function of their morphology and caste (see SI sec. 1 for  
 303 more details). For a specific value of these parameters, we followed the collective behavior of RAnts  
 304 by averaging their position over several pick-and-drop timescales to obtain the RAnt density field  
 305  $\rho_r(r, \phi, t)$ , just as for ants. When all the RAnts are programmed to have a cooperation parameter  $C =$   
 306 1, RAnts initially explore the region without picking the boundary element until the photormone  
 307 concentration  $c \sim c^*$ , which happens once a particular location has enough visits by other RAnts. As  
 308 for ants, we calculate the radially averaged RAnt density  $\mathcal{P}_r^r(\phi, t) = \int \rho_r(r, \phi, t) dr$ ; **Figure 6(d)** shows  
 309 how RAnt density localizes at a (random) value of the azimuthal angle. As excavation progresses,  
 310 the RAnt density propagates radially outwards as a density front just as in ants, shown in **Figure 6(e)**  
 311 in terms of the quantity  $\mathcal{P}_r^r(r, t) = \int \rho_r(r, \phi, t) d\phi$  (also shown in **Figure 7** for different trails when  
 312  $C = 1$ ). Concomitantly, as excavation progresses, the corral area increases (**Toffin et al., 2009**);  
 313 interestingly the scaled corral area  $A(t)/\pi R_0^2$  is independent of the cooperation parameter  $C$  as  
 314 shown in **Figure 6(f)** (all RAnts were programmed to have the same excavation rate).

315 However, cooperation does change the time for excavation; in **Figure 6(g)** we show the average  
 316 excavation time (scaled by the characteristic time it takes for a rant to traverse the arena) and  
 317 see that  $T/t_s$  decreases with an increase in the cooperation parameter  $C$ . RAnts excavated out  
 318 every time for  $C > 0.5$ , but are unable to complete excavation for low cooperation parameters  
 319 (within a 15 minute time window). Our results show that it is the localized collective excavation  
 320 of RAnts mediated by photormone-induced cooperation that is responsible for efficient tunneling  
 321 and excavation; for low values of the cooperation parameter, tunneling is defocused and global,  
 322 and thus not as effective (see SI **Figure 2**). When  $E \rightarrow 0$  (vanishing probability for a successful  
 323 pick up) but strong cooperation (see **Figure 8** and SI sec. for theoretical predictions), the RAnts get  
 324 jammed because they follow the photormone field they generate but are unable to tunnel through  
 325 the boundary constriction. On the other hand, when  $E$  is small and  $C$  is small, the agents do not  
 326 cooperate and their diffusive behavior prevents successful tunneling. The range of strategies can  
 327 be visualized in a two-dimensional phase space spanned by the variables  $E$  and  $C$  shown in **Figure 8**.  
 328 Low values of  $C$  and  $E$  lead to diffusive (and non-functional) behavior, while high values of these  
 329 variables lead to coordinated excavation, with the other two quadrants corresponding to jammed  
 330 states (large  $C$ , small  $E$ ) and partially tunneled states (large  $E$ , small  $C$ ). Interestingly, these states  
 331 are also observed as transients in our ant experiments, for example in the initially diffused state  
 332 that is characterized by random motion inside the corral, when transiently jammed states and

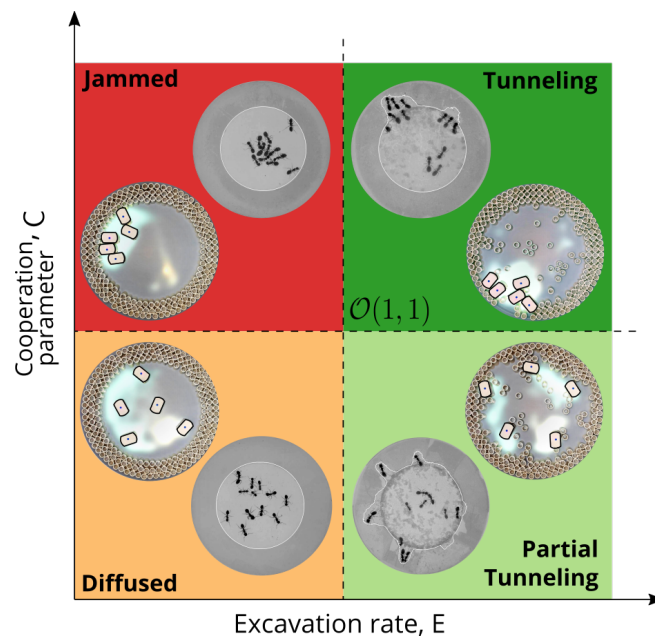


**Figure 8. Phases of cooperation** Phase-diagram of cooperative task execution with different phases seen in ants and RAnts. In the robotic experiments we tune the Cooperation parameter  $C$  and the Excavation rate  $E$  while in the ant experiments we change the caste mixture. In the ant experiments we see the jammed and diffused phases transiently before the ants relax to cooperative excavation.

333 partial tunneling occur (see Video3).

### 334 Discussion

335 Our analysis of collective behavior in a functional task, excavation, attempts to use observations  
 336 of ants to abstract the general features that are amenable to a theoretical treatment of the fields  
 337 and rules that are also sufficient to explain them, and eventually to create a robotic system that  
 338 recreates these behaviors. Simple dynamical models at the level of individual agents and an effec-  
 339 tive continuum theory explain our observations and provide a minimal phase diagram that shows  
 340 how the transition from an individually exploratory strategy to an exploitative cooperative solution  
 341 is mediated by the local chemical and mechanical environment. Our study suggested algorithms  
 342 that we then deployed in an engineered system of a swarm of robots that individually follow a min-  
 343 imal set of behavioral rules that mould the environment and are modulated by it. A critical aspect  
 344 of our framework is the role of a malleable environment that serves both as a spatial memory as  
 345 well as a computational platform (using the spatio-temporal photormone field and the corral). Our  
 346 simulations of agent-based models and robotic experiments further suggest that a coarse-grained  
 347 framework linking behavior, communication and a modulated environment is relatively robust to  
 348 failure of and stochasticity in the behavior of individual agents (i.e. variations in initial conditions  
 349 and number of agents), in the communication channels or in the corral geometry, in contrast to  
 350 many engineering approaches that aim to control all agents and optimize costs.

351 Different strategies such as collective excavation, jamming and diffusion then arise as a func-  
 352 tion of the relative strength of the cooperation (representing the ability to follow gradients and  
 353 detect threshold values) and excavation parameters (representing the ability to move material),  
 354 as manifest in a phase diagram, and the emergence of cooperation arises due to the relatively  
 355 slow decay of an environmental signal (the pheromone/antennating/photormone field), coupled  
 356 to a threshold excavation rate. Our approach to functional and purposeful collective behavior  
 357 links many simple brains and bodies with a dynamic environment that modulates behavior, and is  
 358 changed by it. Since the ability to solve complex eco-physiological problems such as collective exca-  
 359 vation is directly correlated with a selective advantage in an evolutionary setting, perhaps collective

360 behavior must always be studied in a functional context.

## 361 Acknowledgments

362 We thank the NSF PHY1606895 (S.G.P., L.M.), Swiss National Science foundation (F.G., grant P400P2-  
363 191115), Ford foundation (J.K.), NSF EFRI 18-30901 (L.M.), NSF 1764269 (L.M.), Kavli Institute for  
364 Bionano Science and Technology (S.M., V.M., L.M.), the Simons Foundation (L.M.) and the Henri  
365 Seydoux Fund (L.M.) for partial financial support.

## 366 References

- 367 **Aguilar J**, Monaenkova D, Linevich V, Savoie W, Dutta B, Kuan HS, Betterton M, Goodisman M, Goldman D.  
368 Collective clog control: Optimizing traffic flow in confined biological and robo-physical excavation. *Science*.  
369 2018; 361(6403):672–677.
- 370 **Alcock J**. *Animal behavior: An evolutionary approach*. Sinauer Associates Sunderland; 2001.
- 371 **Braitenberg V**. *Vehicles: Experiments in synthetic psychology*. MIT press; 1986.
- 372 **Bricard A**, Caussin JB, Desreumaux N, Dauchot O, Bartolo D. Emergence of macroscopic directed motion in  
373 populations of motile colloids. *Nature*. 2013; 503(7474):95–98.
- 374 **Brooks RA**. Intelligence without representation. *Artificial intelligence*. 1991; 47(1-3):139–159.
- 375 **Buhl J**, Deneubourg JL, Grimal A, Theraulaz G. Self-organized digging activity in ant colonies. *Behavioral ecology*  
376 and sociobiology. 2005; 58(1):9–17.
- 377 **Camazine S**, Deneubourg JL, Franks NR, Sneyd J, Theraulaz G, Bonabeau E. *Self-organization in biological sys-*  
378 *tems*. Princeton university press; 2020.
- 379 **Couzin ID**, Krause J, et al. Self-organization and collective behavior in vertebrates. *Advances in the Study of*  
380 *Behavior*. 2003; 32(1):10–1016.
- 381 **Deneubourg JL**, Franks NR. Collective control without explicit coding: the case of communal nest excavation.  
382 *Journal of insect behavior*. 1995; 8(4):417–432.
- 383 **Deneubourg JL**, Lioni A, Detrain C. Dynamics of aggregation and emergence of cooperation. *The Biological*  
384 *Bulletin*. 2002; 202(3):262–267.
- 385 **Elster J**, et al. *Social mechanisms: An analytical approach to social theory*. Cambridge University Press; 1998.
- 386 **Feinerman O**, Pinkoviezky I, Gelblum A, Fonio E, Gov NS. The physics of cooperative transport in groups of  
387 ants. *Nature Physics*. 2018; 14(7):683–693.
- 388 **Garnier S**, Tache F, Combe M, Grimal A, Theraulaz G. Alice in pheromone land: An experimental setup for the  
389 study of ant-like robots. In: *Swarm intelligence symposium IEEE*; 2007. .
- 390 **Gordon DM**. *Ants at work: how an insect society is organized*. Simon and Schuster; 1999.
- 391 **Gordon DM**. Movement, encounter rate, and collective behavior in ant colonies. *Annals of the Entomological*  
392 *Society of America*. 2021; 114(5):541–546.
- 393 **Gordon DM**, Paul RE, Thorpe K. What is the function of encounter patterns in ant colonies? *Animal Behaviour*.  
394 1993; 45(6):1083–1100.
- 395 **Hansen LD**, Klotz JH. *Carpenter ants of the United States and Canada*. Cornell University Press; 2005.
- 396 **Hillen T**, Painter KJ. A user's guide to PDE models for chemotaxis. *Journal of mathematical biology*. 2009;  
397 58(1):183–217.
- 398 **Hölldobler B**, Wilson EO, et al. *The ants*. Harvard University Press; 1990.
- 399 **Hölldobler B**, Wilson EO, et al. *The superorganism: the beauty, elegance, and strangeness of insect societies*.  
400 WW Norton & Company; 2009.
- 401 **Le Goc M**, Kim LH, Parsaei A, Fekete JD, Dragicevic P, Follmer S. Zooids: Building blocks for swarm user in-  
402 terfaces. In: *Proceedings of the 29th Annual Symposium on User Interface Software and Technology*; 2016. p.  
403 97–109.

- 404 **Mataric MJ.** Designing emergent behaviors: From local interactions to collective intelligence. In: *Proceedings*  
405 *of the Second International Conference on Simulation of Adaptive Behavior*; 1993. p. 432–441.
- 406 **Mikheyev A, Tschinkel W.** Nest architecture of the ant *Formica pallidefulva*: structure, costs and rules of  
407 excavation. *Insectes Sociaux*. 2004; 51(1):30–36.
- 408 **Nowak MA.** *Evolutionary dynamics: exploring the equations of life*. Harvard university press; 2006.
- 409 **Ocko SA, Mahadevan L.** Collective thermoregulation in bee clusters. *Journal of The Royal Society Interface*.  
410 2014; 11(91):20131033.
- 411 **Pagliara R, Gordon DM, Leonard NE.** Regulation of harvester ant foraging as a closed-loop excitable system.  
412 *PLoS computational biology*. 2018; 14(12):e1006200.
- 413 **Peleg O, Peters JM, Salcedo MK, Mahadevan L.** Collective mechanical adaptation of honeybee swarms. *Nature*  
414 *Physics*. 2018; 14(12):1193–1198.
- 415 **Pennisi E.** On the Origin of Cooperation. *Science*. 2009; 325(5945):1196–1199.
- 416 **Pereira TD, Tabris N, Li J, Ravindranath S, Papadoyannis ES, Wang ZY, Turner DM, McKenzie-Smith G, Kocher**  
417 **SD, Falkner AL, et al.** SLEAP: multi-animal pose tracking. *bioRxiv*. 2020; .
- 418 **Perna A, Theraulaz G.** When social behaviour is moulded in clay: on growth and form of social insect nests.  
419 *Journal of Experimental Biology*. 2017; 220(1):83–91.
- 420 **Petersen KH, Napp N, Stuart-Smith R, Rus D, Kovac M.** A review of collective robotic construction. *Science*  
421 *Robotics*. 2019; 4(28).
- 422 **Rahwan I, Cebrian M, Obradovich N, Bongard J, Bonnefon JF, Breazeal C, Crandall JW, Christakis NA, Couzin ID,**  
423 **Jackson MO, et al.** Machine behaviour. *Nature*. 2019; 568(7753):477–486.
- 424 **Rasse P, Deneubourg JL.** Dynamics of nest excavation and nest size regulation of *Lasius niger* (Hymenoptera:  
425 *Formicidae*). *Journal of Insect Behavior*. 2001; 14(4):433–449.
- 426 **Reinhard J, Srinivasan MV.** The role of scents in honey bee foraging and recruitment. Food exploitation by  
427 social insects: ecological, behavioral, and theoretical approaches. 2009; 1:165–182.
- 428 **Seeley TD.** *The wisdom of the hive: the social physiology of honey bee colonies*. Harvard University Press;  
429 2009.
- 430 **Simon HA.** *The sciences of the artificial*. 3 ed. MIT press; 1996.
- 431 **Sugawara K, Kazama T, Watanabe T.** Foraging behavior of interacting robots with virtual pheromone. In:  
432 *International Conference on Intelligent Robots and Systems*, vol. 3 IEEE; 2004. .
- 433 **Theraulaz G, Bonabeau E.** Coordination in distributed building. *Science*. 1995; 269(5224):686–688.
- 434 **Toffin E, Di Paolo D, Campo A, Detrain C, Deneubourg JL.** Shape transition during nest digging in ants. *Proceed-*  
435 *ings of the National Academy of Sciences*. 2009; 106(44):18616–18620.
- 436 **Trible W, Olivos-Cisneros L, McKenzie SK, Saragosti J, Chang NC, Matthews BJ, Oxley PR, Kronauer DJ.** Orco mu-  
437 tagenesis causes loss of antennal lobe glomeruli and impaired social behavior in ants. *Cell*. 2017; 170(4):727–  
438 735.
- 439 **Tschinkel WR.** The nest architecture of the Florida harvester ant, *Pogonomyrmex badius*. *Journal of Insect*  
440 *Science*. 2004; 4(1):21.
- 441 **Wang G, Phan TV, Li S, Wombacher M, Qu J, Peng Y, Chen G, Goldman DI, Levin SA, Austin RH, et al.** Emergent  
442 field-driven robot swarm states. *Physical review letters*. 2021; 126(10):108002.
- 443 **Waters CM, Bassler BL.** Quorum sensing: cell-to-cell communication in bacteria. *Annu Rev Cell Dev Biol*. 2005;  
444 21:319–346.
- 445 **Werfel J, Petersen K, Nagpal R.** Designing collective behavior in a termite-inspired robot construction team.  
446 *Science*. 2014; 343(6172):754–758.

## Videos

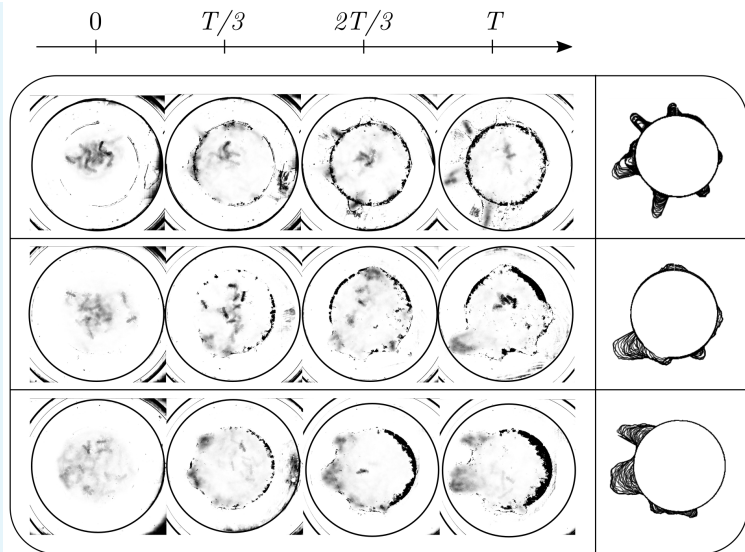
We have 4 supplementary videos which can be viewed using this [link](#).

1. Video 1 - Ant experiments: (i) Single ant: We confined 1 ant (major, media and minor individually) and capture their dynamics to see if they are capable of tunneling on their own; (ii) Multiple castes assemblage: We confined 12 ants, 4 for each of major, minor and media castes, and capture the dynamics of excavation as they tunnel through the boundary; (iii) Major ant collective excavation: We confined 12 major ants and capture the dynamics of excavation as they tunnel through the boundary.
2. Video 2 - Successful tunneling in RAnts: (i) Dynamics of excavation by RAnts as they cooperatively tunnel through the corral for  $C = 1$  and without cooperation,  $C = 0$ ; (ii) Jammed phase: When the pick-and-place in RAnts is deactivated (corresponding to  $E = 0$ ), they get jammed for  $C = 1$ ; Diffused phase: When the pick-and-place in RAnts is deactivated and the RAnts do not follow the antennating field (corresponding to  $C = 0$ ), they diffuse around.
3. Video 3 - Dynamics of excavation from agent-based simulation for different number of agents ( $n = 1, 5, 10, 22, 100$ ) in the corral for parameters in tab. 1. We see successful escape as well as trapped dynamics as highlighted in **Figure 3(d)**.
4. Video 4 - Summary video showing the results from ant experiments, theoretical model and robot experiments.

## Ant experiments

### Experimental setup - handling ants

We collected two queen-right mature colonies of *Camponotus pennsylvanicus*, established in logs of fallen trees, from the Middlesex Fells Reserve (42.45°N, 71.11°W) in August 2019. Each mature colony consists of three morphologically distinct castes of worker ants: major, media and minor, with an average body length of 7 mm, 5 mm for media, and 4 mm respectively. We placed the collected wooden logs housing those colonies in two separate plastic "home" boxes. We coated the inner wall of each home box with ant-slip Fluon to prevent the ants from escaping the home box. Each home box was connected to a foraging box by a tube through which ants travelled to and fro. We kept the whole set up in the laboratory with a 12 hour light-dark cycle, 30°C temperature and 50-70% relative humidity. Before we moved to the next phase of the experiment, i.e. the data collection, we waited for the ants to resume foraging and excavation of woods (for expanding their galleries) inside their home wooden log; this took 3-5 days after the relocation.



481  
482  
483  
485

**Appendix 1 Figure 1.** Dynamics of ant density field,  $\rho_a(\mathbf{x}, t)$  (in units of  $\#/mm^2$ ) obtained by averaging the ant location and the boundary shape  $R(\phi)$  when 4 ants each of major, media and minor types are confined inside the agar ring for different trials.

486  
487  
488  
489  
490  
491

About 10 minutes prior to the experiments, we collected ants engaged in wood excavation from the surface of the nest log. We used insect aspirators for collecting the ants. Once we collected all ants needed for the experiment, we subjected the ants to Carbon dioxide anaesthesia for 1 minute. Next, we placed the anaesthetised ants in the agarose well in the experimental arena; we placed each ant at least 1 cm away from any other ant. Ants regained their activity in the next 5-10 minutes.

492

### Experimental setup - confinement

493  
494  
495  
496  
497  
498  
499  
500  
501  
502  
503  
504  
505  
506

For the next phase of the experiment, we needed to confine the ants in an excavatable enclosure. This is the corral that the ants need to bite through to free themselves. We used a ring-like confinement made of agarose gel, with a height of 10 mm, an inner radius of 35 mm and outer radius of 55 mm, making the ring 20 mm thick. To make a precise shape of the ring repeatedly, we custom-built a casting mold made of acrylic plastic. We started preparing for the Agar ring before we collected the ants. For making the ring, first, we thoroughly mixed 3 gm of Agar powder in 100 ml of tap water. We then warmed the solution in a microwave oven until the solution started bubbling and appeared clear. Next, we poured the solution in the plastic mold, and kept it in 30°C temperature for 25 minutes; the agarose gel solidified and become opaque during this time. Once the agarose turned solid, we placed the ring on top of plastic sheet in the arena. Next, we placed the ants inside the ring and put a petri dish lid on top of the agarose ring. Thus, we confined the ants - with a solid plastic floor and ceiling, and an excavatable agarose gel wall. A schematic of the set-up is shown in *Figure 1(b)*.

507

### Experimental setup - arena and video recording

508  
509  
510  
511  
512

The arena consists of a piece of white 3 mm thick plastic sheet as the substratum, illuminated with infrared back-light, and surrounded by a 1.5 cm high plastic wall coated with Fluon ant-slip. We placed a Point Grey (FLIR) Grasshopper3 GS3-U3-41C6NIR camera, fitted with a 65 mm macro lens, on top of the arena to capture the view of the whole ring. The camera recorded the videos with 30 fps recording speed and 1024x1024 pixels resolution.

513  
514  
515  
516  
517  
518  
519  
520  
521  
522  
523  
524  
525  
526  
527  
528  
529  
  
530  
531  
532  
533  
534  
535  
536  
537  
538  
539  
540  
541  
542  
  
543  
544  
545  
546  
547  
548  
549

### Markerless tracking

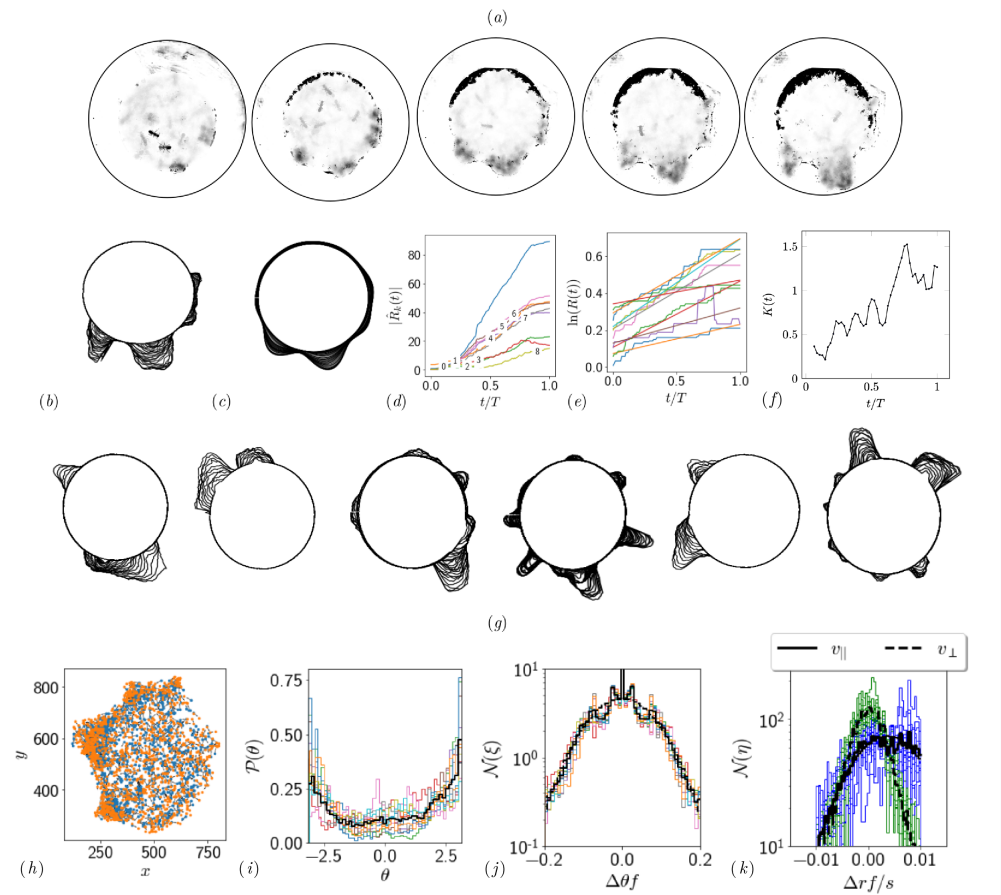
Leveraging an open source, deep-learning based pose estimator package SLEAP (*Pereira et al., 2020*), we track 3 body parts in each ant - head, thorax, and abdomen (gaster). Sample results obtained from this tracking is shown in SI *Figure 2(e)* and in *(f - h)* we quantify the noise statistics of ant motion and its orientation using the tracking data. Ants initially move randomly in the confinement and one of the ants starts the excavation process after which several ants start excavating cooperatively at the same location. When the tunneling happens, all the ants are orientated along the tunnel. We see this through the progression of the orientation distribution of ants  $\mathcal{P}(\theta, t)$  in SI *Figure 2(j)*. To characterize the localization in ant orientation as the excavation proceeds, we use a von-Mises distribution (the analog of a Gaussian distribution for a periodic variable, given by  $\mathcal{P}(\theta, t; \mu(t), K(t)) = \exp[K \cos(\theta - \mu)] / 2\pi I_0(K)$ ) of the ants (where  $\mu$  is the mean local orientation associated with location of tunnel along the boundary). In SI *Figure 2(k)*, we see that over time,  $K(t)$  increases, i.e. the variance decreases. During the excavation process, ants bite through the corral, carry the debris from the excavation site and drop it in the interior of the confinement. This happens over and over again until all the ants excavate out. We see this captured in the oscillations of the location of ants as shown in SI *Figure 2(i)*.

### Average dynamics

We have a total of 7 sets of experiments with four sets of experiments with a collective of 12 majors ants and 3 sets of experiments with a mixture of 4 major, 4 media and 4 minor ants. Using the recorded video of the ant excavation dynamics, we threshold the intensity to extract only the ant boundary and average the ant dynamics over 250 secs. This gives us a density field of ants representing the locations where the ants have been and the amount of time they spend. We found in our experiments that each ant bites the corral, picks the bitten piece and transports it into the interior of the confinement. This process takes approximately 60 secs (see SI *Figure 2(i)*) and we would like to average the ant dynamics over several 'turn over' time-scales. We chose 250 secs and the obtained density field is shown in SI *Figure 2*. We perform this averaging for the experiments with all major ants as well as the mixture of different castes. In all the experiments, an ant density front propagates through the corral as they excavate and gradually tunnel through.

### Boundary tracking

From the recorded videos, we also track the locations in which the ants excavate for creating the tunnel. For that, we used a custom image processing Matlab script. First, we created a mask superimposing on the area encircled by the inner ring of the corral; we colored the mask with a shade different from the corral. When ants excavated the corral, the Matlab script could detect the difference in the shade/color of the excavated area. Using this contrast, we track the continuously changing boundary.



550

551

552

553

554

555

556

557

558

559

560

561

562

563

564

565

566

567

568

569

570

**Appendix 1 Figure 2.** (a, b) Shape of the boundary tunnel during the tunneling process and the approximate representation of the shape using first 9 Fourier modes. (c) Evolution of the magnitude of the first 9 Fourier modes of the boundary:  $R(\phi, t) = \sum_k \hat{R}(k, t) e^{ik\phi}$ . (d) Evolution of boundary location,  $R(t)$  at different  $\phi$  values and the excavation rate. (e) Collage of boundary evolution showing tunnel formation in six experiments. (f)  $K(t)$  is the von Mises parameter highlighting strength of focus in ant orientation thorough a fit to the  $\mathcal{P}(\theta)$  obtained by a curve fit to the distribution. (g) Image showing evolution of the boundary as the excavation process happens for different experimental trials. (h) Location of center of ants with orientation during the excavation process. (i) Average orientation distribution  $\mathcal{P}(\theta)$  of all the ants showing hints of localization which is evident when plotted over time. (j) Noise statistics of ant velocity along the body axis,  $v_{\parallel}$  and in the normal direction,  $v_{\perp}$ . Dashed lines again are Gaussian fit to the data. Ants have zero mean velocity normal to its axis. (k) Noise statistics of orientation with peak close to 0 because of resting of the ants which otherwise follows a Gaussian which is the dashed line.

This is shown as a super-imposed image on the right side of SI **Figure 2** where  $R(\phi, t)$  is the radius of the ring as a function of the polar angle  $\phi$ . Tunnels are locations along  $\phi$  which see increase in the radius. We quantify this by plotting  $R(t)$  in SI **Figure 2**(d). We also quantify the number of tunnels by decomposing the shape into different Fourier modes as detailed in the caption.

### Agent-based model of cooperative task execution

The results shown in figure 3 are based on a numerical simulation where discrete agents operate in a continuum scalar communication field, subject to Equation (1) - (3). Some additional behavioral rules have to be defined to model the interaction of agents with the substrate. We realize the substrate by discrete obstacles arranged in a circular ring. Agents will attach to an obstacle if they are within the detection range,  $l_d$ , and if the measured communication field value is above the threshold, i.e.  $c \geq c_{hi}^*$ . The agent will then reverse its direction of motion, by changing the sign of  $G$  in Equation (2). This results in a gradient descent behavior and the attached obstacle will be detached once the measured communication field value satisfies  $c < c_{lo}^*$ . After detachment, the sign of  $G$  is changed again. If agents encounter other agents or obstacles within the detection radius but  $c < c^*$ , the agents will avoid the obstacle by turning randomly.

There are a few tuned behaviors we implemented to allow scaling the simulation to larger numbers of agents while maintaining the tunneling behavior. First, the gradient  $\nabla_{\perp} c$  in Equation (2) is passed through a  $\tanh(\cdot)$  function to limit the turning rate of the agents. Second, the noise term in Equation (2) was set to zero for this simulation and the only source of randomness are the random turns during obstacle avoidance. Third, agents pause for  $t_{p1}$  when they encounter an obstacle and for  $t_{p2}$  when picking up an obstacle. This helps disrupting potential "pheromone traps" to be formed where agents are bound to a region of space due to a high field concentration.

The simulation parameters are described in the following table. All parameters are non-dimensionalized by the corral size  $L$  and the base speed of the agents,  $v_0$ .

Parameter	Description	Value
$n_r$	Number of agents	1-100
$n_o$	Number of substrate elements	300
$n_l$	Number of corral layers	3
$T$	Maximum simulation time	66
$k_+$	Communication field production rate	97.5
$k_-$	Communication field decay rate	0.75
$D_a$	Communication field diffusivity	$4.2 \times 10^{-3}$
$c_{hi}^*$	Excavation threshold	$\frac{1}{2} \frac{k_+}{k_-}$
$c_{lo}^*$	Detachment threshold	0.11
$\sigma_g^2$	Agent field production width (variance)	$2.8 \times 10^{-3}$
$l_d$	Agent obstacle detection range	0.03
$t_{p1}$	Pause after obstacle detection	0.07
$l_{p2}$	Pause after substrate attachment	0.27
$G$	Rotational gain	0.135

Appendix 2 Table 1. Parameters of agent-based simulation.

597

## Continuum model of cooperative task execution

The dimensional equations for the ant-density  $\rho_a(\mathbf{x}, t)$ , antennating field  $c(\mathbf{x}, t)$  and the corral  $\rho_s(\mathbf{x}, t)$  are given by,

$$\partial_t \rho_a + \nabla \cdot (\mathbf{u}_a \rho_a) = \nabla \cdot (D_a \nabla \rho_a - \chi \rho_a \nabla c), \quad (12)$$

598

$$\partial_t c = D_c \nabla^2 c + k_+ \rho_a - k_- c, \quad (13)$$

599

600

$$\partial_t \rho_s = -\frac{1}{4} k_s \rho_s (1 + \tanh[\alpha_c (c - c^*)])$$

601

$$(1 + \tanh[\alpha_c (\rho_a - \rho_a^*)]), \quad (14)$$

602

603

604

605

606

607

608

609

where velocity of the collective is  $\mathbf{u}_a = v_o(1 - \rho_s/\rho_o)\hat{\mathbf{p}}$ , capturing the reduction in velocity as the ant collides with the corral. We approximate the Heaviside function,  $\Theta(x)$  here using the hyperbolic function  $[1 + \tanh(x)]/2$ . In the coarse-grained picture describing the collective tunneling seen in experiments the relevant variables (shown schematically in **Figure 4**) are the density of ants,  $\rho_a$ ; their velocity,  $\mathbf{u}_a$ ; amplitude of the antennating field,  $c$ ; the density of corral,  $\rho_s$ . Here we discuss the limits of phase-space that are not described in the main text i.e. when  $E \neq 0$  and also the simulation details.

Time-scale	Process
$\tau_a \sim l^2/D_a$	Ant diffusion
$\tau_v \sim l/v_o$	Ant collective migration
$\tau_x \sim l^2/(\chi c_o)$	Taxis due to antennating field gradient
$\tau_+ \sim c_o/(k_+ \rho_o)$	Antennating field production
$\tau_c \sim l^2/D_c$	Antennation field diffusion
$\tau_- \sim 1/k_-$	Antennating field decay
$\tau_s \sim 1/k_s$	Corral excavation
Length-scale	Process
$L$	Corral width
$l_a$	Initial width of ant density
$D_a/v_o$	Ant density advection-diffusion
$(D_c/k_-)^{1/2}$	Antennating field diffusion-decay

611

612

**Appendix 2 Table 2.** Time-scales and length-scales associated with different processes in the model in **Equation 12- Equation 14**.

614

615

616

617

618

619

620

621

622

623

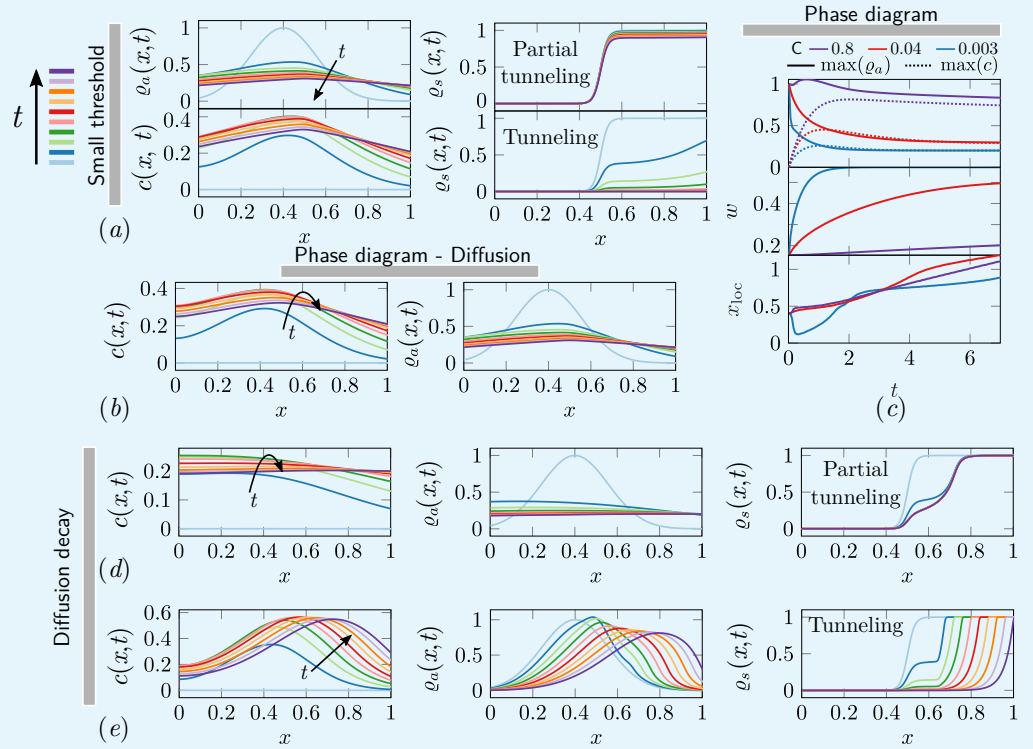
### Limits of phase-space when $E \neq 0$

Different phases of task execution/failure arise when the excavation parameter  $E$  and the cooperation parameter  $C$  are varied. In the cooperation dominated phase if the excavation rate of the agents is small, they get jammed and the analysis in the previous section holds true. When the cooperation among the agents is low, we have  $C \ll 1$  which results in diffusion dominated regime. Based on the strength of the excavation parameter  $E$ , the corral can be partially tunneled or just diffuse. Since we assume that the relevant length scale is of the same order as the width of the corral,  $L \sim l$ , our analysis reduces to different phases based on whether  $E \gg 1$  (where we get partial-tunneling) or  $E \ll 1$  (we get diffusion). Based on this we get partial tunneling or diffused phase as listed in **Table 3**.

In **Figure 1** we show results from 1-D simulations highlighting the effect of different terms we have discussed from **Equation 4-Equation 5** corresponding to different parts of the phase space of cooperative excavation. In the ant density diffusion dominated regime, i.e.  $C \ll 1, E \ll 1$ , shown in **Figure 1(b)**, there is little cooperation; rapid diffusion with slow excavation results in no tunneling. As we have seen in **Figure 4(b, c)**, tunneling and partial tunneling are inferred through the ultimate state of the corral and the ant-density. In

626  
627  
628  
629  
630  
631  
632  
633  
634  
635  
636  
637  
638  
639

SI **Figure 1(d, e)** we show how the relative rate of the antennating field diffusion compared to decay, i.e.  $D_c \sim \mathcal{O}(1)$  leads to either tunneling or partial tunneling as we vary the cooperation parameter  $C$ . Decreasing  $C$  causes the maximum of  $\rho_a(x, t)$ ,  $c(x, t)$  to go down (ref SI **Figure 1(c)**), and the width of the initial ant density field increases. Increasing  $C$  leads to successful tunneling driven by the propagation of the location of maximum ant density  $x_{loc}$  due to excavation of the corral. Furthermore, we see that the ants can be jammed either because the antennating field diffusion dominates, i.e.  $D_c \sim \hat{k}_{\pm} \gg 1$ , or because of the same field decays rapidly, i.e.  $\hat{k}_{\pm} \sim \mathcal{O}(1)$ ,  $D_c \ll 1$ . In both these cases however cooperation is what drives the aggregation. Lastly, we see that in order to achieve partial tunneling there are several routes depending upon the relative magnitudes of  $\{C, E, V, \hat{k}_{\pm}, D_c\}$  listed in **Table 3**.



	Phase	$v_o$	$\chi$	$D_a$	$k_+$	$k_-$	$D_c$	$k_s$
Small threshold	Tunneling	0.1	0	0.1	-	-	-	2.5
	Partial-tunneling	0.1	0	0.1	-	-	-	0.03
Phase diagram	Tunneling	0.1	$5 \times 10^{-3}$	$5 \times 10^{-3}$	1.5	1.5	$5 \times 10^{-3}$	2.5
	Partial-tunneling	0.1	$5 \times 10^{-3}$	$5 \times 10^{-1}$	1.5	1.5	$5 \times 10^{-3}$	2.5
	Partial-tunneling II	0.1	$5 \times 10^{-3}$	$5 \times 10^{-2}$	1.5	1.5	$5 \times 10^{-3}$	2.5
	Diffusion	0.1	$5 \times 10^{-3}$	0.1	1.5	1.5	$5 \times 10^{-3}$	0.001
Diffusion decay	Tunneling	0.1	$5 \times 10^{-3}$	$5 \times 10^{-3}$	1.5	1.5	$5 \times 10^{-2}$	2.5
	Partial-tunneling	0.1	$5 \times 10^{-3}$	$5 \times 10^{-1}$	1.5	1.5	$5 \times 10^{-2}$	2.5
(f) 2D	Tunneling	0.1	$5 \times 10^{-3}$	$5 \times 10^{-3}$	1.5	1.5	$5 \times 10^{-3}$	1.0

**Appendix 2 Figure 1.** The ant density field  $\rho_a(x, t)$ , antennating field  $c(x, t)$  and corral density  $\rho_s(x, t)$  for various scenarios of interest in the phase-space: (a) partial tunneling and tunneling when the threshold for excavation is small i.e.  $\rho_a^* = c^* = 0.01$ , we see homogeneous excavation and can get tunneling and partial tunneling; (b) when we are in the diffusive phase where ant density diffusion dominates,  $C = 0.02$  and the excavation rate is very small,  $E = 6 \times 10^{-4}$ ; (d, e) partial tunneling and tunneling when the length scale due to antennating field diffusion and decay is of the same order as the initial ant density i.e.  $l_a \sim (D_a/k_-)^{1/2}$ . (c) Evolution of maximum value of  $\rho_a, c$  for 3 different  $C$  and fixed  $E = 1.44$ . (f) Table with parameters used in simulations corresponding to different titles shown in gray bar in (a – e).

640  
641  
642  
643  
644  
645  
646  
647  
648  
649  
650

651

C	E	V	$\hat{k}_{\pm}$	$D_c$	Phase
$\gg 1$	$\gg 1$	$\gg 1$	$\mathcal{O}(1)$	$\ll 1$	Tunneling
$\gg 1$	$\gg 1$	$\gg 1$	$\ll 1$	$\mathcal{O}(1)$	Tunneling
$\ll 1$	$\gg 1$	$\gg 1$	$\mathcal{O}(1)$	$\ll 1$	Partial-Tunneling
$\ll 1$	$\gg 1$	$\gg 1$	$\ll 1$	$\mathcal{O}(1)$	Partial-Tunneling
$\gg 1$	$\ll 1$	-	$\mathcal{O}(1)$	$\ll 1$	Jammed
$\gg 1$	$\ll 1$	-	$\ll 1$	$\mathcal{O}(1)$	Jammed
$\ll 1$	$\ll 1$	-	-	-	Diffused

653

**Appendix 2 Table 3.** Different phases in different limits of phase-space of parameters in the model.

654

### Simulation details

655

656

657

658

659

660

661

662

663

664

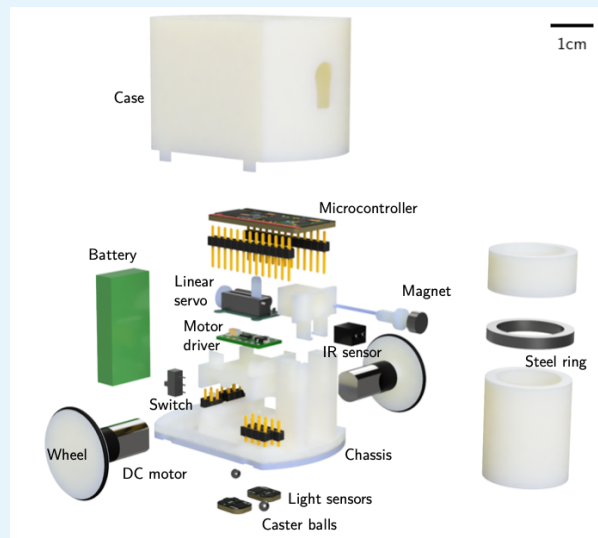
665

All the simulations shown in the main text as well the ones above were performed using commercial software COMSOL<sup>TM</sup>, in their general form Partial Differential Equations solver. We choose a very fine resolution with maximum mesh size of 0.005 in a domain of size 2 units in 1D simulations and maximum mesh size of 0.25 in a circular domain of radius 5 units in 2D. The initial condition for the ant density,  $\rho_a(r, 0)$  is  $\exp(-(r - r_o)^2/2l_a^2)$  where  $r_o = 0.4$ ,  $l_a = 0.16$  and the density of the corral  $\rho_s(r, 0)$  is chosen to be  $[1 + \tanh(\alpha(r - 2.5))]/2$  where  $\alpha = 30$ . We set the parameter  $\alpha_c = 50$  in 1D,  $\alpha_c = 10$  in 2D while  $\rho^* = 0.3$ ,  $c^* = 0.01$ . The other parameters used in the simulations in **Figure 4**, **SI Figure 1** and **Figure 5(a - e)** are listed in **(f)**. In the 2D simulations in **Figure 5** we assume a spatio-temporally varying self-propulsive velocity field of the form,  $\mathbf{u}_a = v_o \{\exp(-y^2/2\sigma^2), \exp(-t/\tau)(1 - \exp(-(x - x_o)^2/2\sigma^2))\}$ ,  $v_o = 0.1$ ,  $x_o = 0.2$ ,  $\sigma^2 = 0.75$ ,  $\tau = 10$ .

## Robot Ants

### RAnt design

RAnts were designed to accommodate the essential electronic and electromechanical parts required for locomotion, picking and placing, and sensing. An exploded view is shown in **Figure 1**. RAnts are powered with a rechargeable 3.7V battery with 400mAh (Pkc cell LIPO 801735) and are coordinated with a microcontroller (Adafruit ItsyBitsy M0 Express). The RAnt's wheels have a diameter of 25mm and are directly driven with two brushed DC motors with a planetary gearbox rated at 85 RPM at 3.7V. Rubber o-rings are attached to the wheels to increase traction. A dual motor controller (Pololu DRV8835 Dual Motor Driver Carrier) sets the desired output speed of the motors given a PWM signal from the microcontroller. The mechanism to pick up wall elements was realized using a permanent magnet that is retractable inside the RAnt. A linear servo motor (Spektrum SPMSA2005) moves a permanent magnet inside a guide such that, when fully extended, the magnet attracts ferromagnetic materials and when retracted, the magnetic force is small enough to drop any previously attached objects.



**Appendix 3 Figure 1.** Exploded view of a RAnt and a wall element.

The objects to be picked up are cylindrical wall elements of dimension 22mm×40mm made of polyvinyl chloride (PVC) tubes which have a ferromagnetic ring of 3mm thickness embedded in them. The ring was 3D printed using polylactic acid (PLA) mixed with steel powder (colorFabb SteelFill) and was sandwiched between two PVC tubes. If the RAnt is sufficiently close ( $\approx 3$ mm) to a wall element with an engaged magnet, the ring in the wall element is attracted to the magnet and the wall element is slightly lifted from the ground ( $\approx 1$ mm) for transportation due to the elevated position of the magnet relative to the ferromagnetic ring. RAnts have two

types of sensors; two light sensors (Adafruit ALS-PT19) located at the bottom left and right of the RAnt (relative to the direction of travel) and an infrared (IR) distance sensor (Everlight ITR20001 opto interrupter) capable of detecting objects within 3cm in front of the RAnt. The chassis of the RAnt is 3D printed using acrylic styrene acrylonitrile (ASA) and supports all the internal components. The wheels of the RAnts were printed with the same material. Due to the design of the wheel arrangement, which was inspired by the zoid robots (**Le Goc et al., 2016**), we require two small steel caster balls of 3mm in diameter that help stabilize the RAnt. The steel balls can be pressed into the bottom of the 3D printed chassis. A 3D printed case made of ASA encloses all internal components of the RAnts, except for a small switch to power the RAnt on or off. A small blue sticker of 6mm in diameter was placed on the center top of the case and is used for tracking of the RAnt's position with the webcam

715  
716  
717  
718  
719  
720  
721  
722  
723  
724  
725  
726  
727  
728  
729  
730  
731  
732  
733  
734  
735  
736  
737  
738  
739  
740  
741  
742  
743  
744  
745  
746  
747  
748  
749  
750  
751  
752  
753  
754  
755  
756  
757  
758  
759  
760  
761  
762  
763  
764  
765  
766

mounted above the arena.

### RAnt programming

The RAnt behavior is coordinated by the microcontroller which we programmed according to the pseudocode shown in Algorithm 1. The program is initialized with a variable  $d$  that encodes the direction of travel (1 for forward, -1 for backward), the cooperation parameter  $C \in [0, 1]$ , the RAnt's base speed  $v_b$ , and the light intensity threshold  $c^*$ . This threshold was set at 50% of the maximal light intensity that can be generated by the photormone field multiplied by the cooperation parameter, i.e.  $c^* = 0.5 \times c_{max} \times C$ .

After initialization, the program enters a while loop which is running until the RAnt is switched off or the battery voltage drops below 3.5V. The loop starts with setting the heading of the RAnt, which effectively sets the turning rate. The turning rate is a function of the cooperation parameter and a stochastic process  $W$  (Wiener process) which is integrated in the microprocessor. The turning rate follows the equation

$$\Omega = Cd \frac{c_L - c_R}{c_{max}} + (1 - C) b \sin(\pi W) \quad (15)$$

with  $c_L$  and  $c_R$  the photormone intensity measured in the left and right light sensors, respectively,  $c_{max}$  is the maximal photormone intensity measurable by the sensors, and  $b = 0.3$  is a fixed amplitude. Using a sine function we map the stochastic process  $W$  to the range  $[-1, 1]$  to avoid getting stuck in constant rotation for large excursions of  $W$ . The first term in **Equation 15** corresponds to phototaxis using the projected photormone and the second term to a random walk. We can tune the influence of either terms with the cooperation parameter  $C$  from pure phototaxis at  $C = 1$  to a random walk at  $C = 0$ . The turning rate is used to define the rotation speed of each wheel. One wheel is always turning at a base rate  $\omega_1 = \omega_b = v_b/R$  (with  $R$  the wheel's radius) and the other wheel at

$$\omega_2 = \omega_b (1 - 2\|\Omega\|). \quad (16)$$

The assignment of  $\omega_1$  and  $\omega_2$  to the left and right wheel is flipped according to the sign of  $\Omega$ . With this definition, at a value of  $\Omega = \pm 1$  a RAnt turns on the spot without any translation and at  $\Omega = 0$  the RAnt moves on a straight path without rotation.

After the heading was defined and the turning rates sent to the motor driver, the distance sensor is checked for any obstacles that are present up to 3cm in front of the RAnt. At the same time, the light sensors are checked and compared to the threshold value  $c^*$ . If an object is detected and the photormone value exceeds  $c^*$ , the RAnt performs a fetching manoeuvre that consists of engaging the magnet with probability  $E$ , moving forward for a second with half the base speed  $v_b$  then move backwards for the same amount of time. After the fetching manoeuvre, the direction parameter is inverted, i.e.  $d = -1$ . If an object is picked up with the magnet after the fetching manoeuvre, the distance sensor will report a detected object as long as it is attached to the magnet. Since  $d = -1$ , the RAnt will perform the same type of gradient driven locomotion described in **Equation 15** and **Equation 16** but the sign of the signal sent to the motor driver will be inverted, resulting in a reverse motion of the RAnt. If an object is detected, but the photormone concentration in both sensors is lower than  $c^*$ , an avoidance manoeuvre is performed which consists of a random rotation in place in any direction with the intent to turn away from the detected obstacle.

The next if-statement checks again if an obstacle is detected, but without the condition that the direction parameter is equal to one. If no obstacle is detected, the direction parameter  $d$  is set to one and the magnet is disengaged.

---

**Algorithm 1:** RAnt behavioral algorithm

---

**Result:** Cooperative escape in Robot Ants

```
d = 1;
C ∈ [0, 1];
c* = 0.5 × cmax × C;
while true do
  set heading;
  if object detected & d = 1 then
    if c > c* then
      engage magnet with probability E;
      fetch object;
      d = −1;
    else
      turn away from object;
    end
  end
  if no object detected then
    d = 1;
    disengage magnet;
  end
  if d = −1 and P < kC then
    disengage magnet;
    turn away from object;
    d = 1;
  end
end
```

---

767

768

769

770

771

772

773

774

775

776

This guarantees that if a fetching manoeuvre is performed but the wall element was not picked up or the object was another RAnt, the RAnt goes back to moving forward.

The last if-statement checks whether the RAnt is in the reverse mode  $d = -1$  and if the photormone concentration dropped below the threshold  $c^*$ . If both statements are true, the magnet is disengaged, dropping any potentially picked up wall elements, and the direction parameter is set back to  $d = 1$ . In order to avoid the RAnt from picking up the just dropped element, it performs a random rotation in place in any direction before going back to the start of the main loop.

### Experimental set-up

The photormone was projected with an Epson EX9200 projector onto an acrylic sheet with a translucent top, which served as the surface on which the RAnts are operating. The projector uses three-chip digital light processing (DLP) which is required for the light sensors in the RAnts to pick up the photormone field. Tests with single-chip DLP projectors generated large noise in the light sensors and phototaxis was not possible. The dynamics of the photormone field is a function of the RAnt's positions and is given by

$$\partial_t c = D\nabla^2 c - k_M c + k_P \sum_{i=1}^n \mathcal{N}(\mathbf{r}_i, \Sigma) \quad (17)$$

with  $c = c(\mathbf{x}, t)$  the photormone concentration at position  $\mathbf{x} = [x, y]$  and time  $t$ ,  $D = 10^{-5} \text{ m}^2 \text{ s}^{-1}$  the diffusion coefficient,  $k_M = 1 \text{ s}^{-1}$  the decay rate,  $k_P = 6.5 \text{ s}^{-1}$  the photormone production rate,  $n$  the number of RAnts detected in the arena,  $\mathcal{N}(\mathbf{r}_i, \Sigma)$  a bivariate normal distribution with the position of the  $i$ th RAnt  $\mathbf{r}_i$  as the mean and covariance  $\Sigma$  with diagonal entries  $\sigma^2 = 10^{-4} \text{ m}^2$ . The position of the RAnts are used as the centers of sources of photormone. If a RAnt is not moving, photormone is built up with rate  $k_P$  at that location over time and diffuses out. When the RAnt moves to a new location, the built up photormone decays with rate  $k_M$ . The reasoning for the parameter choices is as follows. The parameters were tuned

790  
791  
792  
793  
794  
795  
796  
797  
798  
799  
800  
801  
802  
803  
804  
805  
806  
807  
808  
809  
810  
811  
812  
813  
814  
815  
816  
817  
818  
819  
820  
821  
822  
823  
824  
825  
826  
827  
828  
829  
830  
831  
832  
833  
834  
835  
836  
837  
838  
839

to allow for a RAnt located at one position for one second to leave a detectable trace for 5 seconds. During that time, another RAnt moving at base speed  $v_b \approx 5\text{cm/s}$  can travel half the diameter of the arena. The diffusion length over the decay time scale is  $\approx 3\text{mm}$  which may appear small, however, RAnts are not always moving at base speed but often located in a particular location for multiple seconds to even minutes. The parameter choice described here has shown to neither saturate the domain with photormone nor be too volatile, but allowing the photormone to act as a spatiotemporal memory for the RAnts over the course of an experiment.

The positions of the RAnts are tracked with a webcam mounted above the arena and evaluated in Matlab. Blue markers are attached on the centroid of the case's upper surface which allow to use a simple blob detection to identify the pixel position of the RAnts. The photormone concentration is then dynamically updated in the same Matlab script and displayed on the RAnt arena with the projector. The tracking and integration of the photormone field is executed in real time which restricted the update rate of the projected field to 8 Hz on average. The low refresh rate did not have any noticeable consequences for the conducted experiments but might have affected results for RAnts with a much larger base speed and more volatile photormone dynamics.

The set-up of the enclosure for the RAnts consisted of approximately 200 wall elements arranged in three concentric circles where the outermost circle had a diameter of 50 cm. The outermost circle was prevented from being pushed outward from their initial position by a thin plastic ring that was attached to the base of the arena. The plastic ring was thick enough to prevent wall elements from leaving the confinement, but thin enough for RAnts to roll over it to escape the arena. For every experiment we randomly placed the rants in the arena and waited for the first RAnt to excavate out or the time limit of 15 minutes to be reached. At that point, data was stored and the experiment ended. Most experiments required no intervention, but in case of an empty battery of a RAnt or any unexpected critical failure during the experiments, we had two RAnts standing by to replace the defective RAnt. Since all RAnts are identical and the main memory is communicated through the environment and the photormone concentration, a switch has no further statistical consequences on the outcome of the experiments. There was no leader and no dedicated roles, which makes every RAnt replaceable.

We conducted experiments for five cooperation parameters  $C = \{0, 0.25, 0.5, 0.75, 1\}$  at fixed excavation rate  $E = 1$  and repeated experiments five times for each parameter. Every RAnt's software was updated before a new set of five experiments with the same cooperation parameter was conducted. For every experiment, we stored the webcam data and time stamps. The video frames were post-processed and locations of all RAnts and wall elements were stored as a function of time.

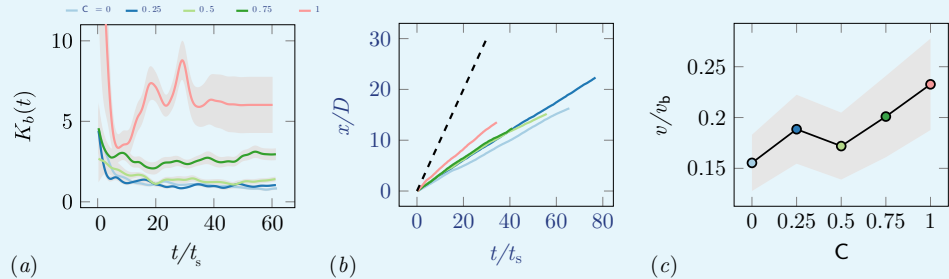
For the phase diagram experiments we used the previous data for cooperation parameters  $C = 0$  and  $C = 1$  for partial tunneling and tunneling, respectively. To induce jamming behavior and diffusion behavior the excavation rate had to be changed in the internal programming of the RAnts. By setting the excavation rate  $E = 0$  the probability of the magnet engaging vanished which led to jamming for high cooperation parameters, and diffusion for low cooperation parameters. We only collected data for two trials of a few minutes each in the diffusion and jamming case as tunneling cannot be initiated with disengaged magnets which reduces the timescales over which the behavior occurs.

### Cooperation parameter

We explored the effect of cooperation parameters on the excavation time and excavation performance as stated in the main text. Five cooperation parameters, i.e.  $C = \{0, 0.25, 0.5, 0.75, 1\}$ , were selected each of which was tested in five RAnt experiments with five RAnts. SI **Figure 3**

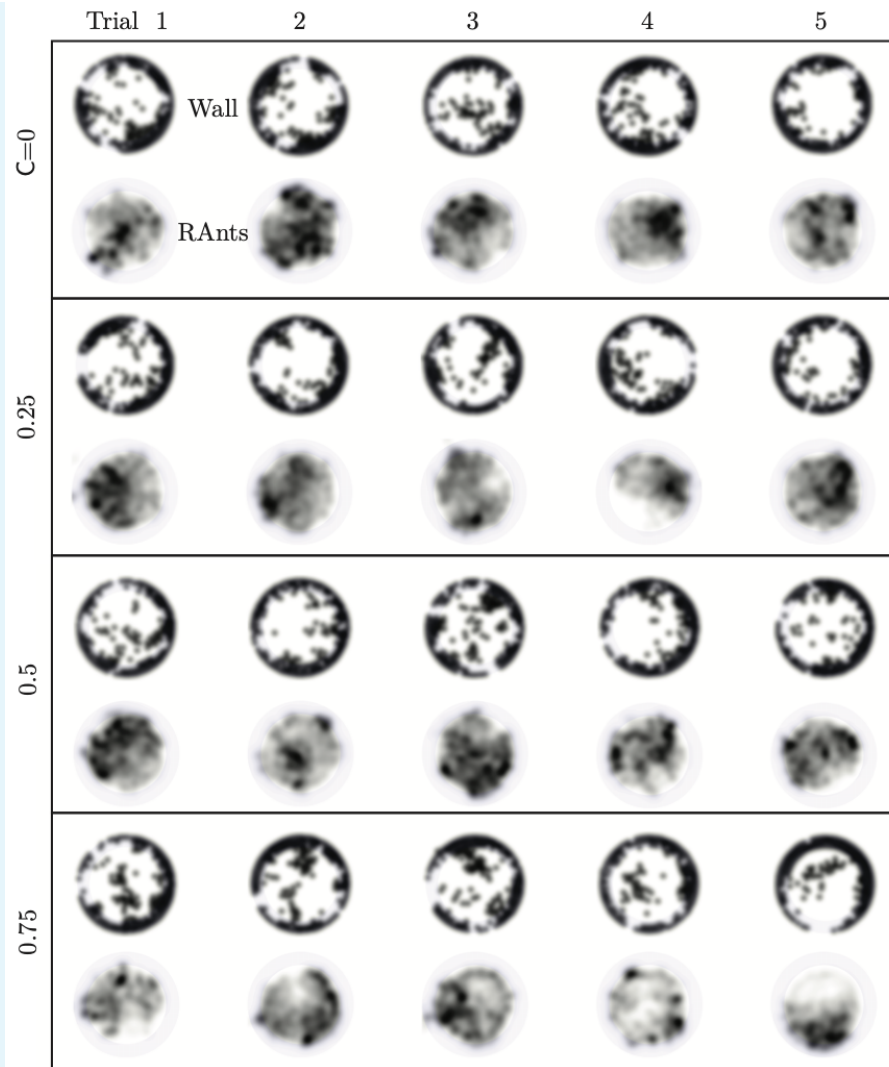
shows the final wall element distribution and the RAnt density averaged over the whole trial for all the conducted 25 experiments.

From the final wall element distribution one can deduce the degree of focus during the tunneling effort. For low cooperation parameters the initial three layers are excavated at multiple excavation sites. As the cooperation parameter increases, less excavation sites are visible and at  $C = 1$  there is in general only one large excavation site.



**Appendix 3 Figure 2.** (a) Von Mises concentration parameter,  $K_b$ , of the angular position of the excavated boundary elements as a function of time for different cooperation parameters and averaged over 5 experiments per cooperation parameter. (b) Total travelled distance of RAnts for different cooperation parameters. The travelled distance  $x$  is scaled by the size of the arena  $D$ . The dashed line shows the travelled distance of a RAnt moving at base speed  $v_b$  constantly. (c) RAnts' averaged speed  $v$  normalized by  $v_b = D/t_s$  for different cooperation parameters  $C$ .

While the final wall distribution shows only a snapshot in time, the RAnt distribution is averaged over time and therefore displays where the RAnts were mostly located throughout the run. At low cooperation numbers, the RAnt density is generally distributed all across the arena. Localization of the density toward one region was observed for low cooperation parameters as excavated wall elements were forming a new boundary that confined the RAnt motion to that region (see e.g.  $C = 0$  T4,  $C = 0.25$  T4). As the cooperation number increases, more distinct localized density becomes apparent. Due to the photomone field Rants operating at higher cooperation parameter values are more likely to start excavating in locations where RAnts have previously been present. The location of that attracting field is not known a priori, but emerges spontaneously through the interaction with other RAnts. The location of the peak density field at higher cooperation numbers strongly correlates with the point of excavation in the wall. The difference in RAnt behavior as a function of the cooperation parameter is the degree of focus during excavation as represented by the von Mises parameter of the angular position of excavated boundary elements shown in ??(a). A large value of the parameter indicates a high degree of concentration of the excavation effort, while low values indicate a scattered distribution of many digging sites. Another metric to assess the behavioral difference induced by the cooperation parameter is the traveled distance of the RAnts. SI **Figure 2** (b) displays the total travelled distance of a rAnt  $x$  normalized by the arena diameter  $D$  as a function of the normalized time  $t/t_s$ , where  $t_s = D/v_b$  and  $v_b$  the base speed, shows that RAnts travel a greater distance in the same amount of time at higher concentration parameters. The theoretical limit of the travelled distance is shown with the dashed line in the left-hand side figure, reflecting that RAnts do not constantly move at base speed, but are interrupted by other RAnts, obstacles, and fetching/dropping manoeuvres. As shown in SI **Figure 2** (c), RAnts travel at about a fifth of the base speed on average. An increase of the average speed is observed as a function of the cooperation parameter, which can be explained by the fact that obstacles are more scattered at lower cooperation parameters, effectively reducing the mean free path of a RAnt.



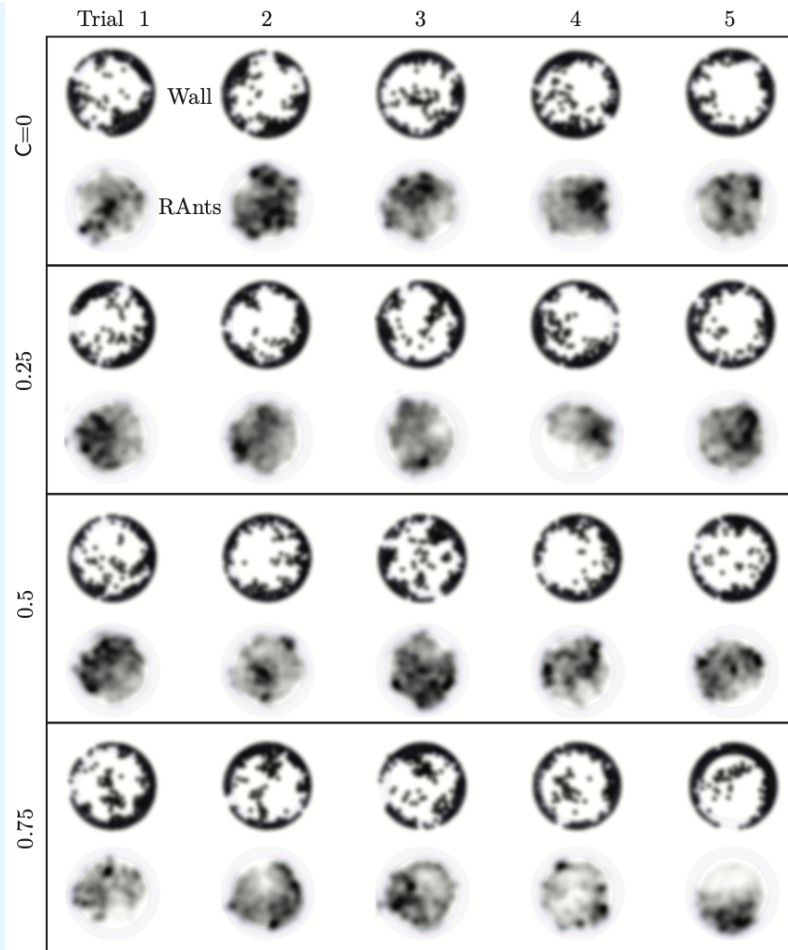
885  
886  
888

**Appendix 3 Figure 3.** Final wall element distribution and averaged RAnt density field (in units of  $\#/cm^2$ ) over the full duration of the run for all 20 experiments.

889  
890  
891  
892  
893  
894  
895  
896

### RAnt density

In our main result we used five RAnts to explore cooperative excavation in an artificial system. More RAnts than five hindered the excavation behavior as fellow RAnts would block each others path or disturb a RAnt during the fetching and deposition of wall elements. Fewer RAnts did manage to excavate out, but the excavation rate is slower and the spontaneous formation of an excavation site due to accumulation of photormone occurs later if at all. SI **Figure 4** shows the final wall element positions and RAnt density field averaged over time for  $C = 1$  and two experiments with one RAnt and two experiments with three RAnts.



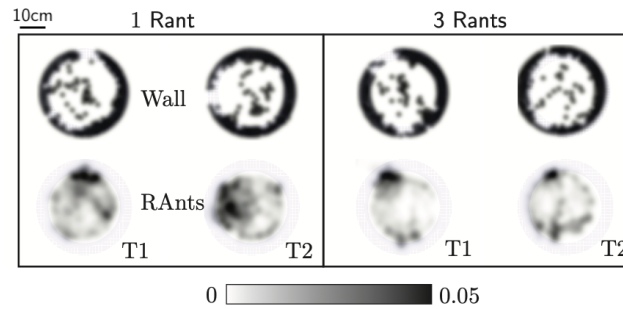
897  
898  
899  
900  
901  
902  
903  
904  
905  
906  
907  
908  
909  
910  
911  
912  
913  
914  
915

**Appendix 3 Figure 4.** Final wall element distribution and averaged RAnt density field (in units of  $\#/cm^2$ ) over the full duration of the run for experiments with one and three RAnts. The cooperation parameter was set to  $C = 1$  and the experiments was repeated twice (Trials T1 and T2).

A single RAnt can efficiently excavate a site if an initial photormone seed is present, but it is not robust. In fact, even though the RAnt in T2 managed to remove some elements in the last layer, it never excavated out but lost the photormone seed where it was digging and started diffusing again. Three rants were more successful in generating an initial photormone seed, but excavation occurred at multiple sites even for  $C = 1$  since the lower number of RAnts did not generate one dominating photormone field.

### Phases of cooperation in RAnts

In the RAnt case we can infer the phase in which the RAnts operate by looking at the tunnel size,  $1/K_b(t)$  and the location along the boundary at which the RAnts are localized,  $\rho_r(\phi)$  as they execute their task. We find that in the jammed and diffused phase there exists no tunnel and the variance remains zero throughout the process. However the location along the boundary  $\phi_b$  at which the RAnts spend their time the most has a large peak around the jammed location due to high cooperation which in the case of diffusion remains widespread (see ??).



916  
917  
918  
919  
920  
922

**Appendix 3 Figure 5.** From the RAnt experiments in *Figure 8*,  $K_b$  is the von Mises concentration parameter computed from the location of the boundary and  $\phi_r$  is the angular distribution of the RAnts in the arena averaged over time.  $\phi_b$  is the time-averaged mean azimuthal location of the RAnts in the arena. RAnts present over longer periods in a particular sector of the arena will cause a peak in  $\phi_r$ . One can infer the phase the RAnts are in by measuring these two quantities.

923  
924  
925  
926  
927  
928  
929

A successful tunnel, as we have already seen, has an initial increase in the variance that plateaus rapidly due to cooperation driven focus at a given location. As the RAnts are localized, focusing on their task, we again see peaks around the location of the tunnel. For a partial tunnel, due to low cooperation, the variance in the tunnel size is large and the location along the boundary the RAnts spend their effort is spread out. Thus the phase the RAnts operate in can be distinguished by using information about the environment, i.e. the tunnel size, in combination with agent dynamics, i.e. their location.

# AI discovers new nanostructures

Scientists at the U.S. Department of Energy's (DOE) Brookhaven National Laboratory have successfully demonstrated that autonomous methods can discover new materials. The artificial intelligence (AI)-driven technique led to the discovery of three new nanostructures, including a first-of-its-kind nanoscale "ladder." The research was published today in *Science Advances*.

The newly discovered structures were formed by a process called self-assembly, in which a material's molecules organize themselves into unique patterns. Scientists at Brookhaven's Center for Functional Nanomaterials (CFN) are experts at directing the self-assembly process, creating templates for materials to form desirable arrangements for applications in microelectronics, catalysis, and more. Their discovery of the nanoscale ladder and other new structures further widens the scope of self-assembly's applications.

"Self-assembly can be used as a technique for nanopatterning, which is a driver for advances in microelectronics and computer hardware," said CFN scientist and co-author Gregory Doerk. "These technologies are always pushing for higher resolution using smaller nanopatterns. You can get really small and tightly controlled features from self-assembling materials, but they do not necessarily obey the kind of rules that we lay out for circuits, for example. By directing self-assembly using a template, we can form patterns that are more useful."

Staff scientists at CFN, which is a DOE Office of Science User Facility, aim to build a library of self-assembled nanopattern types to broaden their applications. In previous studies, they demonstrated that new types of patterns are made possible by blending two self-assembling materials together.

"The fact that we can now create a ladder structure, which no one has ever dreamed of before, is amazing," said CFN group leader and co-author Kevin Yager. "Traditional self-assembly can only form relatively simple structures like cylinders, sheets, and spheres. But by blending two materials together and using just the right chemical grating, we've found that entirely new structures are possible."

Blending self-assembling materials together has enabled CFN scientists to uncover unique structures, but it has also created new challenges. With many more parameters to control in the self-assembly process, finding the right combination of parameters to create new and useful structures is a battle against time. To accelerate their research, CFN scientists leveraged a new AI capability: autonomous experimentation.

In collaboration with the Center for Advanced Mathematics for Energy Research Applications (CAMERA) at DOE's Lawrence Berkeley National Laboratory, Brookhaven scientists at CFN and the National Synchrotron Light Source II (NSLS-II), another DOE Office of Science User Facility at Brookhaven Lab, have been developing an AI framework that can autonomously define and perform all the steps of an experiment. CAMERA's gpCAM algorithm drives the framework's autonomous decision-making. The latest research is the team's first successful demonstration of the algorithm's ability to discover new materials.

"gpCAM is a flexible algorithm and software for autonomous experimentation," said Berkeley Lab scientist and co-author Marcus Noack. "It was used particularly ingeniously in this study to autonomously explore different features of the model."

"With help from our colleagues at Berkeley Lab, we had this software and methodology ready to go, and now we've successfully used it to discover new materials," Yager said. "We've now learned enough about autonomous science that we can take a materials problem and convert it into an autonomous problem pretty easily."

To accelerate materials discovery using their new algorithm, the team first developed a complex sample with a spectrum of properties for analysis. Researchers fabricated the sample using the CFN nanofabrication facility and carried out the self-assembly in the CFN material synthesis facility.

"An old school way of doing material science is to synthesize a sample, measure it, learn from it, and then go back and make a different sample and keep iterating that process," Yager said. "Instead, we made a sample that has a gradient of every parameter we're interested in. That single sample is thus a vast collection of many distinct material structures."

Then, the team brought the sample to NSLS-II, which generates ultrabright x-rays for studying the structure of materials. CFN operates three experimental stations in partnership with NSLS-II, one of which was used in this study, the Soft Matter Interfaces (SMI) beamline.

"One of the SMI beamline's strengths is its ability to focus the x-ray beam on the sample down to microns," said NSLS-II scientist and co-author Masa Fukuto. "By analyzing how these microbeam x-rays get scattered by the material, we learn about the material's local structure at the illuminated spot. Measurements at many different spots can then reveal how the local structure varies across the gradient sample. In this work, we let the AI algorithm pick, on the fly, which spot to measure next to maximize the value of each measurement."

As the sample was measured at the SMI beamline, the algorithm, without human intervention, created a model of the material's numerous and diverse set of structures. The model updated itself with each subsequent x-ray measurement, making every measurement more insightful and accurate.

In a matter of hours, the algorithm had identified three key areas in the complex sample for the CFN researchers to study more closely. They used the CFN electron microscopy facility to image those key areas in exquisite detail, uncovering the rails and rungs of a nanoscale ladder, among other novel features.

From start to finish, the experiment ran about six hours. The researchers estimate they would have needed about a month to make this discovery using traditional methods.

"Autonomous methods can tremendously accelerate discovery," Yager said. "It's essentially 'tightening' the usual discovery loop of science, so that we cycle between hypotheses and measurements more quickly. Beyond just speed, however, autonomous methods increase the scope of what we can study,

meaning we can tackle more challenging science problems."

"Moving forward, we want to investigate the complex interplay among multiple parameters. We conducted simulations using the CFN computer cluster that verified our experimental results, but they also suggested how other parameters, such as film thickness, can also play an important role," Doerk said.

The team is actively applying their autonomous research method to even more challenging material discovery problems in self-assembly, as well as other classes of materials. Autonomous discovery methods are adaptable and can be applied to nearly any research problem.

"We are now deploying these methods to the broad community of users who come to CFN and NSLS-II to conduct experiments," Yager said. "Anyone can work with us to accelerate the exploration of their materials research. We foresee this empowering a host of new discoveries in the coming years, including in national priority areas like clean energy and microelectronics."

This research was supported by the DOE Office of Science.

## MATERIALS SCIENCE

# Autonomous discovery of emergent morphologies in directed self-assembly of block copolymer blends

Gregory S. Doerk<sup>1\*</sup>, Aaron Stein<sup>1</sup>, Suwon Bae<sup>1</sup>, Marcus M. Noack<sup>2</sup>, Masafumi Fukuto<sup>3</sup>, Kevin G. Yager<sup>1\*</sup>

The directed self-assembly (DSA) of block copolymers (BCPs) is a powerful approach to fabricate complex nanostructure arrays, but finding morphologies that emerge with changes in polymer architecture, composition, or assembly constraints remains daunting because of the increased dimensionality of the DSA design space. Here, we demonstrate machine-guided discovery of emergent morphologies from a cylinder/lamellae BCP blend directed by a chemical grating template, conducted without direct human intervention on a synchrotron x-ray scattering beamline. This approach maps the morphology-template phase space in a fraction of the time required by manual characterization and highlights regions deserving more detailed investigation. These studies reveal localized, template-directed partitioning of coexisting lamella- and cylinder-like subdomains at the template period length scale, manifesting as previously unknown morphologies such as aligned alternating subdomains, bilayers, or a "ladder" morphology. This work underscores the pivotal role that autonomous characterization can play in advancing the paradigm of DSA.

## INTRODUCTION

An overarching goal of research in self-assembly is to create arbitrarily elaborate and customizable objects with prescribed hierarchical control down to the nanoscale or even molecular scale. Encoding the requisite complex organizational information, however, entails the use of concomitantly more complex building blocks or constraints, sacrificing in part, the appeal of self-assembly as a synthesis strategy (1). This trade-off is exemplified in block copolymers (BCPs), where the macromolecular architecture reliably encodes the emergent self-assembled morphology, correlating morphological customizability with synthetic complexity (2). This interdependence can be overcome in part by blending BCPs with other polymers or nanomaterials that selectively segregate to one block (3–11) or layering BCPs with different domain sizes or morphologies (12–17). Meanwhile, epitaxial registration of assembled BCP domains to chemical or topographical templates in directed self-assembly (DSA) can impose local control over BCP chain distortion, domain orientation, or pattern transferability to generate non-native pattern symmetries in two and three dimensions (18–22). These approaches avoid the synthesis of complex polymers but introduce their own complexities with respect to process control, template design, and composition selection. Accelerating progress in their use hinges upon exploring the relevant high-dimensional parameter spaces more efficiently and discovering the unifying principles that dictate how and why particular assembly motifs emerge.

Previously, we have demonstrated an approach to selectively enhance and control the complexity of nanopatterns formed through DSA by using a mixture of BCPs that acts as a responsive blend (23). Specifically, we used a 1:1 blend of cylindrical and lamellar diblock copolymers of near-equal molar mass, which self-

assembles to form coexisting line and dot patterns in thin films (24). Using a chemical grating template to order and align the BCP blend pattern through DSA, competing influences of polymer chain distortion and preferential wetting can be exploited to locally select between line and dot patterns simply by adjusting the grating template pitch and/or linewidth. This locally selective DSA can even be extended to single-domain resolution with precise registry between the template and the self-assembled pattern to form a single line in an ordered hexagonal array of dots, for instance (23). Because of the challenges of manual characterization and analysis, however, the prior investigation was restricted to a narrow region of the template parameter space around where the template pitch ( $\Lambda$ ) matches the natural domain spacing of the BCP blend ( $L_0$ ). In this narrow template range, the resulting line and dot patterns are effectively two-dimensional; more complex assembly behavior, including the emergence of three-dimensional morphologies, may be possible as the template parameter space is widened. Here, we investigate the assembly of this same blend on chemical patterns spanning a much larger range of line widths and pitches, including pitches more than two times the equilibrium self-assembled spacing ( $\Lambda \geq 2L_0$ ). To bypass the laborious, time-consuming, and often-confusing enterprise of characterization and analysis by exhaustive electron microscopy, we instead probe the system autonomously using synchrotron x-ray scattering. Without direct human intervention, we systematically map the self-assembly behavior in multiple quantitative dimensions across the entire chemical pattern space.

The results of this autonomous mapping reveal an intriguing capacity for the blend to form unusual three-dimensional morphologies, whose unit cells exhibit local partitioning into nominally cylinder-like and lamella-like subdomains, all in registry with the underlying chemical template. These emergent three-dimensional morphologies depend sensitively on the chemical pattern dimensions. At incommensurate values of  $\Lambda$  between  $L_0$  and  $2L_0$ , this can yield subdomain bilayers exhibiting preferential top subdomain alignment along specific skew angles with respect to the grating

Copyright © 2023 The Authors, some rights reserved; exclusive licensee American Association for the Advancement of Science. No claim to original U.S. Government Works. Distributed under a Creative Commons Attribution License 4.0 (CC BY).

<sup>1</sup>Center for Functional Nanomaterials, Brookhaven National Laboratory, Upton, NY 11973, USA. <sup>2</sup>The Center for Advanced Mathematics for Energy Research Applications (CAMERA), Lawrence Berkeley National Laboratory, Berkeley, CA 94720, USA. <sup>3</sup>National Synchrotron Light Source II, Brookhaven National Laboratory, Upton, NY 11973, USA.

\*Corresponding author. Email: gdoerk@bnl.gov (G.S.D.); kyager@bnl.gov (K.G.Y.)

direction. Meanwhile, in the vicinity of  $\Lambda \approx 2L_0$ , subdomain partitioning manifests as either line patterns composed of alternating subdomains aligned along the grating direction or a “ladder” morphology consisting of lamella-like “rails” and cylinder-like “rungs.” To the best of our knowledge, neither the ladder, skew, nor alternating morphologies have been observed in previous studies. These findings underscore the immense potential for pairing combinatorial sampling with autonomous characterization to empower researchers and to accelerate the discovery of approaches for generating designer hierarchical self-assembled morphologies.

## RESULTS

Our strategy to accelerate the discovery of self-assembled phases comprises three synergistically linked elements. The first is the fabrication of a combinatorial array sample with systematically varied chemical template dimensions, by which one can survey a large parameter space without resorting to serial sample creation. Following our previous work (23), the assembly process starts with a chemical pattern fabricated using polymer brush grafting, electron beam lithography, and oxygen plasma etching. The chemical pattern is a simple one-dimensional grating consisting of alternating hydrophobic polystyrene (PS) brush stripes and hydrophilic (ostensibly silicon oxide) stripes of width  $w$  with a template pitch  $\Lambda$  (Fig. 1A). The sample comprises a contiguous array of grating chemical patterns, each pattern being a 60  $\mu\text{m}$ -by-60  $\mu\text{m}$  square field with lines oriented parallel to the sample  $y$  axis. Two defining features of the gratings are systematically varied across this combinatorial array. The electron beam patterning dose increases with  $y_c$ , effectively increasing  $w$ , while  $\Lambda$  varies from 30 to 130 nm with  $x_c$ , where the “c” subscript indicates positions in the patterned combinatorial array. This combinatorial array, depicted schematically in fig. S1, increases the design space with respect to our previous work by a factor of five in terms of  $\Lambda$  alone. As in our previous report, cylinder- and lamellae-forming PS-*block*-poly(methyl methacrylate) (PS-*b*-PMMA) with nearly equivalent molar mass were blended in equal parts by weight in toluene solution. Films about 40 nm thick were spin-casted from solution onto the chemical pattern. The film was annealed overnight under vacuum to enable self-assembly of the BCP blend thin film with an isotropic

(undirected) natural period ( $L_0$ ) of  $\sim 54$  nm. To enhance contrast for x-ray scattering and to enable electron microscopy of the domain structure, PMMA was selectively infiltrated with  $\text{Al}_2\text{O}_3$  and the polymer was subsequently removed using oxygen plasma treatment, generating inorganic replicas of the assembled PMMA domains. Removal of the polymer would cause collapse for morphologies consisting of isolated domains (e.g., spheres); the prevalent vertical orientation and interconnectivity of the inorganic replicas prevent this in morphological structures observed here. Details of the template fabrication, assembly, and infiltration processes can be found in Materials and Methods.

The second element of our approach is the use of microfocused transmission small-angle x-ray scattering (SAXS) at a synchrotron x-ray scattering beamline, in which measurements performed with an area of tens of micrometers provide a wealth of structural information on the time scale of seconds. This provides the high-resolution characterization needed to understand complex assembly behavior at speeds required to explore the design space efficiently. SAXS measurements were performed in transmission geometry, as shown schematically in Fig. 1B, at the Soft Matter Interfaces (SMI) beamline at the National Synchrotron Light Source II (NSLS-II). To avoid unwanted averaging across adjacent patterning fields, the x-ray beam was focused to a  $\sim 2\text{-}\mu\text{m}$  vertical by  $\sim 25\text{-}\mu\text{m}$  horizontal spot on the sample. The 200- $\mu\text{m}$ -thick Si wafer substrates and the high x-ray contrast provided by the alumina replicas of PMMA domain structures ensured sufficient signal that required only 2 s per measurements. Compared with a more conventional approach to characterization, e.g., systematic scanning electron microscopy by a capable operator, synchrotron SAXS offers major improvements in measurement throughput. Assuming 90 s per image, using SAXS at a synchrotron can provide a  $\sim 45\times$  boost in characterization speed.

The third element of our strategy is the use of autonomous characterization methods, wherein a machine-learning algorithm selects measurements based on a continually updating analysis of the existing dataset. As described in detail in the Materials and Methods and in previous publications (25–28), the autonomous x-ray measurements and analysis were performed using a fully automated, closed-loop workflow that combines sample positioning, data collection, real-time data analysis, and machine-guided selection of

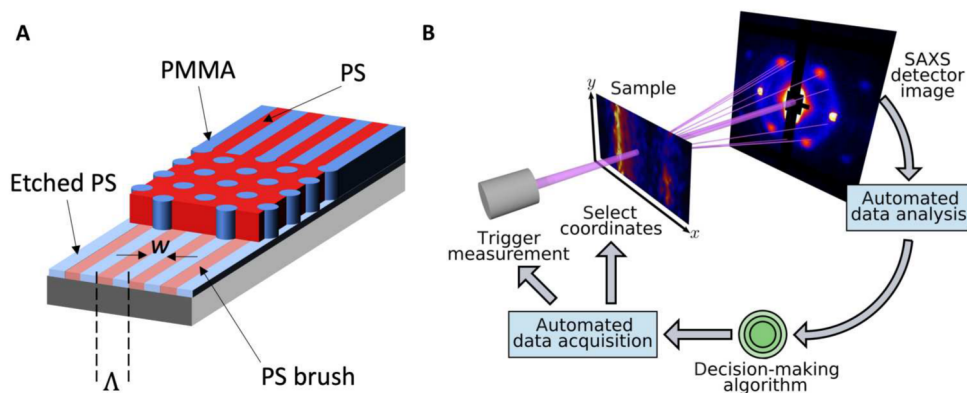


**Fig. 1. Schematics of the experimental approach.** (A) DSA of a 1:1 blend of cylindrical and lamellar PS-*b*-PMMA BCPs is achieved using a grating chemical surface pattern with hydrophilic stripes of width  $w$  on a pitch  $\Lambda$ , etched into a surface-grafted PS brush. (B) Autonomous SAXS measurement schematic. A motion system allows the instrument to select any  $(x, y)$  coordinate on the surface of the combinatorial sample for measurement. The SAXS pattern at each position is fed into a data analysis pipeline. A decision-making algorithm based on Gaussian process (GP) methods then selects the next coordinate for measurement.

subsequent measurement locations within the pattern array. The control algorithm was a Gaussian process (GP) regression method (29), which constructs an interpolated surrogate model for the experimental parameter space, along with a corresponding uncertainty model. Over the course of the experiment, we switched between maximizing three different objective functions [ $F(x_c, y_c)$ ]. The first is defined as the GP posterior variance of the scattering intensity (of the peak associated with the BCP),  $F(x_c, y_c) = \sigma_{GP}^2(x_c, y_c)$ , which leads to efficient exploration of the input space without any particular focus. This objective function places new measurement points wherever model uncertainty is highest, thus maximizing knowledge gain per measurement. The second objective function, defined as  $F(x_c, y_c) = 3\sigma_{GP}(x_c, y_c) + m_{GP}(x_c, y_c)\sigma_{GP}(x_c, y_c)$ , where  $m_{GP}$  is the GP posterior mean of the scattering intensity, balances maximum signal and uncertainty while simultaneously preventing the data acquisition from getting stuck in specific regions of the parameter space. This mode provides a balance between focusing on regions of high scattering intensity while also continuing to explore the parameter space. The third objective function drew the focus onto regions with high uncertainty among scattering peak heights in the 30°, 60°, and 90° azimuthal directions. This objective function is given by

$$F(x_c, y_c) = \text{mean}\{|\mathbf{a}(x_c, y_c) - \text{mean}[\mathbf{a}(x_c, y_c)]|^2\} \quad (1)$$

where  $\mathbf{a}(x_c, y_c)$  is a vector of the positive peak height posterior means in the three directions. This objective function focuses attention on areas deemed “interesting” by the experimenter in the sense that they are regions with notable differences in the scattering of the different morphological populations. The ability to shift between different acquisition strategies, while always leveraging all previously collected data in modeling and thus prediction, is a useful feature of the human-supervised approach described here and enabled efficient data collection. Overall, the GP method implements Bayesian modeling and thus allows data collection that accounts for uncertainty. By selecting locations with large model uncertainty for subsequent measurements, the algorithm maximizes information gain per measurement. Including a term in objective functions that

scales with signal intensity emphasizes data collection in regions with good structural order. Last, inclusion of multiple signals (for different azimuthal angles) allows the model to consider the ordering of multiple populations simultaneously and thus to minimize the uncertainty in the distributions of these distinct populations.

By avoiding oversampling of areas with low uncertainty, as would occur in a grid search, the GP algorithm rapidly highlights areas meriting further scientific investigation. This benefit becomes critically important as parameter spaces increase in size and dimensionality or as individual measurements become more costly (e.g., require longer acquisition times) (27). In the work presented here, synthetic tests comparing GP regression to a simulated grid search at the same number of measurements reveal that the autonomous algorithm achieves both a faster reduction in error and a lower overall error in modeling the experimental parameter space. The surrogate model shows that the autonomous GP algorithm provides a complete model of the parameter space in a fraction of the time (see fig. S2 in the Supplementary Materials). Moreover, while synchrotron x-ray scattering affords notable advantages in certain contexts (x-ray scattering may be necessary to resolve nanoscale three-dimensional morphologies), the GP regression algorithm is agnostic to the characterization approach. It could be applied equally well, for example, to electron microscope images acquired through critical dimension scanning electron microscopy, a rapid and automated characterization method in common use within the nanoelectronics industry. Fourier transforms of the resultant scanning electron micrographs (SEMs) could be analyzed by automated fitting procedures similar to those used here.

Our automated analysis pipeline provides several signals that can be used as the quantity of interest for autonomous control, including scattering peak height, position, or width (which measure the amount of ordered material, repeat-spacing, and the spatial correlation length, respectively). As noted above, the scattering peak height (i.e., the prefactor from a Gaussian fit to the first-order peak arising from the BCP ordering) along different azimuthal directions was selected as the input signal for the work shown here. The GP model for the fitted prefactor ( $p$ ) of the primary scattering

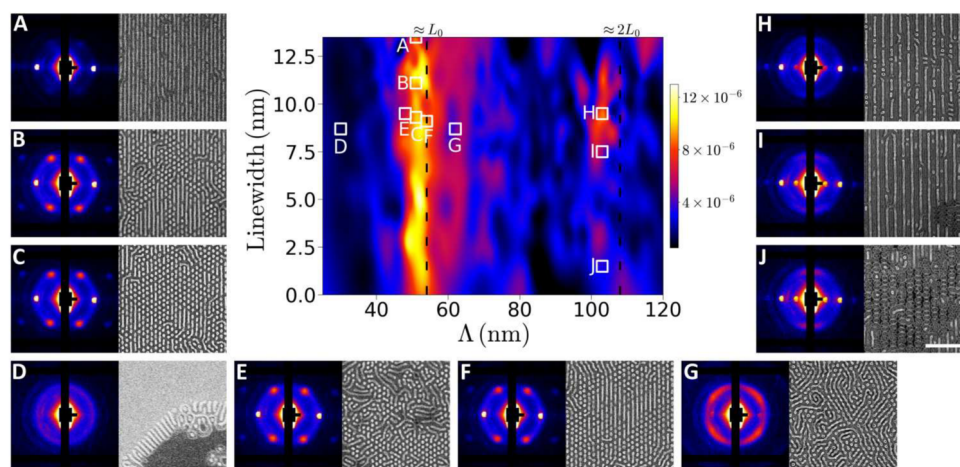


**Fig. 2. Emergent morphologies within the DSA design space.** At the center is a map of scattering prefactor intensity ( $p$ ) as a function of  $\Lambda$  and  $w$ . Exemplar SAXS patterns, accompanied by corresponding SEMs, indicate regions of the design space dominated by self-assembled line (A), hexagonal or line (B, C, E, and F), isotropic (D), skew (G), and alternating cylinders and lamellae or ladder (H to J) patterns. These pattern types are described in more detail in the main text. The white scale bar denoting 500 nm in (J) applies to all SEMs.

peak is plotted as a function of  $\Lambda$  and  $w$  in Fig. 2. We note that the values of  $w$  shown here are simulated as described in Materials and Methods, and absolute values may be different after oxygen plasma etching, although the trends are preserved. The GP model extrapolates slightly to the lowest and highest  $w$  values, as shown in fig. S3. Similar maps of domain repeat spacing ( $d_0$ ) and spatial correlation length ( $\xi$ ) can be generated on the basis of the fit of the primary scattering peak. These maps represent specific populations of pattern types based on the choice of an azimuthal sector average (see fig. S4).

As a representation of the degree of order and alignment along the grating direction (perpendicular to  $\Lambda$ ), the spatial distribution of  $p$  immediately captures salient features of the samples. Two high-intensity vertical bands signaling optimal alignment and ordering are present at  $\Lambda$  just larger than  $\sim 50$  and  $\sim 100$  nm. An informed researcher might anticipate these bands at  $\Lambda \approx L_0$  and  $\Lambda \approx 2L_0$ , as BCPs are expected to align and register with the template at these pitch dimensions to minimize both the interfacial and elastic free energies in the BCP thin film (23, 30, 31). Counter to expectations, however,  $p$  is highest at  $\Lambda$  approximately  $\sim 4\%$  less than  $L_0$  or  $2L_0$ , which can be attributed to the inherent responsivity of the blend

(compared to a neat BCP) and the lower free-energy penalty for chain compression versus tension (32). The autonomous workflow found this feature independently of human experimenters. In addition, the autonomous workflow revealed trends that are not expected on the basis of heuristic guidance, such as asymmetric intensity toward larger pitches in the vicinity of  $\Lambda \geq L_0$  and a highly dose-dependent intensity in the range of  $\Lambda \approx 2L_0$ . These features motivated detailed and targeted additional investigation, as discussed below.

BCP domain alignment to the chemical pattern is maximized when the  $\Lambda$  is nearly commensurate with the  $L_0$ . Consistent with our previous report (23), holding  $\Lambda$  near  $\sim L_0$  while decreasing the dose results in a transition from assembled line patterns to hexagonal dot patterns (Fig. 2, A to C). At all  $w$  values for  $\Lambda < 44$  nm, the morphological pattern is predominantly isotropic, as evidenced by the azimuthally uniform SAXS pattern obtained from the exemplar measurement in Fig. 2D. The corresponding SEMs obtained from the same approximate location show that the morphology is composed of terraced lamellae, with lines orthogonal to the terrace edges, which likely include a combination of both cylindrical and lamellar chains. At these chemical pattern pitches, the BCP blend cannot align in registry with the pattern without excessive chain deformation; instead, the patterned brush can be considered a "compositionally random" brush (33) that presents a net PS-preferential interface for the blend given that the calculated duty cycles ( $w/\Lambda$ ) patterned by our electron beam lithography process are less than 30% across the entire array. Hexagonal dot patterns are apparent at  $\Lambda$  just slightly less than  $L_0$  (Fig. 2E), but the conflicting influences of template wetting and chain compression frustrate ordered alignment, leading to an enhanced level of defectivity. As  $\Lambda$  is increased to values above  $\sim L_0$ , however, the hexagonal dot patterns (Fig. 2F) give way to a different pattern type in which PMMA domains form partial line patterns that skew within the substrate plane at specific angles with respect to the grating axis, as exemplified in Fig. 2G.

A strong dependence of the magnitude of  $p$  with respect to dose is observed near  $\Lambda \approx 2L_0$ , a feature not observed at  $\Lambda \approx L_0$ . The reason for this can be ascertained by inspection of SAXS patterns and SEMs acquired at  $\Lambda \approx 2L_0$ , exemplars of which are shown for various doses in Fig. 2 (H to J). Higher doses (Fig. 2, H and I) are characterized by line patterns parallel with the grating direction. The lines exhibit alternating high and low contrast in the corresponding SEMs. As detailed later, we hypothesize that these lines are alternating subdomains enriched with cylindrical or lamellar chains. On the other hand, a completely different morphology that resembles a ladder with rails along the grating direction and rungs orthogonal to it emerges at lower doses (Fig. 2J). This ladder morphology can be considered as a more complex partitioning of cylinder-like and lamella-like subdomains, much like what is observed with the alternating lamella-like and cylinder-like subdomains at high doses, but in which the cylinder-like subdomains orient perpendicularly to the grating direction to satisfy commensurability constraints. A larger set of exemplary SAXS patterns and SEMs are presented in figs. S5 and S6.

On the basis of the observations above, five distinct types of patterns are observed within the template area: isotropic, lines, hexagonal (dots), skew, and ladder. The scattering intensity along the azimuthal direction can be decomposed into a weighted set of contributions corresponding to the identified morphology types. From this, we can construct maps of each patterning motif within the  $\Lambda$

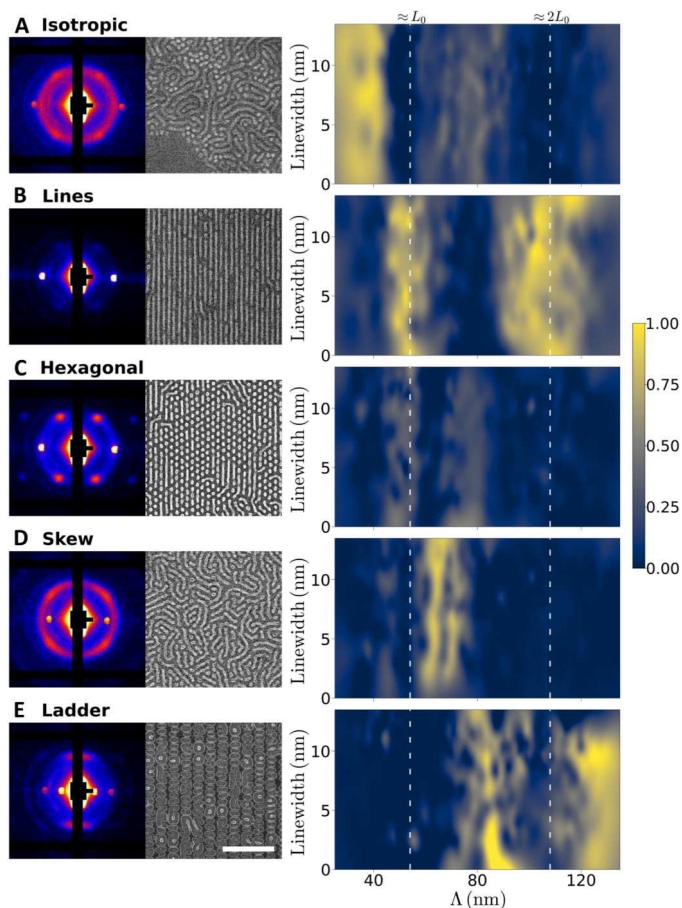


**Fig. 3. Weighted contributions from specific pattern motifs within the template design space based on fitting the azimuthal scattering data.** Exemplar SAXS patterns and SEMs (left) corresponding to intensity maps (right) are shown for self-assembled isotropic (A), line (B), hexagonal (C), skew (D), and ladder (E) patterns. The white scale bar denoting 500 nm in (E) applies to all SEMs.

versus  $w$  design space, as shown in Fig. 3 (details about how these interpolated maps are prepared may be found in Materials and Methods). These intensity maps of selected SAXS signals reveal notable trends in the way the blend self-assembles in response to the underlying template. As expected, isotropic patterns (Fig. 3A) dominate for  $\Lambda < L_0$ , where the substrate surface is compositionally random, while line patterns (Fig. 3B) are most prominent when the template pitch is nearly commensurate with the domain spacing ( $\Lambda \approx L_0$  or  $2L_0$ ). Hexagonal patterns (Fig. 3C) overlap with the line patterns around  $\Lambda \approx L_0$ . While this analysis does not show the dose-dependent transition between hexagonal and line patterns, it does show that hexagonal patterns are also prominent in region of  $\Lambda \geq L_0$ . Skew patterns (Fig. 3D) emerge as  $\Lambda$  is increased to just larger than  $L_0$  and recede in prominence as  $\Lambda$  is further increased. The ladder pattern (Fig. 3E) replaces the skew pattern with increasing pitch and becomes the dominant pattern in the array for larger pitches except in proximity to  $\Lambda \approx 2L_0$ . These trends demonstrate that the blends are highly responsive to the template chemical pattern in unusual ways that would be difficult to predict, find, and understand by a conventional, manual experiment paradigm.

The azimuthal angle of maximum SAXS intensity along the primary BCP peak yields an average alignment angle for the morphology within the combinatorial sample ( $\chi_c$ ) that can be plotted across the template design space, as shown in Fig. 4A, where  $\chi_c = 0^\circ$  when patterns align orthogonally to the template grating direction.  $\chi_c$  is ill-defined in the isotropic region ( $\Lambda < L_0$ ) and hence is distributed randomly there. On the other hand, for  $\Lambda > 2L_0$ ,  $\chi_c$

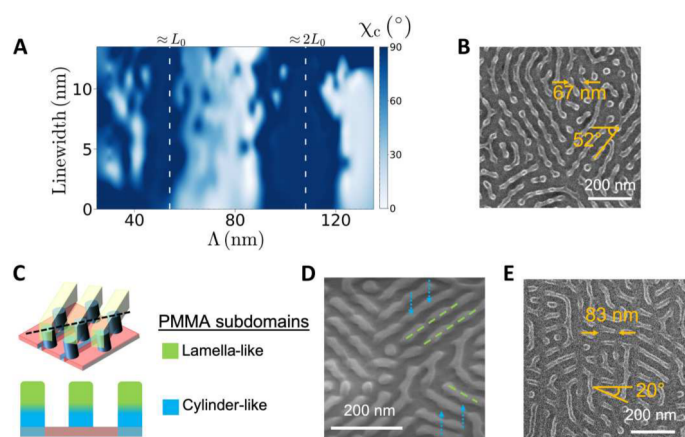


**Fig. 4. Bilayer and complex morphologies in the skew region of the template parameter space.** (A) Map of  $\chi_c$  across the template design space. Patterns are aligned with the grating direction at  $\chi_c = 90^\circ$  and against the grating direction at  $\chi_c = 0^\circ$ . A continuous variation in  $\chi_c$  is apparent in the region identified with the skew morphology within the range of  $L_0 \leq \Lambda \leq 2L_0$ . (B) SEM of a skew pattern showing vertical hexagonal posts connected by lines at angles similar to those of  $\chi_c$  measured by SAXS patterns for the first population. (C) Schematic of the proposed bilayer morphology responsible for skew patterns. Lamella-like subdomains in the top layer (green) are transparent in the top view. The cross section is taken through the vertical plane along the dashed black line. Green and blue represent lamella-like (i.e., enriched with symmetric BCP chains) and cylinder-like (i.e., enriched with PMMA-minority BCP chains) PMMA subdomains, respectively. (D) SEM of a skew pattern taken at a  $45^\circ$  tilt angle. Blue dotted arrows and green dashed lines indicate the inferred positions of cylinder-like and lamella-like subdomains, respectively. (E) SEM of the complex morphology that emerges at  $\Lambda \geq 70$  nm.

clusters near zero, which we attribute to scattering signal from the rungs of the ladder pattern. The most striking feature, however, is the negative correlation between  $\chi_c$  and  $\Lambda$  in the region where skew patterns predominate. There are two distinct populations of  $\chi_c$  that are responsive to the template, as discussed in the Supplementary Materials (including fig. S7).

SEMs obtained from selected locations within skew region ( $\Lambda = 60$  to  $80$  nm), an example of which is shown in Fig. 4B, reveal dots on a hexagonal lattice, although the lattice is often rotated by  $\sim 30^\circ$  from the cases near  $\Lambda = L_0$  in which the hexagonal dot patterns are well registered to the chemical pattern template. Furthermore, numerous lines are observed to connect these dots at angles from the direction orthogonal to the template grating, which are consistent with  $\chi_c$ . We infer that the observed morphology is a bilayer, depicted schematically in Fig. 4C, where vertical posts on a hexagonal lattice assemble at the template interface, while lines assemble at the air interface. For added clarity, in Fig. 4D, we mark the hypothesized posts and lines in a SEM from the skew region taken at a  $45^\circ$  tilt by dotted blue arrows and dashed green lines, respectively. A simple trigonometric calculation based on this bilayer model can provide a plausible upper limit for the relationship between  $\chi_c$  to  $\Lambda$ , as discussed in the Supplementary Materials. The bilayer motif appears to break down at  $\Lambda \gtrsim 70$  nm into a more complex morphology (Fig. 4E) with reduced dependence of  $\chi_c$  on  $\Lambda$  that is reminiscent of nonbulk morphologies previously observed for symmetric diblock copolymers on highly incommensurate chemical patterns (34, 35). Note that multiple types of morphologies coexist within the skew region of the template parameter space, indicating an energetic degeneracy among them (see fig. S8). Additional tilt-view SEMs from the skew region that support our designation of the bilayer morphology are provided in the fig. S9.

We posit that the bilayer morphology and other unusual patterns observed in the skew region are a consequence of the capacity of the blend to accommodate incommensurability between  $\Lambda$  and  $L_0$  by locally partitioning into distinct morphological objects, or subdomains, within a morphological unit cell of area  $\Lambda \times L_0$  (bounded vertically by the film thickness). This partitioning can be thought of as the result of highly localized enrichment of BCP chains directed by the chemical pattern template. In the absence of external directing fields, energetic penalties associated with chain stretching or compression due to chain mixing promote localized enrichment of cylindrical and lamellar BCP chains within a thin film blend of lamellar and cylindrical BCPs of nearly equivalent molecular weight, as used here, leading to the self-assembly of coexisting dot and lines patterns (24, 36). On the other hand, a chemical pattern template imposes a strong directing field that can enforce the assembly of a single pattern type (i.e., lines or dots), aligned and registered with the template, which minimizes chain distortion while satisfying surface wetting constraints (23). As the template pitch increases, however, a single pattern type (i.e., only lines or only dots) cannot accommodate the resulting incommensurability between template and domain spacing. For templates in the range of  $L_0 < \Lambda < 2L_0$ , the space between grating lines is insufficient to enable distinct subdomains to coexist at their natural spacing within a single layer in registration with the template. In response, the blend may self-assemble to form a bilayer morphology with layers partitioned according to the general subdomain shape. Although subdomain shapes often change continuously with position throughout the

film, we find it useful to classify subdomains as “cylinder-like” when enrichment of cylindrical BCP chains either between or within the subdomains stabilizes higher domain interfacial curvature. On the other hand, similar enrichment of lamellar BCP chains can stabilize “lamella-like” subdomains with lower domain interfacial curvature.

The patterns found in the vicinity of  $\Lambda \approx 2L_0$  can again be understood as a product of the partitioning of the blend into cylinder-like and lamella-like subdomains within a unit cell; here, however, the partitioning occurs within a single layer, which is made possible by the larger spacing between template grating lines. For larger  $w$  at  $\Lambda \approx 2L_0$  (Fig. 2, H and I), lamella-like PMMA subdomains assemble directly above the template grating to maximize favorable contact between PMMA and hydrophilic regions, while cylinder-like PMMA subdomains align horizontally and in parallel with the PMMA lamella-like subdomains, as depicted schematically in Fig. 5A. The line patterns in this area of the template space are thus composed of alternating and aligned subdomains. This configuration minimizes both enthalpic penalties due to domain/template mismatch and entropic penalties due to chain stretching while satisfying the constraint of equal volume for cylindrical and lamellar chains. Accompanying SEMs (Fig. 5, B to D) are consistent with the alternating subdomain model. Here, we mark the hypothetical lamella-like and cylinder-like subdomains by dashed green and dotted blue lines, respectively. PMMA within the nominal lamella-like subdomains above guiding lines extends across the entire film thickness, resulting in a higher degree of alumina infiltration that provides brighter contrast and more prominent alumina replicas of these subdomains in top-view (Fig. 5B) and tilted-view (Fig. 5D) SEMs, respectively. A horizontal dotted white line in the cross-sectional SEM (Fig. 5C) marks the bottom of the lamella-like subdomains, whereas the alternating cylinder-like subdomains are identifiable by their reduced depth. The apparent flat or concave surfaces at the top of the subdomains in Fig. 5C are likely an artifact from the milling process used to obtain the cross section.

As  $w$  decreases (Fig. 2J), the mismatched contact area between PMMA subdomains and the hydrophilic template lines introduces an enthalpic energy penalty; reducing the subdomain width,

however, compresses chains within the subdomains above guiding lines and stretches chains within the alternating subdomains. The blend can resolve this dilemma by orienting the cylinder-like PMMA subdomains orthogonally to the template grating line direction to minimize chain distortion, resulting in the ladder morphology depicted schematically in Fig. 5E and shown in a representative top-view SEM in Fig. 5F. Under this hypothesis, lamella-like PMMA subdomains form the ladder rails, while cylinder-like PMMA subdomains form the rungs. For added clarity, we again mark the hypothetical lamella-like and cylinder-like subdomains by dashed green and dotted blue lines, respectively. Cross-sectional and tilt-view SEMs [Fig. 5 (G and H, respectively)] demonstrate that the ladder morphology contacts the substrate along the ladder rails, which are connected to each other by suspended rungs, consistent with the proposed mechanism for ladder self-assembly.

The orientation of the subdomains orthogonally to the template guiding lines to minimize chain stretching also explains why ladder patterns dominate at  $\Lambda$  slightly more or less than  $2L_0$ . Lamella-like PMMA assembles on top of the template lines to minimize mismatched contact area, while the orthogonal horizontal cylinder-like PMMA subdomains fill the space between template lines without incurring an enthalpic penalty. Measurements of the spacing between rungs from SEMs at  $\Lambda$  values ranging from  $\sim 90$  to 130 nm maintain a consistent value of  $54 \pm 2$  nm. The equivalence of the rung spacing with the equilibrium domain spacing for the overall blend across a large range of  $\Lambda$  supports the proposed mechanism for ladder assembly. Additional SEMs provided in figs. S10 and S11, including cross sections obtained from milling by a focused ion beam, reinforce the conclusions regarding the three-dimensional morphologies observed in the vicinity of  $\Lambda \approx 2L_0$ .

Using coarse-grained molecular dynamics (MD) simulations, we have previously shown that highly localized chain redistribution and enrichment at the scale of single morphological objects in thin film blends of cylindrical and lamellar BCPs stabilizes coexistence phases (i.e., dots and lines) (36). We therefore used MD simulations to investigate the assembly behavior of a blend of “L”

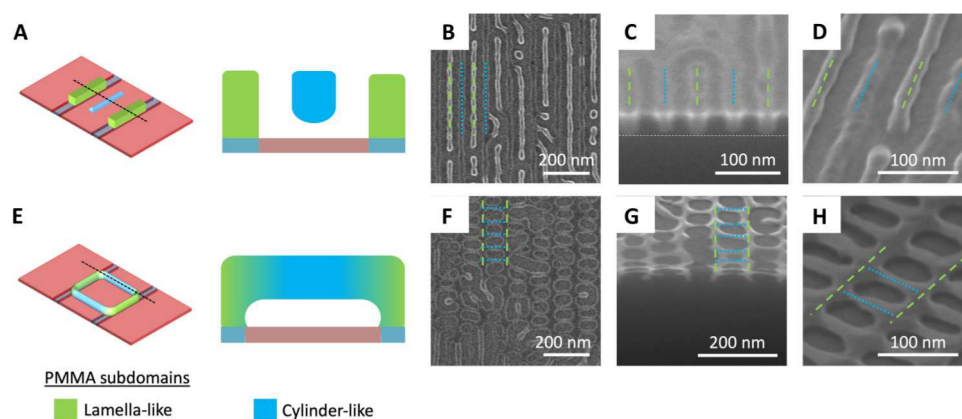


**Fig. 5. Emergent patterns in proximity to  $\Lambda \approx 2L_0$ .** Schematic unit cell (A) and top-view (B), cross-sectional (C), and tilt-view (D) SEMs of alternating cylinder-like (i.e., enriched with PMMA-minority BCP chains) and lamella-like (i.e., enriched with symmetric BCP chains) subdomains aligned along the grating direction, which emerge in the vicinity of  $\Lambda \approx 2L_0$  and larger values of  $w$ . Schematic unit cell (E) and top-view (F), cross-sectional (G), and tilt-view (H) SEMs of ladder structures, which emerge in the vicinity of  $\Lambda \approx 2L_0$  and smaller values of  $w$  or in regions where  $\Lambda$  is slightly more or less than  $2L_0$ . Green and blue represent lamella-like and cylinder-like PMMA subdomains, respectively. Right schematics represent cross-sectional slices at the position of the dotted lines in the left schematics. Green dashed and blue dotted lines in the SEMs indicate the inferred positions of lamella-like and cylinder-like subdomains, respectively.

(symmetric) and “C” (asymmetric) BCP chains on a wide range of chemical patterns analogous to those used experimentally. Simulation details are provided in Materials and Methods. An exemplar MD simulation result is shown in perspective view in Fig. 6A, with a portion of the film removed to reveal the underlying chemical pattern, and in a cross-sectional view along a slice taken orthogonally to the chemical grating direction in Fig. 6B. At these template dimensions ( $\Lambda \approx 2L_0$  and  $w/\Lambda = 0.100$ ), corresponding to the template region in the vicinity of Fig. 2H, the agreement with the experimentally observed alternating morphology is remarkable. Simulated

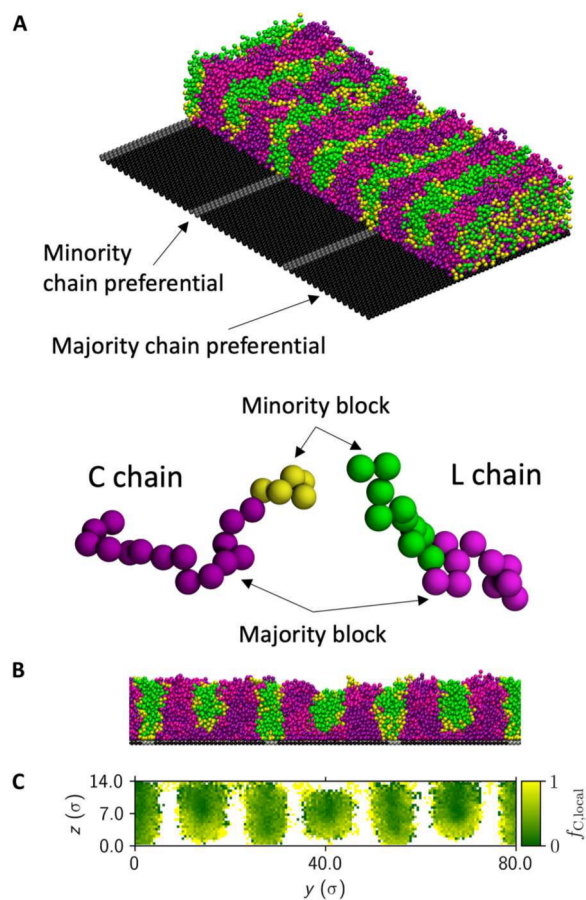


**Fig. 6. Exemplar coarse-grained MD simulation result for a cylindrical/lamellar BCP blend on a chemical grating template with  $\Lambda \approx 2L_0$  and  $w/\Lambda = 0.100$ .** Black substrate beads are preferential for majority BCP chains, analogous to PS brush-grafted regions, while gray substrate beads are preferential for minority BCP chains, analogous to etched grating lines. Symmetric L chains consist of blocks colored green and magenta, while the minority and majority blocks in asymmetric C chains are colored yellow and purple, respectively. Minority beads in the different chain types are chemically identical and are colored differently only for visualization purposes (similarly for majority beads). A perspective view of the result with a portion of the film removed to reveal the underlying chemical pattern (A) and a cross-sectional view taken orthogonally to the chemical grating direction (B) reveal a remarkable agreement with the experimentally observed alternating morphology (in the vicinity of Fig. 2H). The local fraction of cylindrical minority BCP chains ( $f_{C,local}$ ) plotted in (C) reveals enrichment of asymmetric (cylindrical) chains near the substrate between grating lines. This local redistribution of chains stabilizes the assembly of aligned cylinder-like subdomains. Here, “y” is the direction perpendicular to the gratings; “z” is the substrate normal direction, and the unit ( $\sigma$ ) is the bead size parameter.

minority subdomains (PMMA in the experiment) contact the substrate at the location of the grating lines, whereas the alternating minority subdomains are separated from the brush-grafted substrate regions by majority block chains.

To elucidate the role of localized chain enrichment in the self-assembly of the alternating morphology, the average molecular fraction of C minority block chains ( $f_{C,local}$ ) along the grating direction is plotted in Fig. 6C versus the substrate normal direction ( $z$ ) and the direction perpendicular to the gratings ( $y$ ), where the color code between C and L minority species matches the chain schematic in Fig. 6A. Notably,  $f_{C,local}$  increases near the substrate within alternating subdomains not above grating lines, signaling a localized enrichment of C BCP chains that accommodates the higher interfacial curvature required to separate the minority subdomain from the unfavorable brush-grafted substrate. Our MD simulations therefore strongly support our hypothesis that localized cylindrical or lamellar chain enrichment is essential to the assembly of the previously undiscovered morphologies described in this report.

As shown in the Supplementary Materials, simulations performed on chemical patterns in which  $w$  is reduced or  $\Lambda$  is shifted away from  $\sim 2L_0$  reveal a self-assembled morphology that bears a remarkable resemblance to the proposed bilayer structure for skew patterns and occurs in the same general regions of the template parameter space (figs. S12 and S13). While less common, hints of the ladder morphology are also observed in simulations across these same regions, as evidenced in figs. S12 and S14. Moreover, alternating morphologies become more common as film thickness is reduced (figs. S15 and S16), while a tendency toward defective, ladder-like morphologies is apparent when film thickness is increased (fig. S17). This suggests that film thickness may play an important role in the presence or absence of specific emergent morphologies formed through subdomain partitioning.

A high level of defectivity is generally observed in self-assembled patterns across the entire template. In part, this is a natural outcome of self-assembly in polymer blends, which can stabilize template-programmable defects (22). As the objective of this work is to deploy the synergistic combination of combinatorial sampling and autonomous characterization for morphological discovery, we did not endeavor to optimize our templates for the defect-free assembly of any particular morphology. Nevertheless, our results highlight key trends that may lead to formalized template design rules for morphological selection. As an example, both experiment and simulations show that aligned and alternating subdomains are largely constrained to larger values of  $w$  near  $\Lambda \approx 2L_0$  (see Figs. 2 and 3B). Consideration of past research on BCP DSA using chemical patterns (31, 37) suggests that this alternating morphology would be most strongly selected for when  $w \approx 0.5L_0$ , as this would minimize enthalpic penalties incurred at the interface between the template and lamella-like subdomains. Meanwhile, the ladder morphology is clearly dominant at  $\Lambda > 2L_0$  (Fig. 3E), a region of the template design space where it does not compete with the skew morphology. Considering the morphology transition from ladder to alternating lines with increasing  $w$  at  $\Lambda \approx 2L_0$ , the ladder morphology may be most strongly selected for when  $\Lambda > 2L_0$  and  $w \ll 0.5L_0$ .

## DISCUSSION

We have characterized complex three-dimensional morphologies that emerge via self-assembly of BCP blend thin films in response to underlying chemical pattern templates. By autonomously mapping a combinatorial sample using synchrotron x-ray scattering, we have substantially expanded the explorable parameter space compared to previous experiments while simultaneously providing multifaceted morphology descriptors, all without immediate human intervention. The autonomously derived results guided subsequent electron microscopy characterization, enabling the judiciously targeted selection of regions to image for interpreting the assembly behavior. This investigation revealed the emergence of previously unknown morphologies such as a bilayer structure, alternating gratings, and a ladder morphology; it also helped distill the general principle of subdomain partitioning that can be used to predict, interpret, and design patterns by the DSA of BCP blends, thereby adding a valuable mechanism to engineer hierarchical self-assembled morphologies with precise registry control. While our results are germane to selective DSA using BCP blends, the general approach to autonomously characterizing large parameter spaces demonstrated here provides a wealth of crucial information to understand complex assembly behavior while freeing up human experimenters to focus on interpretation and hypothesis formulation.

## MATERIALS AND METHODS

## Materials

Hydroxyl-terminated PS “brush” (PS-OH, number average molar mass ( $M_n$ ) = 10.5 kg mol<sup>-1</sup>, polydispersity index (PDI) = 1.06), lamellae-forming PS-*b*-PMMA ( $M_n$  = 52-*b*-52 kg mol<sup>-1</sup>, PDI = 1.09), and cylinder-forming PS-*b*-PMMA ( $M_n$  = 64-*b*-35 kg mol<sup>-1</sup>, PDI = 1.09) were obtained from Polymer Source and used as received. The PS brush was dissolved in propylene glycol monomethyl ether acetate (PGMEA) at a concentration of 1% by weight, while the BCPs were dissolved in toluene at a concentration of 1% by weight. BCP solutions were prepared by combining the two pure BCP solutions in a 1:1 weight ratio. Polished silicon wafers that were 200 μm thick were purchased from University Wafer.

## Sample fabrication

After cleaning by O<sub>2</sub> plasma treatment, the PS brush was grafted to a silicon wafer coupon with dimensions of ~2 cm by ~3 cm that was spin-casting a film of it at 1500 rpm and annealing on a hot plate for 5 min at 250°C under continuous nitrogen purging to chemically graft the brush to the substrate. Ungrafted brush was removed by spin-rinsing in PGMEA at 3000 rpm. PMMA electron beam resist (950 K) was spin-coated to a thickness of ~50 nm and baked on a hot plate at 180°C for 3 min. Line/space grating patterns were exposed in a JEOL JBX6300-FS electron beam lithography tool using 1-nA beam current with doses ranging from 1200 to 2080 μC cm<sup>-2</sup>. After exposure, the samples were developed in room temperature methyl isobutyl ketone:isopropyl alcohol (1:3) for 60 s and rinsed in isopropyl alcohol. Exposed grating patterns were transferred to the PS brush by oxygen plasma etching (Trion Phantom) RIE tool using 10 standard cubic centimeters per minute (sccm) O<sub>2</sub> at 50 mtorr, with 15-W radio frequency power for ~40 s. The remaining PMMA was removed by soaking in

toluene at 60°C for 15 min, with the final 10 min in an ultrasonic bath, followed by soaking in N-Methyl-2-pyrrolidone at 180°C for 10 min in an ultrasonic bath, and lastly in room temperature methanol for 5 min in an ultrasonic bath. Grating linewidths were simulated across the entire combinatorial array using the BEAMER software package (GenISys). A point spread function for PMMA on silicon was applied on the grating pattern in the electron beam simulation module, looping over a range of grating pitches and electron beam doses that matched the exposure conditions. The BEAMER metrology module was used to extract linewidths at each array position.

The BCP blend film was subsequently spin-casted onto the chemical pattern from toluene solution at 2000 rpm and thermally annealed in a vacuum oven at 220°C for ~18 hours. After annealing, alumina replicas of the three-dimensional PMMA domain structure were synthesized through vapor phase infiltration as described previously (38) to enhance contrast for electron microscopy and x-ray scattering. Briefly, the sample was placed into a commercial atomic layer deposition tool (Cambridge Ultratech Savannah S100) with a base pressure <1 torr and exposed to four cycles of exposure to trimethylaluminum and water vapor (100 s each) at 85°C. The polymer was then removed by oxygen plasma ashing at 20 W and ~100 mtorr (March Plasma CS1701F) to reveal the alumina replicas.

## X-ray scattering characterization

Transmission SAXS experiments were conducted at the SMI (12-ID) beamline at the NSLS-II at Brookhaven National Laboratory. The beamline x-ray energy was set to 16.1 keV (corresponding to x-ray wavelength of 0.7701 Å). SAXS data were collected on a photon-counting pixel array detector (Dectris PILATUS 1M) with a pixel size of 172 μm. Data were converted to reciprocal space ( $q$ ) using the calibrated sample-detector distance (8.3020 m). Data were analyzed using the SciAnalysis software package, which computes a variety of signals for each experimental detector image. We computed the isotropic one-dimensional scattering curve  $I(q)$  based on the azimuthal average of the full SAXS pattern, as well as the sectorized one-dimensional curve for a variety of angles (from 0° to 90° relative to the grating line direction). For each pattern, the position, width, and height of the scattering peak were quantified by fitting to a Gaussian peak with a linear background. The scattering intensity in the azimuthal direction ( $\chi_c$ ), at the  $q$  value of the BCP first-order peak (i.e.,  $q_0 \sim 0.0117 \text{ \AA}^{-1}$ ; which corresponds to real space distances of  $d_0 \sim 54 \text{ nm}$ ), was extracted. From this  $I(\chi_c)$  data, we fit a circularly wrapped orientation distribution function to quantify the alignment direction (39–42)

$$I(\chi_c) = \frac{(1 + \eta)^2 - 4\eta}{(1 + \eta)^2 - 4\eta \cos^2 \chi_c} \quad (2)$$

where  $\eta$  quantifies the anisotropy. We also fit these data to a weighted sum of orientation functions for the different morphology populations; the relative weights thereby provide estimates of population contributions to the measured scattering intensity. We define the “line” population as a  $I(\chi_c)$  distribution with twofold symmetry and aligned along  $\chi_c = 90^\circ$ , the “hex” population as sixfold symmetric aligned along  $30^\circ$ , the “skew” population as fourfold symmetric aligned along  $45^\circ$ , and the ladder population as twofold symmetric aligned along  $0^\circ$ .

For autonomous characterization, we fed the selected analysis signals into the gpCAM (29) software, which implements GP modeling for arbitrary signals across arbitrarily dimensioned parameter spaces (25–28). The underlying kernel was anisotropic (28), accounting for differences in the correlations along the  $x_c$  ( $\Lambda$ ) and  $y_c$  ( $w$ ) directions. The presented maps of analysis signals were generated using a GP model, with hyperparameters trained on the full dataset. Thus, they represent an interpolated map that takes into account the experimental data, its corresponding uncertainty, and the learned correlation behavior through the parameter space. Autonomous control was implemented using an objective function that included a term proportional to the surrogate model uncertainty and a term proportional to the data signals; we used the scattering peak intensities (in the 30°, 60°, and 90° azimuthal directions) as the signals of interest.

### Electron microscopy

Top-down imaging was performed using a Hitachi S-4800 scanning electron microscope at 10-kV accelerating voltage. Cross-sectional and tilt-view SEMs were acquired using a FEI Helios scanning electron microscope at 5-kV accelerating voltage.

### Coarse-grained MD simulations

MD simulated films were made from linear A-*b*-B BCP chains described by a coarse-grained, Kremer-Grest bead-spring model (36, 43–45). Asymmetric (cylinder-forming) “C” and symmetric (lamellae-forming) “L” chains are the same length (20 beads) and are differentiated by their A block fraction: The A block fraction is 0.25 and 0.5 for the asymmetric and symmetric BCPs, respectively. Each bead has unit mass (1.0 $m$ ) for all types, and the interactions between BCP chain beads consist of bonded and nonbonded potentials. Parameters  $m$ ,  $\sigma$ ,  $\epsilon$ , and  $\tau$  are units for mass, distance, energy, and time, respectively, and  $\tau = \sigma(m/\epsilon)^{1/2}$ . The bonded interactions between every pair of adjacent chain beads are governed by a finitely extensible nonlinear elastic (FENE) potential as described in Eq. 3, which is a sum of attractive (first term) and repulsive (second term) potentials, resulting in a wall-like potential with an equilibrium

length

$$U_{\text{FENE}}(r) = -0.5kR_0^2 \ln\left(1 - \frac{r^2}{R_0^2}\right) + 4\epsilon_{ij} \left[ \left(\frac{\sigma_{ij}}{r}\right)^{12} - \left(\frac{\sigma_{ij}}{r}\right)^6 + \frac{1}{4} \right] \quad (3)$$

where  $r$  is the distance between beads,  $k$  is a spring constant,  $R_0$  is a maximum length,  $\epsilon_{ij}$  is the strength of interaction between a bead of type  $i$  and a bead of type  $j$ , and  $\sigma_{ij}$  is the finite distance at which the interbead potential is zero. The second term is cut off and shifted to zero energy at  $r_c$  of  $\sqrt{[6]2}$ , and thus is purely repulsive. The nonbonded interactions are modeled using a Lennard-Jones (LJ) potential as described in Eq. 4 and apply to every pair of beads except covalently bonded ones.  $\epsilon_{ij}$  and  $\sigma_{ij}$  share the same definitions as in Eq. 3

$$U_{\text{LJ}}(r) = \begin{cases} 4\epsilon_{ij} \left[ \left(\frac{\sigma_{ij}}{r}\right)^{12} - \left(\frac{\sigma_{ij}}{r}\right)^6 \right], & r \leq r_c \\ 0, & r > r_c \end{cases} \quad (4)$$

The LJ potential is cut off and shifted to zero at a  $r_c$  of  $2.5\sigma$ , due to which the nonbonded interactions include attractive interactions. We set potential parameters so that the self-cohesion of A block can be slightly stronger than that of B block as given in Table 1, which mirrors a BCP such as PS-*b*-PMMA where PMMA and PS are A and B blocks, respectively.

We used the same number of symmetric and asymmetric BCPs to construct each film in the simulation box with a chemical pattern at the bottom surface, depicted in fig. S18.  $L_y$  was set to have three to four pitches in the simulation box, and then,  $L_x$  was set to  $L_y/1.618$  using the golden ratio.  $L_z$  is much larger than the film thickness to induce the film-air (vacuum) interface. Periodic boundary conditions were imposed in the  $x$  and  $y$  axis so that the model can represent thin films. Each film was equilibrated (annealed) up to  $0.3 \times 10^6 \tau$  with a time step of  $0.006\tau$  at  $T = 1.2\epsilon/k_B$  using the NVT ensemble with a Nosé-Hoover thermostat. The chemical patterned substrate mirrors the experimental substrate; thin stripes of width  $w$  constructed from fixed  $S_A$  beads (preferential to the A block) are separated from each other at a pitch  $\Lambda$  by regions on the substrate constructed from fixed  $S_B$  beads, where  $S_A$  and  $S_B$  beads share the same interaction strengths ( $\epsilon_{ij}$ ) as A and B beads, respectively.  $\Lambda$  varied from  $18\sigma$  to  $34\sigma$ , and the duty cycle ( $w/\Lambda$ ) varied from 0.0 to 0.2. The BCP films were initially disordered with no phase separation and they self-assemble into morphologies during equilibration. The resulting films are about  $12\sigma$  thick, and the domain spacing is about  $13\sigma$ .

All simulations were carried out on the Institutional Cluster of the Scientific Data and Computing Center at Brookhaven National Laboratory using the LAMMPS simulation package made available by Sandia National Laboratories (46). Molecular snapshots were captured using the VMD software package (47). Different colors were used for symmetric and asymmetric BCPs to aid visualization: Yellow and green for A beads of C and L BCPs, respectively, and purple and magenta for their respective B beads. The chemical pattern B and A beads were colored black and silver, respectively. To quantify the distribution of cylindrical BCP chains in the resultant morphology, we defined the metric  $f_{C, \text{local}}$  as the ratio of the number of C chain beads to the total number of beads.

**Table 1. Parameters used for FENE and LJ potentials.**

Parameter	Value
$k$	$30\epsilon/\sigma^2$
$R_0$	$1.5\sigma$
$r_c$ (FENE)	$\sqrt{[6]2}\sigma$
$r_c$ (LJ)	$2.5\sigma$
$\sigma_{AA} = \sigma_{BB} = \sigma_{AB} = \sigma_{SA} = \sigma_{SB}$	$1.0\sigma$
$\epsilon_{AA}$	$1.01\epsilon$
$\epsilon_{AB} = \epsilon_{BA}$	$0.50\epsilon$
$\epsilon_{BB}$	$0.99\epsilon$

## Supplementary Materials

## This PDF file includes:

Supplementary Text  
Figs. S1 to S18

[View/request a protocol for this paper from Bio-protocol.](#)

## REFERENCES AND NOTES

- G. S. Doerk, K. G. Yager, Beyond native block copolymer morphologies. *Mol. Syst. Des. Eng.* **2**, 518–538 (2017).
- F. S. Bates, G. H. Fredrickson, Block copolymers—Designer soft materials. *Phys. Today* **52**, 32–38 (1999).
- K. I. Winey, E. L. Thomas, L. J. Fetters, Isothermal morphology diagrams for binary blends of diblock copolymer and homopolymer. *Macromolecules* **25**, 2645–2650 (1992).
- Y. Zhao, K. Thorkelsson, A. J. Mastroianni, T. Schilling, J. M. Luther, B. J. Rancatore, K. Matsunaga, H. Jinnai, Y. Wu, D. Poulsen, J. M. J. Fréchet, A. P. Alivisatos, T. Xu, Small-molecule-directed nanoparticle assembly towards stimuli-responsive nanocomposites. *Nat. Mater.* **8**, 979–985 (2009).
- Y. Matsushita, A. Takano, M. Vayer, C. Sinturel, Nonclassical block copolymer self-assembly resulting from a constrained location of chains and junctions. *Adv. Mater. Interfaces* **7**, 1902007 (2020).
- K. Toth, C. O. Osuji, K. G. Yager, G. S. Doerk, High-throughput morphology mapping of self-assembling ternary polymer blends. *RSC Adv.* **10**, 42529–42541 (2020).
- B. C. Garcia, M. Kamperman, R. Ulrich, A. Jain, S. M. Gruner, U. Wiesner, Morphology diagram of a diblock copolymer—Aluminosilicate nanoparticle system. *Chem. Mater.* **21**, 5397–5405 (2009).
- M. W. Matsen, Stabilizing new morphologies by blending homopolymer with block copolymer. *Phys. Rev. Lett.* **74**, 4225–4228 (1995).
- C. Choi, S. Ahn, J. K. Kim, Diverse morphologies of block copolymers by blending with homo (and Co) polymers. *Macromolecules* **53**, 4577–4580 (2020).
- A. P. Lindsay, R. M. Lewis, B. Lee, A. J. Peterson, T. P. Lodge, F. S. Bates, A15,  $\sigma$ , and a quasicrystal: Access to complex particle packings via bidisperse diblock copolymer blends. *ACS Macro Lett.* **1**, 197–203 (2020).
- R. Zhang, Z. Qiang, M. Wang, Integration of polymer synthesis and self-assembly for controlled periodicity and photonic properties. *Adv. Funct. Mater.* **31**, 2005819 (2021).
- N. Demazy, C. Cummins, K. Aissou, G. Fleury, Non-native block copolymer thin film nanostructures derived from iterative self-assembly processes. *Adv. Mater. Interfaces* **7**, 1901747 (2020).
- A. Rahman, P. W. Majewski, G. Doerk, C. T. Black, K. G. Yager, Non-native three-dimensional block copolymer morphologies. *Nat. Commun.* **7**, 13988 (2016).
- P. W. Majewski, A. Rahman, C. T. Black, K. G. Yager, Arbitrary lattice symmetries via block copolymer nanomeshes. *Nat. Commun.* **6**, 7448 (2015).
- C. Jin, B. C. Olsen, E. J. Lubner, J. M. Buriak, Preferential alignment of incommensurate block copolymer dot arrays forming moiré superstructures. *ACS Nano* **11**, 3237–3246 (2017).
- B. B. Patel, D. J. Walsh, D. H. Kim, J. Kwok, B. Lee, D. Guirionnet, Y. Diao, Tunable structural color of bottlebrush block copolymers through direct-write 3D printing from solution. *Science. Sci. Adv.* **6**, eaaz7202 (2020).
- C. He, M. P. Stoykovich, Photopatterning of cross-linkable epoxide-functionalized block copolymers and dual-tone nanostructure development for fabrication across the nano- and microscales. *Small* **11**, 2407–2416 (2015).
- Y. Ding, K. R. Gadelrab, K. Mizrahi Rodriguez, H. Huang, C. A. Ross, A. Alexander-Katz, Emergent symmetries in block copolymer epitaxy. *Nat. Commun.* **10**, 2974 (2019).
- A. K. G. Tavakkoli, K. W. Gotrik, A. F. Hannon, A. Alexander-Katz, C. A. Ross, K. K. Berggren, Templating three-dimensional self-assembled structures in bilayer block copolymer films. *Science* **336**, 1294–1298 (2012).
- A. Tavakkoli, K. G. S. M. Nicaise, A. F. Hannon, K. W. Gotrik, A. Alexander-Katz, C. A. Ross, K. K. Berggren, Sacrificial-post templating method for block copolymer self-assembly. *Small* **10**, 493–499 (2014).
- G. S. Doerk, J. Y. Cheng, G. Singh, C. T. Rettner, J. W. Pitera, S. Balakrishnan, N. Arellano, D. P. Sanders, Enabling complex nanoscale pattern customization using directed self-assembly. *Nat. Commun.* **5**, 5805 (2014).
- M. P. Stoykovich, M. Müller, S. O. Kim, H. H. Solak, E. W. Edwards, J. J. de Pablo, P. F. Nealey, Directed assembly of block copolymer blends into nonregular device-oriented structures. *Science* **308**, 1442–1446 (2005).
- A. Stein, G. Wright, K. G. Yager, G. S. Doerk, C. T. Black, Selective directed self-assembly of coexisting morphologies using block copolymer blends. *Nat. Commun.* **7**, 12366–12366 (2016).
- K. G. Yager, E. Lai, C. T. Black, Self-assembled phases of block copolymer blend thin films. *ACS Nano* **8**, 10582–10588 (2014).
- M. M. Noack, K. G. Yager, M. Fukuto, G. S. Doerk, R. Li, J. A. Sethian, A kriging-based approach to autonomous experimentation with applications to X-ray scattering. *Sci. Rep.* **9**, 11809 (2019).
- M. M. Noack, G. S. Doerk, R. Li, M. Fukuto, K. G. Yager, Advances in kriging-based autonomous X-ray scattering experiments. *Sci. Rep.* **10**, 1325 (2020).
- M. M. Noack, P. H. Zwart, D. M. Ushizima, M. Fukuto, K. G. Yager, K. C. Elbert, C. B. Murray, A. Stein, G. S. Doerk, E. H. R. Tsai, R. Li, G. Freychet, M. Zhernenkov, H.-Y. N. Holman, S. Lee, L. Chen, E. Rotenberg, T. Weber, Y. L. Goc, M. Boehm, P. Steffens, P. Mutti, J. A. Sethian, Gaussian processes for autonomous data acquisition at large-scale synchrotron and neutron facilities. *Nat. Rev. Phys.* **3**, 685–697 (2021).
- M. M. Noack, G. S. Doerk, R. Li, J. K. Streit, R. A. Vaia, K. G. Yager, M. Fukuto, Autonomous materials discovery driven by Gaussian process regression with inhomogeneous measurement noise and anisotropic kernels. *Sci. Rep.* **10**, 17663 (2020).
- M. Noack, J. Sethian, K. Yager, M. Fukuto, P. Zwart, D. Ushizima, H. Krishnan, S. Lee, R. Pandolfi, I. Humphrey, D. Perryman, P. Enfedaque, A. Hexemer, S. Sarker, T. Weber, A. Mehta, R. Li, G. Doerk, M. Boehm, gpCAM, Version 7.3.4, gitHub (2022); <https://doi.org/10.5281/zenodo.5975553>.
- J. Y. Cheng, A. M. Mayes, C. A. Ross, Nanostructure engineering by templated self-assembly of block copolymers. *Nat. Mater.* **3**, 823–828 (2004).
- G. S. Doerk, C.-C. Liu, J. Y. Cheng, C. T. Rettner, J. W. Pitera, L. E. Krupp, T. Topuria, N. Arellano, D. P. Sanders, Pattern placement accuracy in block copolymer directed self-assembly based on chemical epitaxy. *ACS Nano* **7**, 276–285 (2013).
- D. F. Sunday, E. Ashley, L. Wan, K. C. Patel, R. Ruiz, R. J. Kline, Template–polymer commensurability and directed self-assembly block copolymer lithography. *J Polym Sci B* **53**, 595–603 (2015).
- W. Lee, Y. Kim, S. Jo, S. Park, H. Ahn, D. Y. Ryu, Irreversible physisorption of PS-b-PMMA copolymers on substrates for balanced interfacial interactions as a versatile surface modification. *ACS Macro Lett.* **8**, 519–524 (2019).
- G. Liu, F. Detcheverry, A. Ramírez-Hernández, H. Yoshida, Y. Tada, J. J. de Pablo, P. F. Nealey, Nonbulk complex structures in thin films of symmetric block copolymers on chemically nanopatterned surfaces. *Macromolecules* **45**, 3986–3992 (2012).
- F. A. Detcheverry, G. Liu, P. F. Nealey, J. J. de Pablo, Interpolation in the directed assembly of block copolymers on nanopatterned substrates: Simulation and experiments. *Macromolecules* **43**, 3446–3454 (2010).
- S. Bae, K. G. Yager, Chain redistribution stabilizes coexistence phases in block copolymer blends. *ACS Nano* **16**, 17107–17115 (2022).
- C. Liu, A. Ramírez-Hernández, E. Han, G. S. W. Craig, Y. Tada, H. Yoshida, H. Kang, S. Ji, P. Gopalan, J. J. de Pablo, P. F. Nealey, Chemical patterns for directed self-assembly of lamellae-forming block copolymers with density multiplication of features. *Macromolecules* **46**, 1415–1424 (2013).
- G. S. Doerk, K. G. Yager, Rapid ordering in “wet brush” block copolymer/homopolymer ternary blends. *ACS Nano* **11**, 12326–12336 (2017).
- W. Ruland, H. Tompa, The effect of preferred orientation on the intensity distribution of (hk) interferences. *Acta Cryst A* **24**, 93–99 (1968).
- W. Ruland, B. Smarsly, SAXS of self-assembled oriented lamellar nanocomposite films: An advanced method of evaluation. *J. Appl. Cryst.* **37**, 575–584 (2004).
- K. G. Yager, C. Forrey, G. Singh, S. K. Satija, K. A. Page, D. L. Patton, J. F. Douglas, R. L. Jones, A. Karim, Thermally-induced transition of lamellae orientation in block-copolymer films on ‘neutral’ nanoparticle-coated substrates. *Soft Matter* **11**, 5154–5167 (2015).
- K. J. De France, K. G. Yager, T. Hoare, E. D. Cranston, Cooperative ordering and kinetics of cellulose nanocrystal alignment in a magnetic field. *Langmuir* **32**, 7564–7571 (2016).
- K. Kremer, G. S. Grest, Dynamics of entangled linear polymer melts: A molecular-dynamics simulation. *J. Chem. Phys.* **92**, 5057–5086 (1990).
- C. Forrey, K. G. Yager, S. P. Broadaway, Molecular dynamics study of the role of the free surface on block copolymer thin film morphology and alignment. *ACS Nano* **5**, 2895–2907 (2011).
- K. Toth, S. Bae, C. O. Osuji, K. G. Yager, G. S. Doerk, Film thickness and composition effects in symmetric ternary block copolymer/homopolymer blend films: Domain spacing and orientation. *Macromolecules* **54**, 7970–7986 (2021).
- S. Plimpton, Fast parallel algorithms for short-range molecular dynamics. *J. Comput. Phys.* **117**, 1–19 (1995).
- W. Humphrey, A. Dalke, K. Schulten, VMD: Visual molecular dynamics. *J. Mol. Graph.* **14**, 33–38 (1996).

**Acknowledgments:** This research used the Materials Synthesis and Characterization Facility and the Nanofabrication Facility at the Center for Functional Nanomaterials (CFN), the SMI end station at the NSLS-II, and the Scientific Data and Computing Center, a component of the

Computational Science Initiative, which are U.S. Department of Energy Office of Science User Facilities, at Brookhaven National Laboratory under contract no. DE-SC0012704. The work on gpCAM was funded through the Center for Advanced Mathematics for Energy Research Applications (CAMERA), which is jointly funded by the Advanced Scientific Computing Research (ASCR) and Basic Energy Sciences (BES) within the Department of Energy Office of Science, under contract no. DE-AC02-05CH11231. We thank G. Freychet and M. Zhernenkov for assistance at the SMI beamline. **Funding:** This work was funded by U.S. Department of Energy Office of Science, contract nos. DE-SC0012704 and DE-AC02-05CH11231. **Author contributions:** G.S.D. and A.S. fabricated samples. G.S.D., A.S., and K.G.Y. designed experiments and analyzed data. S.B. performed, analyzed, and assisted with interpreting MD simulations. M.M.N. developed the autonomous regression algorithm. K.G.Y. and M.F. assisted with SAXS characterization. The manuscript was written with contributions from all authors. **Competing**

**interests:** K.G.Y. and A.S. are inventors on U.S. Patent 10,126,652 B2, assigned to Brookhaven Science Associates LLC, that covers the selective DSA approach introduced in reference (23) and used in this report. The authors declare that they have no other competing interests. **Data and materials availability:** All data needed to evaluate the conclusions in the paper are present in the paper and/or the Supplementary Materials. Additional data related to this paper are available through the Materials Data Facility at DOI: 10.18126/qboh-6fav and DOI: 10.18126/09ow-8g8k.

Submitted 7 June 2022  
Accepted 12 December 2022  
Published 13 January 2023  
10.1126/sciadv.add3687

## Swarm intelligence caused by physical mechanisms

Researchers studied swarm behavior of microswimmers

*Date:* January 13, 2023

*Source:* Universität Leipzig

*Summary:* Seemingly spontaneously coordinated swarm behavior exhibited by large groups of animals is a fascinating and striking collective phenomenon. Experiments conducted on laser-controlled synthetic microswimmers now show that supposed swarm intelligence can sometimes also be the result of simple and generic physical mechanisms. A team of physicists found that swarms of synthetically produced Brownian microswimmers appear to spontaneously decide to orbit their target point instead of heading for it directly.

### FULL STORY

---

Seemingly spontaneously coordinated swarm behaviour exhibited by large groups of animals is a fascinating and striking collective phenomenon. Experiments conducted by researchers at Leipzig University on laser-controlled synthetic microswimmers now show that supposed swarm intelligence can sometimes also be the result of simple and generic physical mechanisms. A team of physicists led by Professor Frank Cichos and Professor Klaus Kroy found that swarms of synthetically produced Brownian microswimmers appear to spontaneously decide to orbit their target point instead of heading for it directly. They have just published their findings in the journal *Nature Communications*.

"Scientific research on herd and flock behaviour is usually based on field observations. In such cases, it is usually difficult to reliably record the internal states of the herd animals," Kroy said. As a result, the interpretation of observations frequently relies on plausible assumptions as to which individual behavioural rules are necessary for the complex collective groups under observation. Researchers at Leipzig University therefore developed an experimental model system of microswimmers that elicits properties of natural swarm intelligence and provides complete control over the individuals' internal states, strategies, and transformation of signal perception into a navigational reaction.

Thanks to a sophisticated laser heating system (see image), the colloidal swimmers, which are visible only under the microscope, can actively self-propel in a water container by a kind of "thermophoretic self-propulsion" while their travel is permanently disturbed in a random manner by Brownian motion. "Apart from Brownian random motion, which is ubiquitous in microphysics, the experimental set-up provides complete control over the physical parameters and navigation rules of the individual colloidal swimmers and allows long-term observations of swarms of variable sizes," Cichos said.

According to Cichos, when just a very simple and generic navigation rule is followed identically by all of the swimmers, a surprisingly complex swarm behaviour results. For example, if the swimmers are aiming at the same fixed point, instead of them gathering at the same place a kind of carousel can form. Similar to satellites or atomic electrons, the swimmers then orbit their attractive centre on circular paths of varying

heights. The only "intelligent" behavioural rule required for this is that the self-propulsion responds to environmental perception with a certain time delay, which usually occurs in natural swarm phenomena from mosquito dances to road traffic anyway. It turns out that such a "delayed" effect alone is sufficient to form complex dynamic patterns such as the carousel described above. "Physically speaking, each individual swimmer can spontaneously break the radial symmetry of the system and go into circular motion if the product of the delayed time and swimming speed is large enough," Kroy said. In contrast, the orbits of larger swarms and their synchronisation and stabilisation depend on additional details such as the steric, phoretic and hydrodynamic interactions between the individual swimmers.

Since all signal-response interactions in the living world occur in a time-delayed manner, these findings should also further the understanding of dynamic pattern formation in natural swarm ensembles. The researchers deliberately chose primitive and uniform navigation rules for their experiment. This allowed them to develop a stringent mathematical description of the observed phenomena. In the analysis of the delayed stochastic differential equations used for this purpose, the delay-induced effective synchronisation of the swimmers with their own past turned out to be the key mechanism for the spontaneous circular motion. To a large extent, the theory allows us to mathematically predict the experimental observations. "All in all, we have succeeded in creating a laboratory for swarms of Brownian microswimmers. This can serve as a building block for future systematic studies of increasingly complex and possibly still unknown swarm behaviour, and it may also explain why puppies often circle their food bowl when they are being fed," Cichos said.

#### Story Source:

Materials provided by **Universität Leipzig**. Original written by Susann Huster. *Note: Content may be edited for style and length.*

---

#### Journal Reference:

1. Xiangzun Wang, Pin-Chuan Chen, Klaus Kroy, Viktor Holubec, Frank Cichos. **Spontaneous vortex formation by microswimmers with retarded attractions**. *Nature Communications*, 2023; 14 (1) DOI: 10.1038/s41467-022-35427-7

---

#### Cite This Page:

MLA	APA	Chicago
-----	-----	---------

---

Universität Leipzig. "Swarm intelligence caused by physical mechanisms: Researchers studied swarm behavior of microswimmers." ScienceDaily. ScienceDaily, 13 January 2023. <[www.sciencedaily.com/releases/2023/01/230113145348.htm](http://www.sciencedaily.com/releases/2023/01/230113145348.htm)>.

# Spontaneous vortex formation by microswimmers with retarded attractions

Received: 2 August 2022

Accepted: 2 December 2022

Published online: 04 January 2023

 Check for updatesXiangzun Wang<sup>1</sup>, Pin-Chuan Chen<sup>2</sup>, Klaus Kroy<sup>2</sup>, Viktor Holubec<sup>3</sup> & Frank Cichos<sup>1</sup> ✉

Collective states of inanimate particles self-assemble through physical interactions and thermal motion. Despite some phenomenological resemblance, including signatures of criticality, the autonomous dynamics that binds motile agents into flocks, herds, or swarms allows for much richer behavior. Low-dimensional models have hinted at the crucial role played in this respect by perceived information, decision-making, and feedback, implying that the corresponding interactions are inevitably retarded. Here we present experiments on spherical Brownian microswimmers with delayed self-propulsion toward a spatially fixed target. We observe a spontaneous symmetry breaking to a transiently chiral dynamical state and concomitant critical behavior that do not rely on many-particle cooperativity. By comparison with the stochastic delay differential equation of motion of a single swimmer, we pinpoint the delay-induced effective synchronization of the swimmers with their own past as the key mechanism. Increasing numbers of swimmers self-organize into layers with pro- and retrograde orbital motion, synchronized and stabilized by steric, phoretic, and hydrodynamic interactions. Our results demonstrate how even most simple retarded interactions can foster emergent complex adaptive behavior in small active-particle ensembles.

Ordered dynamical phases of motile organisms are ubiquitous in nature across all scales<sup>1</sup>, from bacterial colonies to insect swarms, and bird flocks<sup>2</sup>. In particular, self-organization into vortex patterns is often observed and has been attributed to some local external attractor, e.g., light or nutrient concentration, together with behavioral rules like collision avoidance and mutual alignment<sup>3</sup>. The pertinent social interactions are commonly thought to be based on perception<sup>4–6</sup> and the ability to actively control the direction of motion<sup>3</sup>. They are also generally presumed to provide some benefits to the individual and to the collective, as in the case of collision avoidance or predator evasion<sup>7,8</sup>. However, since such interactions are usually derived only indirectly and approximately from observations<sup>9</sup>, it is arguably useful to coarse grain them, e.g., into simple alignment rules, in order to rationalize the collective effects with the help of simple mechanistic models, in particular with respect to their emerging universal

traits<sup>3,10–12</sup>. This strategy has been successful in physics and is also supported by the observation that biological collectives often appear highly susceptible to environmental influences and exhibit a dynamical finite-size scaling reminiscent of critical states in inanimate many-body assemblies<sup>13–16</sup>.

Importantly, the cascades of complex biochemical/biophysical processes<sup>17,18</sup> needed to transform signal perception into a navigational reaction inevitably result in retarded interactions upon coarse-graining<sup>19</sup> (cf. supplementary Table S1). This generic complication is often dismissed in the analysis, and dedicated models and experiments addressing the role of time delays in the active matter are still rare<sup>20–23</sup>, although these have occasionally been shown to fundamentally alter the collective dynamics<sup>21</sup> and to bring it closer to that found in nature<sup>24</sup>. To a first approximation, delay effects can resemble inertial corrections to an otherwise overdamped biological dynamics<sup>25</sup>. In particular,

<sup>1</sup>Peter Debye Institute for Soft Matter Physics, Leipzig University, 04103 Leipzig, Germany. <sup>2</sup>Institute for Theoretical Physics, Leipzig University, Postfach 100 920, 04009 Leipzig, Germany. <sup>3</sup>Department of Macromolecular Physics, Faculty of Mathematics and Physics, Charles University, 18000 Prague, Czech Republic. ✉e-mail: [cichos@physik.uni-leipzig.de](mailto:cichos@physik.uni-leipzig.de)

both have the propensity to give rise to oscillations and inertia, moreover, to rotational motion around an attractive center, as familiar from planetary orbits.

Experiments that can assess or even deliberately control retarded interactions in living systems turn out to be difficult. But by imposing time delays onto synthetic active particles via computer-controlled laser activation we can create an ideal laboratory system to experimentally emulate such situations. Suitable feedback control techniques for active particles have recently become available through photon nudging<sup>26</sup>. The technique allows to adjust a particle's propulsion speed to acquire real-time information (positions and directions of motion) about the dynamical state of an ensemble. It has previously been employed to rectify the rotational Brownian motion for particle steering and trapping<sup>27</sup>, to explore orientation-density patterns in activity landscapes<sup>28</sup>, and to study information flow between active particles<sup>23</sup>, and their emerging critical states<sup>29,30</sup>. Beyond what related computer simulations accomplish<sup>31–33</sup>, these experiments additionally incorporate the full real-world complexity arising from actual physical interactions due to hydrodynamic, thermal, or concentration fields. In the following, we describe experiments with feedback-controlled active Brownian microswimmers aiming at a fixed target by a retarded thermophoretic self-propulsion. The systematic navigational errors resulting from the retardation are seen to cause a spontaneous symmetry breaking to a bi-stable dynamical state, in which the swimmers self-organize into a merry-go-round motion that switches transiently between degenerate chiralities.

## Results

### Single-particle retarded interaction

The elementary component of a swarm is a single active particle whose direction of motion depends dynamically on its environment. Even small fluctuations of the particle position and orientation render any prospective active motion based on the perception of the environment inaccurate, due to the inevitable finite perception–action delay. In the most symmetric setup, an active particle moves toward a target

position, which is occupied by an immobile particle of the same size in our experiments. Assuming that the active particle responds to the environment that was perceived a delay time  $\delta t$  earlier, its propulsion direction  $\hat{\mathbf{u}}(t)$  at time  $t$  is determined by its relative position to the target particle at time  $t - \delta t$  in the past, according to

$$\hat{\mathbf{u}}(t) = \frac{-\mathbf{r}(t - \delta t)}{|\mathbf{r}(t - \delta t)|}, \quad (1)$$

where  $\mathbf{r}$  is the location of the active particle with respect to the target particle's center. We implemented this interaction rule in an experimental feedback system that controls the active particles' self-propulsion. Our active particles are polymer spheres of radius  $a = 1.09 \mu\text{m}$ , decorated with gold nanoparticles and suspended in a thin film of water. Laser light with a wavelength of 532 nm is focused at distance  $d$  from the active particle center (Fig. 1A). The resulting excentric heating excites an osmotic flow that lets the particle swim with a speed  $v_0$  in the direction defined by Eq. (1)<sup>34</sup>. A darkfield microscopy setup is used to image the particles (Fig. 1B). A computer analyzes and records the positions of the particles and then controls the laser position accordingly via an acousto-optic deflector. We use a separate calibrator particle running on a quadratic trajectory as a reference for the speed  $v_0$  attained by a free swimmer. Further details are described in Sec. 2 of the Supplementary Information.

If  $\delta t = 0$  s, the active particle moves towards the target particle until it collides with it. Further motion of the active particle is then constrained by the presence of the fixed target sphere, resulting in a diffusive motion around it, at a fluctuating distance consistent with the barometer formula<sup>35,36</sup>. As the delay  $\delta t$  increases, the diffusive motion induces a stochastic “error” component due to the increasingly misaligned self-propulsion. Once a critical delay is reached, the particle begins to orbit around the target (see Supplementary Movies 1–3). We quantify this dynamics by the angle  $\theta$  between the direction of motion in Eq. (1) and the instantaneous negative radial direction  $-\mathbf{r}(t)$  (see Fig. 2A). The angle  $\theta$  itself or  $\sin(\theta)$  can serve as an indicator for

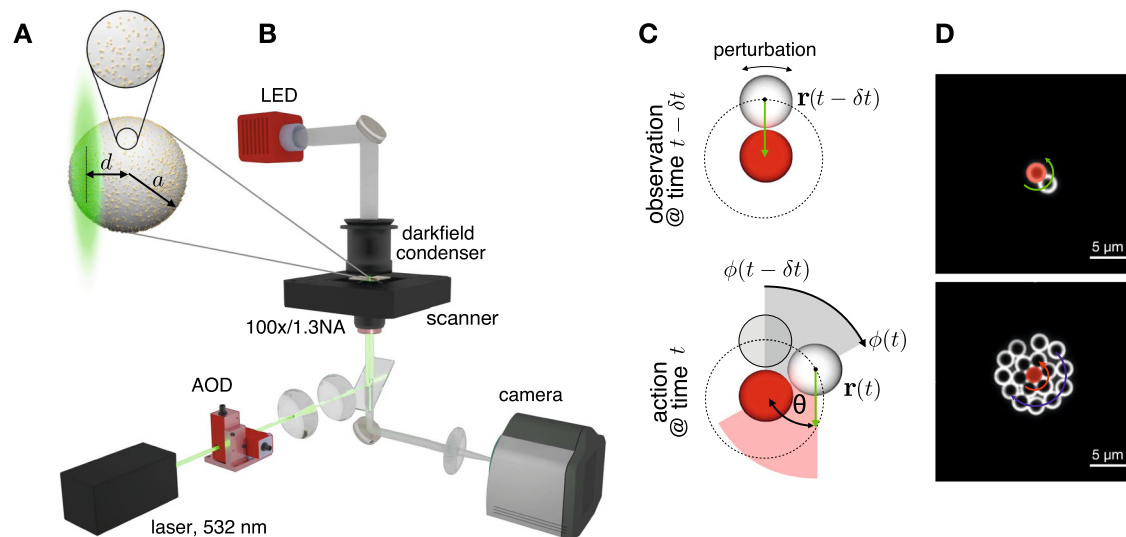


**Fig. 1 | Experimental realization.** **A** Particles used in the experiments consist of a melamine resin colloid ( $2.18 \mu\text{m}$  in diameter) with 8 nm gold nanoparticles scattered across the surface (covering up to 10% of the total surface area). A 532 nm laser focused at the edge of the particle at a distance  $d$  from its center induces a self-thermophoretic motion and allows for precise control of the propulsion direction. Importantly, optical forces are weak so the particles exhibit a truly self-phoretic autonomous motility, making them proper microswimmers. **B** Experimental setup used to image the particles by darkfield microscopy (LED, darkfield condenser, and camera) and guide their motion by sequential beam steering of the laser on the

sample plane with a two-axis acousto-optic deflector (AOD). All particles in the field of view are addressed during each exposure period of the camera. **C** The interaction rule for the delayed attraction of a single active particle (white sphere) towards a target (red sphere) is split into an observation made at a time  $t - \delta t$  that sets the direction of motion for the self-propulsion step exerted after a programmed delay time  $\delta t$ . The green arrows indicate the planned motion  $-\mathbf{r}(t - \delta t)$  and its actual realization at time  $t$ . **D** Examples of darkfield microscopy images where a single active particle (top) and 16 active particles (bottom) interact with one target particle (red).

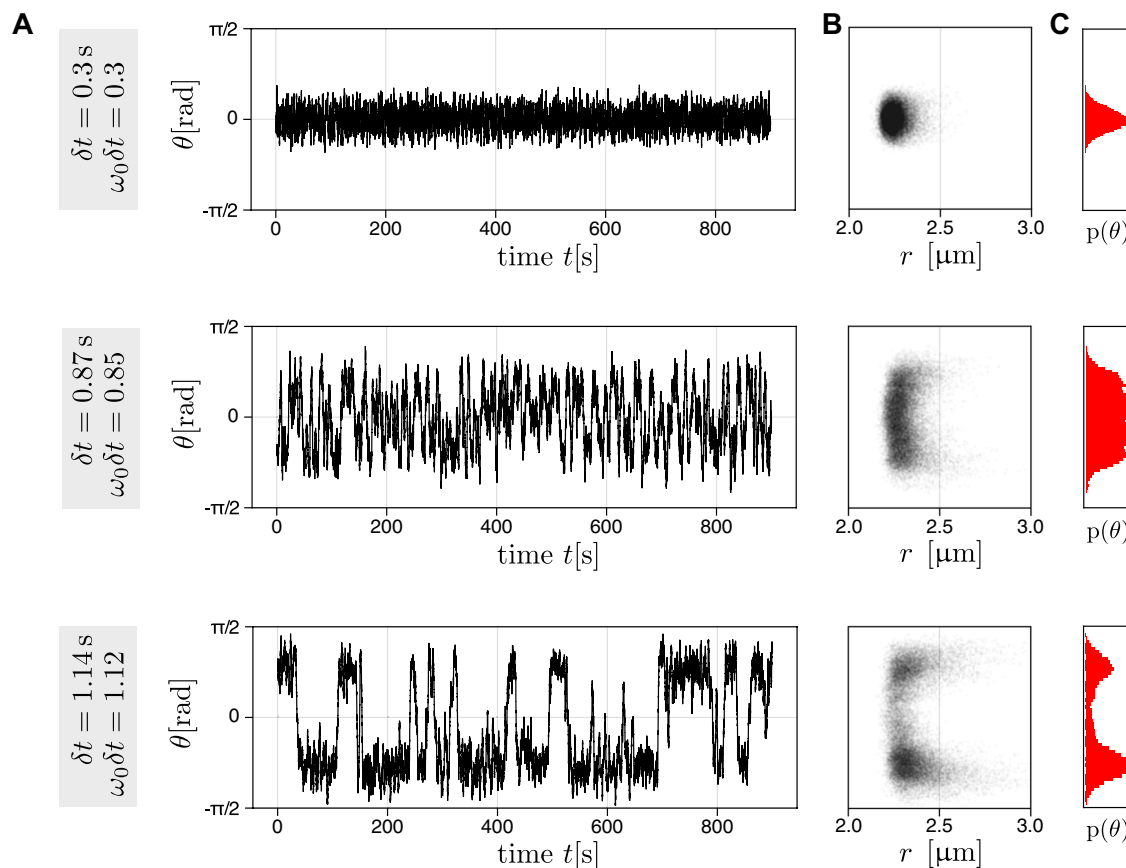


**Fig. 2 | Propulsion angle at the different programmed delay.** **A** Trajectories of the propulsion angle  $\theta(t)$  of an active particle at three different delays (top:  $\delta t = 0.3$  s, middle:  $\delta t = 0.87$  s, and bottom:  $\delta t = 1.14$  s) for its attraction towards a target particle. The velocity of the active particle is  $v_0 = 2.16 \mu\text{m s}^{-1}$ . **B** Propulsion angle  $\theta(t)$

vs. the distance  $|\mathbf{r}(t)|$  of the particle from the target center. **C** Histograms of the propulsion angle over the whole trajectory. The delay for the individual panels in columns (**B**, **C**) is indicated on the left of the corresponding row.

deviations from the “intended” central orientation. Similarly, for many particles, numbered by the index  $i$ , it is useful to define the rotational order parameters  $o_{R,i} = (\hat{\mathbf{r}}_i \times \hat{\mathbf{u}}_i) \cdot \mathbf{e}_z = \sin(\theta_i)^{29,37}$ , where the hats denote vectors normalized to 1 and  $\mathbf{e}_z$  is a unit vector in the direction of  $z$  axis. Figure 2A shows the experimental trajectories of  $\theta$  for a single active particle with  $v_0 = 2.16 \mu\text{m s}^{-1}$  and three different delays. For short delays,  $\theta$  fluctuates with a small amplitude around zero (Fig. 2A top). The fluctuations increase with the delay and lead to a flat-top probability density of the propulsion angle for  $\delta t \approx 0.87$  s (Fig. 2A middle). At larger delays ( $\delta t = 1.14$  s), the propulsion angle fluctuates around a stable nonzero value that changes its sign intermittently (Fig. 2A bottom), corresponding to a bimodal probability density  $p(\theta)$  (Fig. 2C). The periods of consistent chirality increase in duration when the delay is increased further. At  $\delta t = 1.4$  s, the propulsion angle transiently fluctuates around  $\pm 80^\circ$ . Under these conditions, the cohesion of the particle to the target becomes marginal as the typical particle velocity is almost tangential to the target particle circumference. As a result, the distance  $|\mathbf{r}(t)|$  of the particle from the origin starts to fluctuate more strongly, as shown in the position histograms in Fig. 2B.

The net propulsion angle is the result of angular displacements  $\phi(t)$  of the particle position acquired due to the perception–action delay during the period  $[t - \delta t, t]$ :

$$\theta(t) = \int_{t-\delta t}^t \omega(t') dt' = \phi(t) - \phi(t - \delta t) = \angle(\hat{\mathbf{u}}(t), -\mathbf{r}(t)). \quad (2)$$

Here,  $\phi(t)$  is the polar angle of the active particle in polar coordinates centered in the target particle, and we introduced  $\omega(t) = \dot{\phi}(t)$  as its corresponding angular velocity (Fig. 2C). The

observed dynamics can be understood by considering the active particle and the target particle in physical contact. Their distance is then constrained to be the sum of their radii ( $R = 2a = \langle |\mathbf{r}(t)| \rangle$ ) and the active particle slides around the target particle with an angular velocity  $\omega(t) = \omega_0 \sin(\theta(t))$ , where  $\omega_0 = v_0/R$  is the natural angular velocity for tangential propulsion with  $\theta = \pm\pi/2$ . As sketched in Fig. 3A, assuming a constant angular velocity  $\omega$  with  $\theta = \omega\delta t$ , the solutions to the equation for  $\theta$  are given by the intersections of a sine function and a linear function,

$$(\omega_0\delta t)^{-1}\theta = \sin(\theta). \quad (3)$$

For  $\omega_0\delta t < 1$ , there is a single intersection at  $\theta = 0$ , indicating a stable non-rotational state. For  $1 < \omega_0\delta t < \pi/2$ , the non-rotational state becomes unstable and two counter-rotational metastable solutions arise. For  $\omega_0\delta t > \pi/2$ , the rotating solutions correspond to  $|\theta| > \pi/2$ , and the radial component of propulsion becomes positive (repulsive), driving the active particle away from the target particle. As a result, the orbit “takes off” and its radius  $R$  increases until a new stable orbit with  $R = 2v_0\delta t/\pi > 2a$  and  $|\theta| = \pi/2$  is reached. For small particles ( $a \rightarrow 0$ ), the distance of the swimmer to the target position can thus, in principle, vanish ( $R \rightarrow 0$ ), and the rotating orbits can even occur at arbitrarily short programmed delays ( $\delta t \rightarrow 0$ ). Retarded attraction hence always leads to rotational orbital motion with a delay-dependent radius<sup>23</sup>. In the experiment, due to the presence of the fixed central particle, the smallest attainable orbit radius  $R = 2a$  is given by the particle diameter. Adding Brownian fluctuations to the deterministic Eq. (3) results in the nonlinear delayed stochastic differential equation  $\dot{\phi}(t) = \omega_0 \sin(\phi(t) - \phi(t - \delta t)) + \sqrt{2D_0/R^2} \eta(t)$ ,

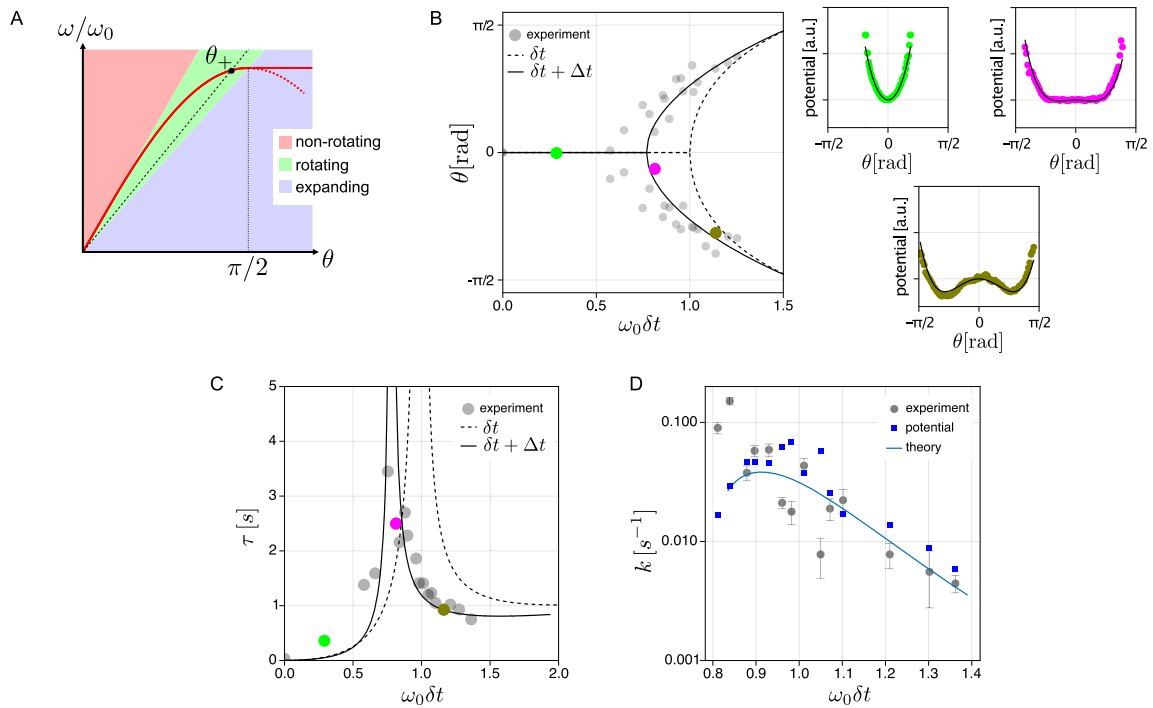


**Fig. 3 | Transition to a rotational dynamical state for a single active particle.**

**A** Graphical construction of condition (3) for a transition from a non-rotational state (red-shaded region) to a rotational state (green-shaded region). The red line ( $\sin \theta$ ) and the black dashed line with slope  $1/(\omega_0 \delta t)$  intersect at several  $\theta$ . The solution  $\theta = \theta_+$  in the green region and its chirally inverse image  $\theta_-$  in the third quadrant (not shown) correspond to co- and counter-clockwise rotation.

**B** Experimentally measured propulsion angles (maxima of the histograms in Fig. 2C) as a function of  $\omega_0 \delta t$ , exhibiting a bifurcation at  $\omega_0 \delta t \approx 0.76$ . The dashed line corresponds to the analytical prediction of the theoretical model (5), neglecting the inevitable instrumental delay  $\Delta t$ . The solid line shows the solution of the refined theoretical model, which includes the instrumental delay  $\Delta t = 64$  ms of our setup in addition to the programmed delay  $\delta t$ . The colored dots indicate the control parameter values studied in Fig. 2 and the linked small color plots show the

corresponding potentials of mean force, determined from the propulsion angle histograms in Fig. 2C, together with a fit of the refined analytical model, including the instrumental delay  $\Delta t$  (see Sec. 2.2 and 3 of Supplementary Information). The only free parameter for fitting is the effective temperature of the system.

**C** Relaxation time  $\tau$  of a single active particle as determined experimentally from the autocorrelation of the propulsion angle fluctuations (Eq. (8), data points). The solid lines correspond to the refined version of the theoretical prediction (Eq. (7)), including the instrumental delay  $\Delta t$  (see Sec. 2.2 of Supplementary Information for details). The colored dots have the same meaning as in panel (B). **D** Transition rates between the two rotational states obtained from the experiments (circles) plotted with the predictions from Kramers' theory, Eq. (9), with a global fit parameter  $D_\theta = 0.05 \text{ s}^{-1}$  (solid line) and  $D_\theta$  fitted to the probability distribution  $p(\theta)$  separately for each value  $\omega_0 \delta t$  (squares). Error bars represent the standard error.

where  $D_0 \approx 0.0642 \mu\text{m}^2 \text{ s}^{-1}$  denotes the translational diffusion coefficient of the active particle and  $\eta(t)$  white noise. To solve this equation, we approximated  $\dot{\phi}(t)\delta t$  by  $\theta(t)$  and expanded the  $\sin(\phi(t) - \phi(t - \delta t))$  in a Taylor series around  $\delta t = 0$  up to the third order in  $\delta t$ . We dropped the term proportional to  $\ddot{\phi}(t)$  to secure the stability of the resulting equation<sup>38</sup> (for details, see Sec. 3 of Supplementary Information). The resulting noise term  $\sqrt{8D_0/(\omega_0 \delta t R)^2}$  turned out to be inaccurate compared to experimental and simulation data. We, therefore, introduce an effective diffusion coefficient  $D_\theta$  as a free parameter in the noise term in Eq. (4) to describe the rotation of the active particle around the target as the angular Brownian motion

$$\dot{\theta} = \frac{1}{3\delta t} [\theta_\pm^2 - \theta^2] \theta + \sqrt{2D_\theta} \eta \quad (4)$$

with

$$\theta_\pm = \pm \sqrt{6 \left( 1 - \frac{1}{\omega_0 \delta t} \right)}. \quad (5)$$

Eq. (4) yields the stationary solutions 0 and  $\theta_\pm$  with the bifurcation point  $\omega_0 \delta t = 1$ , for the transition from a non-rotational to a rotational state. The data points in Fig. 3B display the experimentally obtained maxima of the histograms  $p(\theta)$  of the propulsion angle (see Fig. 2C) as a function of  $\omega_0 \delta t$ . The transition

points in the experiments are located at lower values of the control parameter  $\omega_0 \delta t$ , due to the mentioned instrumental delay  $\Delta t$  in the feedback loop of the experimental setup. This instrumental delay between the most recent exposure to the camera and the laser positioning affects the motion direction beyond the programmed delay  $\delta t$ <sup>34,39</sup>, causing an earlier onset of the transition to a stable rotation. The dashed line in Fig. 3B shows the theoretical prediction, which includes both the instrumental delay  $\Delta t$  and the programmed delay  $\delta t$ , as detailed in the Supplementary Information (Eq. (11)).

The Langevin equation (4) can be interpreted as a dynamical equation for the position  $\theta$  of an overdamped Brownian particle with diffusion coefficient  $D_\theta$  in a quartic potential (see derivation in Sec. 3 of Supplementary Information),

$$U(\theta) = \frac{1}{\delta t} \left[ \left( \frac{1}{\omega_0 \delta t} - 1 \right) \theta^2 + \frac{1}{12} \theta^4 \right], \quad (6)$$

which allows to classify the observed instability of the isotropic state as a normal supercritical pitchfork bifurcation<sup>40</sup>. The potential can also directly be extracted from the experimental data (Fig. 3B) by fitting the histogram  $p(\theta)$  with a (normalized) Boltzmann distribution  $\exp(-U(\theta)/D_\theta)/Z$  at the effective temperature  $D_\theta$ . The effective temperature thus links the measured potential of mean force  $-D_\theta \log p(\theta)$  to Eq. (6).

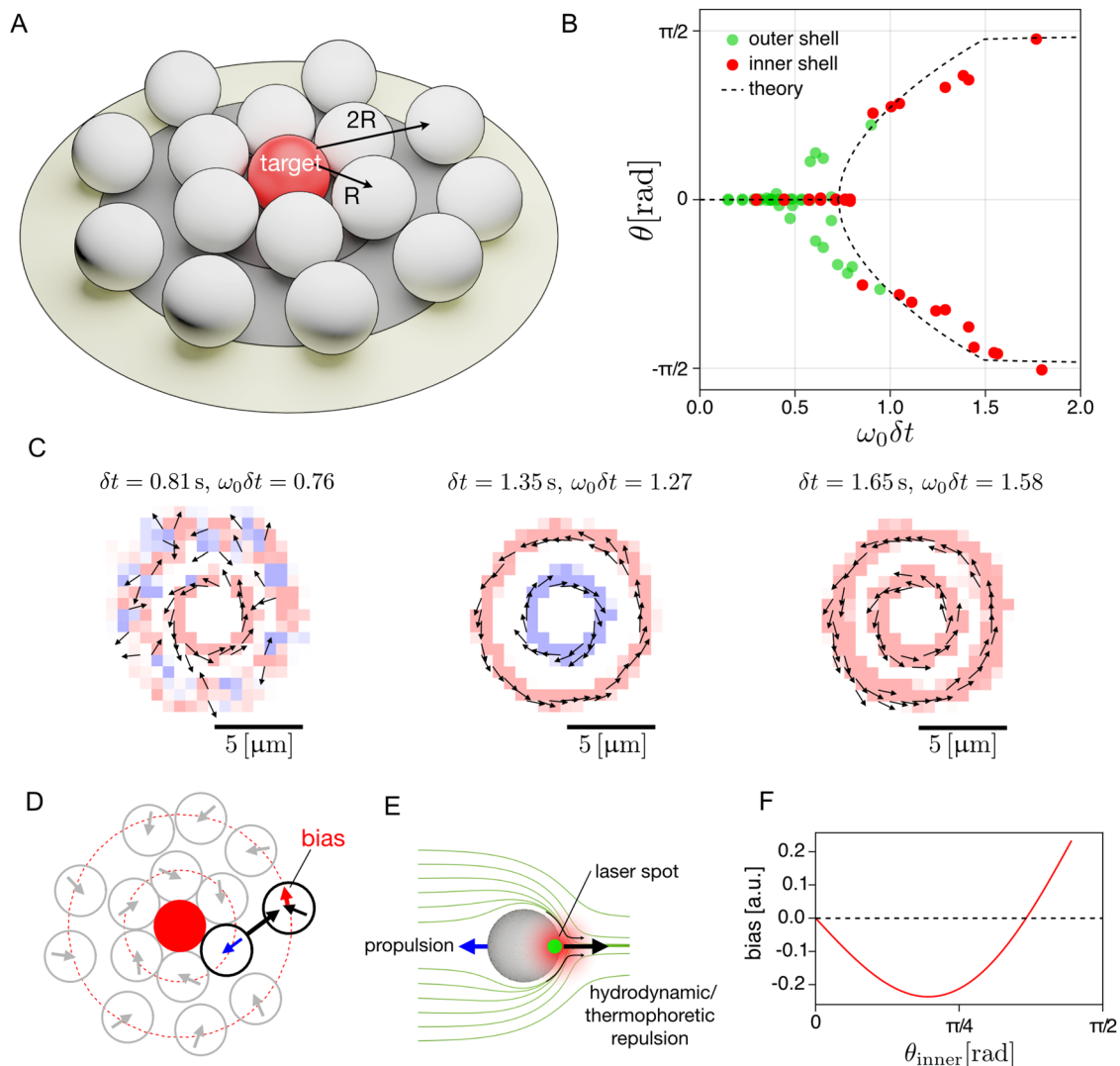


**Fig. 4 | Collective rotation of 15 particles attracted to a single target particle.** **A** Sketch of the shell structure and radii. **B** Bifurcation of the most probable propulsion angle as a function of the control parameter  $\omega_0 \delta t$  for a (calibrator) propulsion speed of  $v_0 = 2.06 \mu\text{m s}^{-1}$ . The red dots are obtained from the inner shell particles at a typical distance of  $R^{\text{in}} = 2.18 \mu\text{m}$ , while the green dots denote the outer shell particles at  $R^{\text{out}} = 4.47 \mu\text{m}$ . The dashed line corresponds to the theoretical single-particle prediction, including the instrumental delay  $\Delta t = 70 \text{ms}$ . **C** Average velocity field of active particles at  $\delta t = 0.81 \text{s}$  when the spontaneous rotation of the inner shell is constantly disrupted by the non-rotating outer shell, at  $\delta t = 1.35 \text{s}$  when the two shells are counter-rotating,

and at  $\delta t = 1.65 \text{s}$  when both shells are co-rotating. The arrows and colors denote the average direction of motion. **D** Snapshot of the active particles and their propulsion directions corresponding to **(C)** at  $\delta t = 1.35 \text{s}$ . The repulsion induced by the flow and temperature fields of the inner shell causes a bias for the outer shell rotation. **E** Sketch of the flow and temperature fields induced by the laser (green dot) around an active particle, and the resulting repulsion. **F** Schematic sketch of the presumed magnitude of the bias caused by the temperature and flow fields on the rotation of the outer shell, as a function of the propulsion angle  $\theta^{\text{in}}$  of the inner shell particles (see Sec. 5 of Supplementary Information).

The latter resembles the Landau free energy at a second-order phase transition<sup>41</sup>. For readers familiar with this framework, this mathematical analogy allows to shortcut the following analysis, the details of which are given in Sec. 3 of the Supplementary Information. Note, however, that we are not discussing a thermodynamic phase transition but merely a dynamical bifurcation, here. The bifurcation and its potential energy landscape are not due to strong many-particle couplings, but to the interaction of the single active particle with its own past image. In Landau's theory, the control parameter  $1 - \omega_0 \delta t$  maps onto the dimensionless distance to the critical temperature. Both the activity  $\omega_0$  and the delay  $\delta t$  favor the transition to the symmetry-broken state. Hence, at high propulsion speeds, already short delays can give rise to rotating orbits. The inverse of the second derivative of  $U(\theta)$ , corresponding to the static susceptibility in Landau theory, gives

the time  $\tau$  (Eq. (7)) to relax in the (meta-)stable states,

$$\tau = \begin{cases} \frac{\delta t}{2} \left( \frac{1}{\omega_0 \delta t} - 1 \right)^{-1} & \omega_0 \delta t < 1 \\ -\frac{\delta t}{4} \left( \frac{1}{\omega_0 \delta t} - 1 \right)^{-1} & \omega_0 \delta t > 1. \end{cases} \quad (7)$$

We determine  $\tau$  experimentally via  $C(\tau)$  from the autocorrelation function,

$$C(\tau) = \frac{\langle \delta\theta(t' + \tau) \delta\theta(t) \rangle_{t'}}{\langle \delta\theta(t')^2 \rangle_{t'}} \quad (8)$$

of fluctuations of the propulsion angle  $\delta\theta(t) = \theta(t) - \langle \theta(t) \rangle$ , as  $C(\tau) = 1/e$  (Fig. 3C). The experimental data (circles) is compared to Eq. (7) (dashed line), and to an improved model prediction (solid line) that

also takes into account the inevitable instrumental delay  $\Delta t$ , as discussed in Sec. 3 of the Supplementary Information. The critical slowing down of the relaxation due to an increasingly flat potential close to the transition point at  $\omega_0 \delta t = 1$ , corresponding to the potential plot in the middle of Fig. 3B, is thereby nicely confirmed, without any free parameter.

While the rotational orbits can be inferred from a purely deterministic model excluding Brownian motion, the observed spontaneous reversal of the chirality is driven by fluctuations in the propulsion angle and, thus, by the (non-equilibrium) noise in the system. It corresponds to transitions between the minima  $\pm\theta_{\pm}$  of the virtual potential, Eq. (6). We may thus apply Kramers' theory to estimate the corresponding transition rate as

$$k = \frac{\sqrt{2} |\omega_0 \delta t - 1|}{\pi \omega_0 \delta t^2} \exp \left[ -\frac{3}{\delta t D_{\theta}} \left( \frac{1}{\omega_0 \delta t} - 1 \right)^2 \right]. \quad (9)$$

The effective temperature  $D_{\theta}$  driving the fluctuations in the virtual potential is treated as a fit parameter. Figure 3D displays the experimentally measured transition rates, obtained from the observed mean residence times of  $\theta$  in the two potential wells. They are in good agreement with Eq. (9), despite the hybrid equilibrium/non-equilibrium origin of the noisy dynamics.

### Multiple particles

As demonstrated in the previous section, the rotation observed in our experiments results from a spontaneous symmetry breaking in the dynamics of a single active particle. It originates from the particle's retarded self-propulsion to a target, which differs from standard explanations of rotational dynamics in overdamped systems, which usually blame mutual ("social") interactions between multiple agents<sup>3,9,12,42</sup>. As we demonstrate in Fig. S9B, when adding up to five more active particles to the system, each of them exhibits the same rotation and bifurcation as a single swimmer. Steric, hydrodynamic, and thermophoretic interactions among the particles then synchronize and stabilize their motion, aligning their sense of rotation. So the system exhibits collective behavior, but the dynamical symmetry breaking to a chiral dynamical state is not primarily due to the mutual interactions.

Somewhat larger numbers of particles organize into multiple rotating shells. Figure 4 summarizes the key results obtained for an ensemble of 15 active particles attracted to the target particle with the same programmed and intrinsic delays  $\delta t$  and  $\Delta t$ , respectively. For the considered range of time delays, the active particles form two tightly packed shells around the target particle (Fig. 4A). The typical distance of the inner shell particles to the target is about half that of the outer shell,  $R^{\text{out}} \approx 2R^{\text{in}} = 4a$ . So based on the single-particle picture alone, the particles in the inner and outer shells swimming at the same speed would be expected to start rotating at different delays. However, in reality, the inter-particle interactions in the compact cluster strongly correlate with the particle motion and quantitatively change the picture. Compared to the theoretical prediction,  $\omega_0 \delta t = 0.73$ , we observe that for  $v_0 = 2.06 \mu\text{m s}^{-1}$  the transition to the rotational phase of the inner shell is postponed to  $\omega_0^{\text{in}} \delta t \equiv v_0 \delta t / R^{\text{in}} \approx 0.83$ , corresponding to  $\delta t = 0.9$  s (see the rightmost red data point lying on the horizontal axis in Fig. 4B). Slightly below the transition, the inner shell exhibits alternating periods of rotational and stationary states. Meanwhile, the stationary outer shell compresses the inner shell due to its inwards-pointing propulsion direction (Fig. 4C, left). Figure. 4C displays the velocity fields of the particles averaged over their trajectories with three different delays. The bifurcation for the outer shell is located at  $\omega_0^{\text{out}} \delta t \equiv v_0 \delta t / R^{\text{out}} \approx 0.41$ , which corresponds to the same value  $\delta t = 0.9$  s of the delay at which the inner shell undergoes its bifurcation to the rotational state (see Fig. 4B and Supplementary Movies S4–S6). For delays slightly above the transition,  $0.9 \text{ s} < \delta t < 1.41 \text{ s}$ , the two shells rotate in opposite directions, as shown in the middle plot of Fig. 4C.

The simultaneous transition and the counter-rotation of the two shells suggest that the inner shell particles generate backflows opposite to their propulsion direction, thereby repelling the outer shell particles and facilitating their transition to the rotational state, as schematically depicted in Fig. 4D–F. These backflows are presumably caused by the directional hydrodynamic and thermophoretic interactions. The surface temperature gradient across each particle creates a thermosmotic surface flow that propels the particle<sup>43</sup>. If the particle motion is opposed by an external force, such as the steric force due to the immobilized target particle, the slowed-down particle acts as a pump, creating a hydrodynamic outflow at its hot side (Fig. 4D and Sec. 2.5 and 5.2 of Supplementary Information). Furthermore, thermophoretic interactions arise from temperature gradients across the surface of a particle caused by its neighbors<sup>33</sup>. These are commonly repulsive, as found, e.g., for Janus particles in external temperature gradients<sup>33</sup>. We have carried out finite element simulations of the flow field around a mobile and an immobile self-propelling swimmer (see Sec. 2.5 of Supplementary Information). The overall near-field hydrodynamic interactions are found to be quite complex, due to many interacting particles and the nearby substrate surface<sup>44–46</sup>. They also depend on the propulsion angle  $\theta$ . An increasing innershell propulsion angle results in a changing direction and magnitude of the rotational bias onto the outer shell, which presumably varies as sketched in Fig. 4F (see Sec. 5 of Supplementary Information). As a result, for  $\delta t \geq 1.41$  s, the two shells predominantly rotate in the same sense, as shown in Fig. 4C, right. The transition from counter- to co-rotation shells corresponds to the sign flip of the bias at  $\theta^{\text{in}} \approx 67^\circ$ . At even longer delays,  $\theta^{\text{in}}$  tends to reach  $90^\circ$ , and thus the inner shell tries to take off and expand against the compression exerted by the outer shell. These competing tendencies lead to particle exchange between the two shells. While we currently cannot separate thermophoretic and hydrodynamic effects in the experiment, hydrodynamic interactions may be expected to be more important here than for a single free particle in a temperature gradient: firstly, due to the collective character of the dynamics, and secondly, due to the pump effect caused by the partial blocking of the self-phoretic motion of the individual swimmers (see Sec. 2.5 and 5.2 of Supplementary Information). These features could provide a link between our experiments and the swarming observed in bacterial colonies<sup>47,48</sup>.

### Discussion

We have demonstrated above that the motion of an active particle induced by the delayed attraction to a target point can spontaneously undergo a transition from a diffuse isotropic "barometric" state to a dynamical chiral state, upon increasing the activity and/or the delay time. The transition is well described by a pitchfork bifurcation accompanied by a characteristic critical slowing down of the response<sup>40</sup>. Similar to certain mechanical analogs<sup>49</sup>, the single-particle dynamics thus already exhibit non-trivial features more commonly associated with (mean-field) phase transitions in strongly interacting passive many-body systems. This can be explained by noting that the deterministic part,  $\dot{\phi}(t) = \omega_0 \sin(\phi(t) - \phi(t - \delta t))$ , of our stochastic delay differential equation can also be understood as the dynamical equation for a single Kuramoto phase oscillator<sup>50,51</sup>, with vanishing eigenfrequency and coupling strength  $\omega_0$ , which is trying to synchronize with its own past state. In the chiral state, the particle orbits around the target point (the central obstacle is optional). The orbiting motion is stable against noise, but its sense of rotation is only transiently maintained. This should be contrasted with the chiral states resulting from non-reciprocal coupling in the time-local Kuramoto model (without delay), as discussed by ref. 52, which hinges on the stabilization by many-body cooperativity. Based on our results, we suggest that for the single retarded oscillator, the infinite number of relaxation modes encoded in the time-delayed equation of motion play a similar role<sup>53,54</sup>.

As we have shown, the nonlinear dynamics of our experimental system can be described by an approximate analytical model, which explains the emergence of a self-generated quartic virtual potential. While such potentials are frequently found in descriptions of phase transitions and collective effects in active-particle ensembles, following various behavioral rules<sup>29,30</sup>, we reiterate that the mechanism is a different one, here. Due to the activity and the (programmed) delay, it already occurs for a single active particle aiming at a spatially fixed target. In a whole swarm of particles that are all attracted to a common target, which might be its own perceived center of mass, the single-particle bifurcation is preserved. Inter-particle collisions merely synchronize, renormalize, and stabilize the rotational states of the individual particles. Upon close contact, hydrodynamic and thermophoretic interactions become important and help the swimmers to self-organize into co- and counter-rotating orbits. In biological motile ensembles, from bacteria to fish, similar hydrodynamic mechanisms may be at work, although precise details and scales may differ widely<sup>45,55–57</sup>. The corresponding many-body effects can be subtle and may elude coarse-grained simulations and theories. This underscores the importance of well-controlled experimental model systems that may act as “hybrid simulations”, combining computer-controlled active particles with real-world environments.

To conclude, while time delays are an unavoidable outcome of coarse-graining microscopic descriptions of the feedback processes in natural systems (cf. Table S1), they are often neglected in low-dimensional models of active particle collective effects<sup>5,10</sup>. In this respect, our model system provides a new perspective, as it takes the unavoidable systematic delays in the dynamics seriously and explores their generic effects. We find that, in overdamped systems, retardation plays a similar role as added inertia. Both effects lead to persistence and associated “aiming errors” in particle dynamics. In this sense, our analysis can provide a template for an entire class of motile ensembles exhibiting spontaneous rotational dynamics caused by aiming errors—as such, are associated with microswimmer navigation strategies employing “vision-cone”<sup>29,30</sup> or “acceptance-angle”<sup>27,36</sup> criteria. In fact, the effects of the time delay may be even richer<sup>20,24,54</sup>. While we considered only a positive delay, i.e., synchronization with the past, above, sophisticated biological organisms also possess predictive capabilities to extrapolate the current state into the future<sup>58,59</sup>. These can, to a first approximation, be incorporated in the form of a negative time delay. The inclusion of positive and negative delays may therefore provide a new, “more physical” perspective on phenomenologically extracted, rather sophisticated rules like collision avoidance and alignment interactions, commonly postulated as sources of emerging complex adaptive responses in living many-body systems.

## Methods

### Sample preparation

Samples were prepared using two glass coverslips (20 mm × 20 mm, 24 mm × 24 mm) to confine a thin liquid layer (3 μm thickness) in between. The edges of one coverslip are sealed with a thin layer of PDMS (polydimethylsiloxane) to prevent leakage and evaporation. The liquid film used in the sample is composed of 2.19-μm-diameter gold-coated melamine formaldehyde (MF) particles (microParticles GmbH) dispersed in 0.1% Pluronic F-127 solution. The latter prevents the cohesion of the particles and adsorption to the cover slide surface. The surface of the MF particles is speckled uniformly with gold nanoparticles of about 8 nm diameter with a total surface coverage of about 10% (Fig. S3A). SiO<sub>2</sub> particles (2.96 μm in diameter, microParticles GmbH) are added into the solution to keep the thickness of the liquid layer at about 3 μm. Finally, 0.3 μl of the mixed particle suspension is pipetted on one of the coverslips, for which the other serves as a lid.

### Experimental setup

The experimental setup (see Sec. 2 of Supplementary Information) consists of an inverted microscope (Olympus, IX71) with a mounted piezo translation stage (Physik Instrumente, P-733.3). The sample is illuminated with an oil-immersion darkfield condenser (Olympus, U-DCW, NA 1.2–1.4) and a white-light LED (Thorlabs, SOLIS-3C). The scattered light is imaged by an objective lens (Olympus, UPlanApo × 100/1.35, Oil, Iris, NA 0.5–1.35) and a tube lens (250 mm) to an EMCCD (electron-multiplying charge-coupled device) camera (Andor, iXon DV885LC). The variable numerical aperture of the objective was set to a value below the minimum aperture of the darkfield condenser.

The microparticles are heated by a focused, continuous-wave laser at a wavelength of 532 nm (CNI, MGL-III-532). The beam diameter is increased by a beam expander and sent to an acousto-optic deflector (AA Opto-Electronic, DTSXY-400-532) and a lens system to steer the laser focus in the sample plane. The deflected beam is directed towards the sample by a dichroic beam splitter (D, Omega Optical, 560DRLP) and focused by an oil-immersion objective (Olympus, UPlanApo × 100/1.35, Oil, Iris, NA 0.5–1.35) to the sample plane ( $w_0 \approx 0.8 \mu\text{m}$  beam waist in the sample plane). A notch filter (Thorlabs, NF533-17) is used to block any remaining back reflections of the laser from the detection path. The acousto-optic deflector (AOD), as well as the piezo stage, are driven by an AD/DA (analog-digital/digital-analog) converter (Jäger Messtechnik, ADwin-Gold II). A LabVIEW program running on a desktop PC (Intel Core i7 2600 4 × 3.40 GHz CPU) is used to record and process the images as well as to control the AOD feedback via the AD/DA converter.

### Data availability

All data in support of this work is available in the manuscript or the Supplementary Information. Further data and materials are available from the corresponding author upon request.

### References

1. Kauffman, S. *The Origins of Order: Self-organization and Selection in Evolution* (Oxford Univ. Press, 1993).
2. Vicsek, T. & Zafeiris, A. Collective motion. *Phys. Rep.* **517**, 71–140 (2012).
3. Delcourt, J., Bode, N. W. F. & Denoël, M. Collective vortex behaviors: diversity, proximate, and ultimate causes of circular animal group movements. *Q. Rev. Biol.* **91**, 1–24 (2016).
4. Strandburg-Peshkin, A. et al. Visual sensory networks and effective information transfer in animal groups. *Curr. Biol.* **23**, R709–R711 (2013).
5. Pearce, D. J. G., Miller, A. M., Rowlands, G. & Turner, M. S. Role of projection in the control of bird flocks. *Proc. Natl. Acad. Sci. USA* **111**, 10422–10426 (2014).
6. Cremer, J. et al. Chemotaxis as a navigation strategy to boost range expansion. *Nature* **575**, 658–663 (2019).
7. Couzin, I. D. & Krause, J. Self-organization and collective behavior in vertebrates. *Adv. Study Behav.* **32**, 1–75 (2003).
8. Ioannou, C. C., Guttal, V. & Couzin, I. D. Predatory fish select for coordinated collective motion in virtual Prey. *Science* **337**, 1212–1215 (2012).
9. Berdahl, A. M. et al. Collective animal navigation and migratory culture: from theoretical models to empirical evidence. *Philos. Trans. R. Soc. B Biol. Sci.* **373**, 20170009 (2018).
10. Vicsek, T., Czirók, A., Ben-Jacob, E., Cohen, I. & Shochet, O. Novel type of phase transition in a system of self-driven particles. *Phys. Rev. Lett.* **75**, 1226–1229 (1995).
11. Hemelrijk, C. K. & Hildenbrandt, H. Some causes of the variable shape of flocks of birds. *PLoS ONE* **6**, e22479 (2011).
12. Costanzo, A. & Hemelrijk, C. K. Spontaneous emergence of milling (vortex state) in a Vicsek-like model. *J. Phys. D Appl. Phys.* **51**, 134004 (2018).

13. Cavagna, A. et al. Scale-free correlations in starling flocks. *Proc. Natl. Acad. Sci. USA* **107**, 11865–11870 (2010).
14. Mora, T. & Bialek, W. Are biological systems poised at criticality? *J. Stat. Phys.* **144**, 268–302 (2011).
15. Muñoz, M. A. Colloquium: criticality and dynamical scaling in living systems. *Rev. Mod. Phys.* **90**, 031001 (2018).
16. Cavagna, A. et al. Dynamic scaling in natural swarms. *Nat. Phys.* **13**, 914–918 (2017).
17. Kim, D. W., Hong, H. & Kim, J. K. Systematic inference identifies a major source of heterogeneity in cell signaling dynamics: the rate-limiting step number. *Sci. Adv.* **8**, eabl4598 (2022).
18. Zhang, J. & Zhou, T. Markovian approaches to modeling intracellular reaction processes with molecular memory. *Proc. Natl. Acad. Sci. USA* **116**, 23542–23550 (2019).
19. More, H. L. & Donelan, J. M. Scaling of sensorimotor delays in terrestrial mammals. *Proc. R. Soc. B Biol.* **285**, 20180613 (2018).
20. Mijalkov, M., McDaniel, A., Wehr, J. & Volpe, G. Engineering sensorial delay to control phototaxis and emergent collective behaviors. *Phys. Rev. X* **6**, 1–16 (2016).
21. Forgoston, E. & Schwartz, I. B. Delay-induced instabilities in self-propelling swarms. *Phys. Rev. E* **77**, 035203 (2008).
22. Piwowarczyk, R., Selin, M., Ihle, T. & Volpe, G. Influence of sensorial delay on clustering and swarming. *Phys. Rev. E* **100**, 012607 (2019).
23. Khadka, U., Holubec, V., Yang, H. & Cichos, F. Active particles bound by information flows. *Nat. Commun.* **9**, 3864 (2018).
24. Holubec, V., Geiss, D., Loos, S. A. M., Kroy, K. & Cichos, F. Finite-size scaling at the edge of disorder in a time-delay vicsek model. *Phys. Rev. Lett.* **127**, 258001 (2021).
25. Attanasi, A. et al. Information transfer and behavioural inertia in starling flocks. *Nat. Phys.* **10**, 615–698 (2014).
26. Qian, B., Montiel, D., Bregulla, A., Cichos, F. & Yang, H. Harnessing thermal fluctuations for purposeful activities: The manipulation of single micro-swimmers by adaptive photon nudging. *Chem. Sci.* **4**, 1420–1429 (2013).
27. Bregulla, A. P., Yang, H. & Cichos, F. Stochastic localization of microswimmers by photon nudging. *ACS Nano* **8**, 6542–6550 (2014).
28. Söker, N. A., Auschra, S., Holubec, V., Kroy, K. & Cichos, F. How activity landscapes polarize microswimmers without alignment forces. *Phys. Rev. Lett.* **126**, 228001 (2021).
29. Baeuerle, T., Loeffler, R. C. & Bechinger, C. Formation of stable and responsive collective states in suspensions of active colloids. *Nat. Commun.* **11**, 2547 (2020).
30. Loeffler, R. C., Baeuerle, T., Kardar, M., Rohwer, C. M. & Bechinger, C. Behavior-dependent critical dynamics in collective states of active particles. *EPL* **134**, 64001 (2021).
31. Liebchen, B. & Löwen, H. Which interactions dominate in active colloids? *Chem. Phys.* **150**, 061102 (2019).
32. Stark, H. Artificial chemotaxis of self-phoretic active colloids: collective behavior. *Acc. Chem. Res.* **51**, 2681–2688 (2018).
33. Auschra, S., Bregulla, A., Kroy, K. & Cichos, F. Thermotaxis of Janus particles. *Eur. Phys. J. E* **44**, 90 (2021).
34. Fränzl, M., Muinos-Landin, S., Holubec, V. & Cichos, F. Fully steerable symmetric thermoplasmonic microswimmers. *ACS Nano* **15**, 3434–3440 (2021).
35. Selmke, M., Khadka, U., Bregulla, A. P., Cichos, F. & Yang, H. Theory for controlling individual self-propelled micro-swimmers by photon nudging I: directed transport. *Phys. Chem. Chem. Phys.* **20**, 10502–10520 (2018).
36. Selmke, M., Khadka, U., Bregulla, A. P., Cichos, F. & Yang, H. Theory for controlling individual self-propelled micro-swimmers by photon nudging II: confinement. *Phys. Chem. Chem. Phys.* **20**, 10521–10532 (2018).
37. Tunström, K. et al. Collective states, multistability and transitional behavior in schooling fish. *PLoS Comput. Biol.* **9**, e1002915 (2013).
38. Insperger, T. On the approximation of delayed systems by Taylor series expansion. *J. Comput. Nonlinear Dyn.* **10**, 024503 (2015).
39. Muinos-Landin, S., Fischer, A., Holubec, V. & Cichos, F. Reinforcement learning with artificial microswimmers. *Sci. Robot.* **6**, eabd9285 (2021).
40. Strogatz, S. H. *Nonlinear Dynamics and Chaos: With Applications to Physics, Biology, Chemistry and Engineering* (Perseus Books, 1994).
41. Goldenfeld, N. *Lectures on Phase Transitions and the Renormalization Group* 1st edn (CRC Press, 1992).
42. Vollmer, J., Vegh, A. G., Lange, C. & Eckhardt, B. Vortex formation by active agents as a model for Daphnia swarming. *Phys. Rev. E* **73**, 061924 (2006).
43. Bregulla, A. P., Würger, A., Günther, K., Mertig, M. & Cichos, F. Thermo-osmotic flow in thin films. *Phys. Rev. Lett.* **116**, 188303 (2016).
44. Popescu, M. N., Uspal, W. E. & Dietrich, S. Chemically active colloids near osmotic-responsive walls with surface-chemistry gradients. *J. Phys. Condens. Matter* **29**, 134001 (2017).
45. Spagnolie, S. E. & Lauga, E. Hydrodynamics of self-propulsion near a boundary: predictions and accuracy of far-field approximations. *J. Fluid Mech.* **700**, 105–147 (2012).
46. Lintuvuori, J. S., Würger, A. & Stratford, K. Hydrodynamics defines the stable swimming direction of spherical squirmers in a nematic liquid crystal. *Phys. Rev. Lett.* **119**, 068001 (2017).
47. Wioland, H., Woodhouse, F. G., Dunkel, J. & Goldstein, R. E. Ferromagnetic and antiferromagnetic order in bacterial vortex lattices. *Nat. Phys.* **12**, 341–345 (2016).
48. Nishiguchi, D., Aranson, I. S., Snezhko, A. & Sokolov, A. Engineering bacterial vortex lattice via direct laser lithography. *Nat. Commun.* **9**, 4486 (2018).
49. Fletcher, G. A mechanical analog of first- and second-order phase transitions. *Am. J. Phys.* **65**, 74–81 (1997).
50. Kuramoto, Y. International symposium on mathematical problems in theoretical physics. *Lect. Notes Phys.* **30**, 420 (1975).
51. O’Keeffe, K. P., Hong, H. & Strogatz, S. H. Oscillators that sync and swarm. *Nat. Commun.* **8**, 1504 (2017).
52. Fruchart, M., Hanai, R., Littlewood, P. B. & Vitelli, V. Non-reciprocal phase transitions. *Nature* **592**, 363–369 (2021).
53. Loos, S. A. M. & Klapp, S. H. L. Fokker–planck equations for time-delayed systems via markovian embedding. *J. Stat. Phys.* **177**, 95–118 (2019).
54. Geiss, D., Kroy, K. & Holubec, V. Brownian molecules formed by delayed harmonic interactions. *New J. Phys.* **21**, 093014 (2019).
55. Drescher, K., Dunkel, J., Cisneros, L. H., Ganguly, S. & Goldstein, R. E. Fluid dynamics and noise in bacterial cell-cell and cell-surface scattering. *Proc. Natl. Acad. Sci. USA* **108**, 10940–10945 (2011).
56. Lauder, G. V. & Drucker, E. G. Forces, fishes, and fluids: hydrodynamic mechanisms of aquatic locomotion. *Physiology* **17**, 235–240 (2002).
57. Verma, S., Novati, G. & Koumoutsakos, P. Efficient collective swimming by harnessing vortices through deep reinforcement learning. *Proc. Natl. Acad. Sci. USA* **115**, 5849–5854 (2018).
58. Morin, A., Caussin, J.-B., Eloy, C. & Bartolo, D. Collective motion with anticipation: flocking, spinning, and swarming. *Phys. Rev. E* **91**, 012134 (2015).
59. Palmer, S. E., Marre, O., Berry, M. J. & Bialek, W. Predictive information in a sensory population. *Proc. Natl. Acad. Sci. USA* **112**, 6908–6913 (2015).

## Acknowledgements

We thank Daniel Geiss for assembling the data in Table S1 and acknowledge funding through DFG-GACR cooperation by the Deutsche Forschungsgemeinschaft (DFG Project No 432421051) and by the Czech Science Foundation (GACR Project No 20-02955J). V.H. was supported

by the Humboldt Foundation. We thank Andrea Kramer for proofreading the manuscript. We also acknowledge financial support by the Open Access Publishing Fund of Leipzig University supported by the German Research Foundation within the program Open Access Publication Funding.

### Author contributions

X.W. and F.C. conceived the experiment. X.W. carried out the experiment. X.W., F.C., P.-C.C., and V.H. analyzed the data. P.-C.C., K.K., and V.H. developed the theory. X.W., P.-C.C., and F.C. carried out simulations. X.W., P.-C.C., K.K., V.H., and F.C. discussed the results and wrote the manuscript.

### Funding

Open Access funding enabled and organized by Projekt DEAL.

### Competing interests

The authors declare no competing interests.

### Additional information

**Supplementary information** The online version contains supplementary material available at <https://doi.org/10.1038/s41467-022-35427-7>.

**Correspondence** and requests for materials should be addressed to Frank Cichos.

**Peer review information** *Nature Communications* thanks Anton Souslov, and the other, anonymous, reviewer for their contribution to the peer review of this work. Peer reviewer reports are available.

**Reprints and permissions information** is available at <http://www.nature.com/reprints>

**Publisher's note** Springer Nature remains neutral with regard to jurisdictional claims in published maps and institutional affiliations.

**Open Access** This article is licensed under a Creative Commons Attribution 4.0 International License, which permits use, sharing, adaptation, distribution and reproduction in any medium or format, as long as you give appropriate credit to the original author(s) and the source, provide a link to the Creative Commons license, and indicate if changes were made. The images or other third party material in this article are included in the article's Creative Commons license, unless indicated otherwise in a credit line to the material. If material is not included in the article's Creative Commons license and your intended use is not permitted by statutory regulation or exceeds the permitted use, you will need to obtain permission directly from the copyright holder. To view a copy of this license, visit <http://creativecommons.org/licenses/by/4.0/>.

© The Author(s) 2023

# Manfred Eigen

(1927–2019)

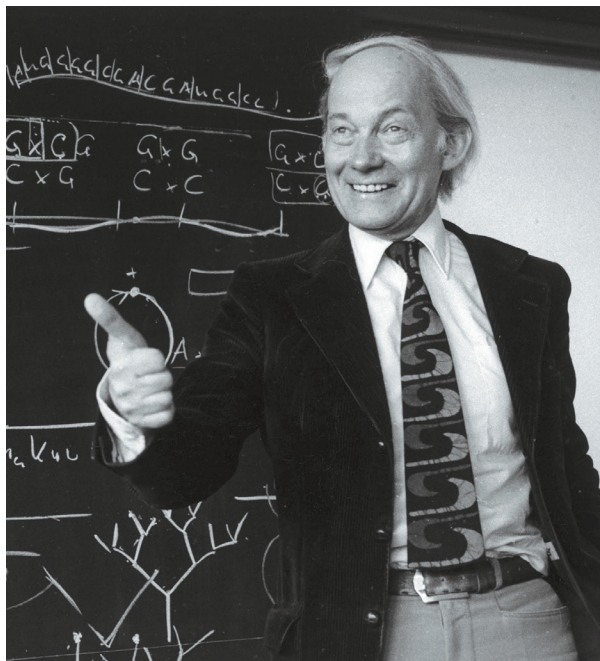
Observer of fast reactions in the laboratory and in life.

Chemist Manfred Eigen regarded received wisdom as a challenge rather than a constraint. His techniques for investigating ‘immeasurably fast’ reactions and their application to biological systems opened up new avenues, in fields from fundamental kinetics to the formation of protein complexes. This work, conducted in the 1950s at the Max Planck Institute (MPI) for Physical Chemistry in Göttingen, won him a share (with Ronald Norrish and George Porter) of the 1967 Nobel Prize in Chemistry. He went on to develop theories to account for the self-organization of biological molecules, and he was a creator of the new field of evolutionary biotechnology.

At a time when most institutes and departments were split along disciplinary lines, Eigen argued that understanding organisms at the level of their chemical interactions demanded an interdisciplinary approach. After years of lobbying, he got his wish in 1971, when the Max Planck Society (MPS) created the MPI for Biophysical Chemistry in Göttingen. ‘It is not the research area that counts,’ ran the founding principle of the laboratory: ‘it is the excellence of the individuals.’ He was less successful at persuading the MPS to found an institute for science and music.

Eigen was born in Bochum, Germany, where his father was a cellist. By 15, he was himself a proficient pianist with the potential for a future solo career. He’d also developed an interest in chemistry, doing experiments in a lab at home. But, in 1942, as allied bombers began to shift the balance against Germany in the Second World War, his class was drafted to the anti-aircraft batteries defending the city; two years later, he was conscripted into the German air force.

When Germany surrendered in May 1945, 2 days before his 18th birthday, Eigen was stationed at Salzburg airport in Austria, which was occupied by US troops. Captured as prisoners of war, Eigen and a friend managed to escape, and walked roughly 1,000 kilometres back to Bochum over the next month. Having not touched a piano for three years, he decided to make his career in science. The University of Göttingen accepted him as a student of geophysics — the only branch of physics with room for him, when so many older students were returning from military service. He studied with some of the country’s



leading physicists, including Nobel prizewinners Werner Heisenberg and Wolfgang Paul.

In 1953, after a doctorate on the specific heat of heavy water, Eigen moved to the recently founded MPI for Physical Chemistry to work with its director, Karl Friedrich Bonhoeffer. In a standard textbook co-authored by his former supervisor, Arnold Eucken, Eigen found reactions described as ‘immeasurably fast’. Refusing to accept such uncertainty, by 1954, he had developed a way of disturbing the equilibria in chemical solutions with pulses of intense electrical or ultrasonic energy, and using spectroscopy to time how long it took for equilibrium to be restored. Such ‘relaxation techniques’ could determine the rate of a neutralization reaction that took place in nanoseconds — orders of magnitude faster than any previously measured.

His success made it possible for scientists to study reactions catalysed by enzymes that drive all processes of life. Eigen developed concepts to explain how replicating macromolecules on the prebiotic Earth might have evolved into replicating organisms. In 1971, for example, he posed the paradox that without error-correction enzymes, the length of a nucleic acid would be limited because, in larger molecules, mutations would destroy the information content of subsequent generations. But this maximum size (or error threshold) was too small to encode an error-correcting enzyme. Eigen’s paradox still

challenges theoretical biologists.

From the early 1980s, he developed these concepts into evolutionary biotechnology at the MPI. His colleagues built ‘evolution reactors’ that drove the evolution of viruses and other replicating molecules under controlled conditions to investigate how pathogens evade the immune system, or to search for new drugs. Eigen helped to found two companies to exploit this technology, Evotec Biosystems (now Evotec AG) and DIREVO Biotech (bought by Bayer Healthcare in 2008).

Although he oversaw the design and location of the MPI for Biophysical Chemistry, Eigen declined the post of permanent director, instead heading its Department of Biochemical Kinetics until he retired in 1995. ‘His way of solving problems with the best factual and transparent solution instead of imposing his unquestioned authority shaped the spirit of the institute,’ wrote MPI colleagues in an article celebrating Eigen in his 90th year (H. Jäckle *et al. Eur. Biophys. J.* 47, 319–323; 2018). Eigen remained active after retirement, dividing his time between Göttingen and the Scripps Research Institute in La Jolla, California.

Communication with the wider public was important to him. He published three books aimed at the general reader: *Laws of the Game* (1983), *Steps Towards Life* (1992) and *From Strange Simplicity to Complex Familiarity* (2013). All were written jointly with his long-standing scientific partner, Ruthild Winkler-Oswatitsch, who became his second wife.

He chaired the council of Europe’s life-sciences organization EMBO through delicate negotiations to establish a base in Heidelberg in the early 1970s. And in his 12 years presiding over the German Academic Fellowship Foundation, he pushed for the advancement of young scientists through doctoral grants. He remained an impressive amateur pianist, sometimes playing Mozart’s concertos after scientific meetings. A man of great personal elegance, with a taste for striking ties, his quest for elegant solutions widened the field of view for generations of researchers that followed. ■

Georgina Ferry is a science writer from Oxford, UK, specializing in the history of the life sciences. Her books include biographies of the crystallographers Dorothy Crowfoot Hodgkin and Max Perutz. e-mail: mgf@georginaferry.com

# John Horton Conway

(1937–2020)

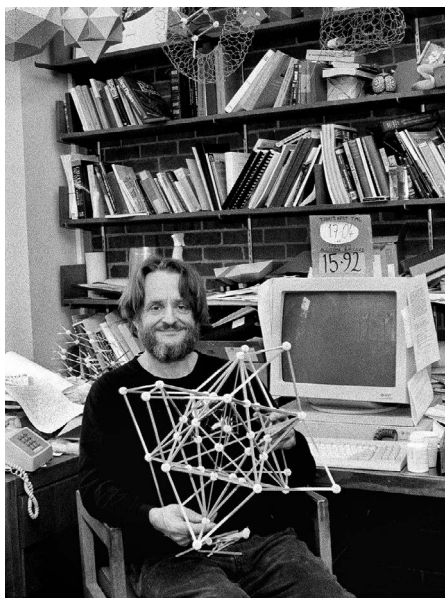
Playful master of games who transformed mathematics.

**J**ohn Horton Conway was one of the most versatile mathematicians of the past century, who made influential contributions to group theory, analysis, topology, number theory, geometry, algebra and combinatorial game theory. His deep yet accessible work, larger-than-life personality, quirky sense of humour and ability to talk about mathematics with any and all who would listen made him the centre of attention and a pop icon everywhere he went, among mathematicians and amateurs alike. His lectures about numbers, games, magic, knots, rainbows, tilings, free will and more captured the public's imagination.

Conway, who died at the age of 82 from complications related to COVID-19, was a lover of games of all kinds. He spent hours in the common rooms of the University of Cambridge, UK, and Princeton University in New Jersey playing backgammon, Go and other diversions, some of his own creation. Several of Conway's most celebrated contributions were made while he was thinking about games and their strategies. Perhaps his greatest discovery was a surprising correspondence between numbers and games that led him to a truly gigantic system, the surreal numbers, which stunned the mathematics community. It contained not only the positive and negative real numbers that we all know, but also new infinitely large numbers, infinitesimally small ones, and all sorts of new numbers in between.

Conway's work on surreal numbers emerged from the influential research project and book *Winning Ways for your Mathematical Plays* (1982), a compendium of information on the theory of games, written with Elwyn Berlekamp and Richard Guy. This fascination with games also led Conway to develop the Game of Life, a cellular automaton in which the pattern of live or dead cells in a two-dimensional grid evolves according to a set of rules for the 'birth' and 'death' of each cell, based on the status of its nearest neighbours. The simplicity and accessibility of this game was popularized in 1970 by *Scientific American* columnist Martin Gardner. By the mid-1970s, it was estimated that one-quarter of the world's computers were running Conway's Game of Life as their screensaver.

Conway, who was the John von Neumann professor of mathematics at Princeton University before his retirement in 2013, was born in Liverpool, UK, in 1937. His father made his living playing cards, and later worked as a



chemistry laboratory technician at a local high school attended by George Harrison and Paul McCartney. Conway, like his mother, was an avid reader. He showed early interests in mathematics; by the age of 11, he wanted to be a mathematician at Cambridge. He received his PhD from the University of Cambridge in 1964 under the advisership of Harold Davenport, was subsequently hired at Cambridge as a lecturer, and became professor in 1983. In 1987, he moved to Princeton.

**“His lectures about numbers, games, magic, knots, rainbows and more captured the public’s imagination.”**

Conway first attained fame in 1968 for determining all 8,315,553,613,086,720,000 symmetries of the Leech lattice – a remarkably regular arrangement of points in 24-dimensional space discovered by John Leech in 1967. This led to his discovery of the Conway simple groups, which were fundamental in the classification of finite simple groups – one of the capstone achievements of twentieth-century mathematics.

Conway had a primary role in researching and assembling the iconic symmetry book *ATLAS of Finite Groups* (1985). His deep knowledge of symmetries led him to propose, with his *ATLAS* co-author Simon Norton, the

Monstrous Moonshine conjectures. These, for the first time, seriously connected finite symmetry groups to analysis – and thus discrete maths to non-discrete maths. Today, the Moonshine conjectures play a key part in physics – including in the understanding of black holes in string theory – inspiring a wave of further such discoveries connecting algebra, analysis, physics and beyond.

Conway's discovery of a new knot invariant – used to tell different knots apart – called the Conway polynomial became an important topic of research in topology. In geometry, he made key discoveries in the study of symmetries, sphere packings, lattices, polyhedra and tilings, including properties of quasi-periodic tilings as developed by Roger Penrose.

In algebra, Conway discovered another important system of numbers, the icosians, with his long-time collaborator Neil Sloane. In number theory, Conway showed that every whole number is the sum of at most 37 fifth powers. He also developed the 15-theorem (with his student William Schneeberger) and the 290-conjecture; these were vast generalizations of the four-squares theorem, proved by eighteenth-century mathematician Joseph-Louis Lagrange, which states that every positive whole number is the sum of four square numbers (for example, 21 is the sum of 16, 4, 1 and 0).

Conway was a memorable teacher and speaker, and the many tricks he performed to illustrate mathematical concepts included: stating immediately the day of the week for any date in history, twirling a hanger with a penny balanced on its inside edge, contorting his tongue into a variety of shapes, balancing objects on his chin, and delivering entire lectures in which every word he said had only one syllable.

He loved to talk about mathematics and games, as well as history, etymology and philosophy. His contributions to culture, through his work and outreach, will have a lasting impact. For the remarkable profundity of his mathematical discoveries – and the playful and generous way in which he shared these with others – he will be sorely missed.

**Manjul Bhargava** is the R. Brandon Fradd professor of mathematics at Princeton University, New Jersey, USA. He was a first-year graduate advisee, and later colleague, of John H. Conway at Princeton.  
e-mail: bhargava@math.princeton.edu